DISS. ETH NO. 29672

PHYSICAL MODELLING OF MASONRY AND REINFORCED CONCRETE USING 3D PRINTING

A thesis submitted to attain the degree of

DOCTOR OF SCIENCES
(Dr. sc. ETH Zurich)

presented by

LORENZO DEL GIUDICE

Laurea Magistrale in Ingegneria Civile,
Università degli studi di Napoli Federico II

born on *29.10.1992*

accepted on the recommendation of
Prof. Dr. Michalis F. Vassiliou
Prof. Dr. Bozidar Stojadinovic
Prof. Dr. Vasilis Sarhosis

2023

Abstract

Global level assumptions of numerical models have been identified as a major source of error in numerical modeling of masonry and reinforced concrete structures. In parallel, recent studies have shown that a statistical approach involving numerous virgin specimens and ground motions is necessary for numerical model validation. Such approach is difficult to follow because of the prohibitive experimental cost associated with dynamic testing of civil engineering structures. The only viable option to pursue a statistical approach is to reduce the size of the test units and perform the required shake table tests at small-scale. This dissertation aims at developing reduced scale physical models for the statistical validation of the global level assumptions in the numerical models of masonry and reinforced concrete structures. It explores the possibility of using different materials, other than the prototype material, which are produced with digital manufacturing technologies. The dissertation provides the mechanical characterization of the model materials, as well as the experimental study of the cyclic behavior of model masonry walls and model reinforced concrete elements.

The model material used for the manufacturing of small-scale masonry models is produced with a sand based binder jet 3D printer that uses furan binder. The first part of the dissertation investigates the mechanical properties of this material. To this end, compression and bending tests on the 3D printed material are performed. The experimental results show that the bulk material presents anisotropy in compression, however the degree of anisotropy is smaller compared to materials produced with printers using ceramic powder. In tension, the anisotropy is found to be statistically insignificant. This is in contrast with the values reported in the literature for powder-based printers. Curing time is found to be crucial for the strength build-up of the 3D printed material. In fact, both compressive and flexural strength increase over time until reaching a plateau after 15 days of curing time. No scale phenomena were observed for length scales between 50 and 100 mm.

A global sensitivity analysis of the 3D printed material with respect to the 3D printer parameter is performed. This study is motivated by the fact the mechanical properties of 3D printed material are dependent on the printing process and parameters. The analysis focuses on the influence of printing resolution, activator percentage, droplet mass, and printing speed on the compressive and flexural strength, as well as on the Young's modulus of the bulk material. In order to minimize the experimental cost of the campaign, a design of experiment approach is applied.

The experimental points are defined using a sequential latin hypercube sampling strategy. Local and total Sobol' indices are calculated for each mechanical property and loading direction through a sparse polynomial chaos expansion. The results show that the mechanical properties are primarily influenced by the binder content of the bulk material, which in turn depends on the printing resolution and the droplet mass. A dependency on the activator percentage is also found. In addition, the effect of thermal treatment is investigated. Curing of the specimens at 80° to 115° for 30 to 120 minutes increases the material strength.

This dissertation, also presents a series of quasi-static cyclic tests on 1/10-scale masonry walls. The specimen walls are produced with binder jet 3D printer. The behavior of the mortar joints is emulated by controlling the micro-geometry in the model masonry, i.e. printing notches that weaken the material in predefined sections. The compressive strength and stiffness of the model masonry was assessed with six uniaxial compression tests on scaled masonry wallets. The wallets had an average compressive strength of 10.4 MPa and an average stiffness of 4038 MPa. The model walls are subjected to drift ratios of up to 1%, presenting a failure mode comparable to a sliding failure. The cyclic loops present features that are comparable to prototype masonry walls with similar aspect ratios and failure mode.

Finally, the experimental investigation of 1/40-scale reinforced concrete elements is discussed. It is proposed to use additive manufacturing to fabricate the reinforcement cage and micro-concrete. The mechanical properties of both materials are defined experimentally. Subsequently, the results from quasi-static cyclic tests on 1/40-scale RC cantilever members are presented. Different longitudinal and transverse reinforcement configurations are tested. The experimental results are compared to numerical results obtained from an Opensees model calibrated against material level small-scale tests.

Sommario

Le ipotesi globali dei modelli numerici sono state identificate come una delle cause principali di errori nei modelli numerici di strutture in muratura e cemento armato. Contemporaneamente, studi recenti hanno dimostrato che un approccio statistico per la validazione dei modelli numerici che include numerosi campioni e numerosi accelerogrammi sia necessario. Tale approccio è difficile da perseguire a causa dei costi proibitivi associati a test dinamici di strutture. L'unica opzione possibile per poter effettuare una validazione di tipo statistica è di ridurre la dimensione dei campioni da testare and di eseguire i test su tavola vibrante in scale ridotta. Questa tesi punta allo sviluppo di modelli fisici in scala atti alla validazione statistica delle ipotesi globali nei modelli numerici di strutture in muratura e in cemento armato. La tesi analizza la possibilità di usare materiali, differenti rispetto al materiale prototipo, prodotti con tecnologie digitali. La tesi riporta la caratterizzazione dei materiali usati per i modelli in scale, oltre che allo studio sperimentale del comportamento ciclico dei modelli di muratura e cemento armato.

Il materiale usato per la creazione dei modelli in scale ridotta di muratura è prodotto con una stampante 3D con tecnologia "*Binder Jet*" che utilizza come *binder* un polimero a base di furanica. Il primo argomento trattato nella tesi consiste nello studio delle proprietà meccaniche di tale materiale. Quindi, prove a compressione e flessione del materiale stampato in 3D sono stati eseguiti. I risultati sperimentali mostrano che il materiale presenta anisotropia in compressione, tuttavia il livello di anisotropia è inferiore di altri materiali prodotti con stampanti che usano materiali ceramici. In trazione, l'anisotropia è risultata non essere statisticamente significativa. Questo non è in accordo con i risultati ritrovati nella letteratura per stampanti simili. Il tempo di maturazione è risultato essere essenziale per lo sviluppo della resistenza meccanica del materiale stampato in 3D, infatti, sia la resistenza a compressione che quella a flessione aumenta con il tempo fino a raggiungere un "*plateau"* dopo 15 giorni. Nessuno effetto di scala è stato osservato per i campioni con lunghezze tra i 50 e i 100mm.

Un'analisi di sensitività globale del materiale stampato in 3D è stata eseguita per valutare l'effetto dei parametri della stampante stessa. Lo studio si basa sul fatto che le proprietà meccanica dei materiali stampati in 3D dipendono dal processo di stampa e dai parametri utilizzati nella fase di stampa. L'analisi si focalizza su l'influenza della risoluzione di stampa, della percentuale di attivatore, la *"droplet mass"* e della velocità di stampa, sulla resistenza alla compressione e alla flessione, oltre che sul modulo di Young del materiale. Per poter minimizzare il

costo della campagna sperimentale è stato applicato un approccio basato sul "*design of experiment"*. I punti sperimentali sono stati definiti usano una strategia di campionamento del tipo "*sequential latin hypercube"*. Indici di Sobol' locali e totali sono stati calcolati per ognuna delle proprietà meccaniche ed ognuna delle direzioni di carico usando "*polynomial chaos expansion"*. I risultati mostrano che le proprietà meccaniche dipendono dalla risoluzione di stampa e dalla *"droplet mass"*. È stata identificata anche una dipendenza dalla percentuale di attivatore. Inoltre, è stato studiato l'effetto di trattamenti termici. Il trattamento dei campioni da 80° a 115° per un tempo dai 30 ai 120 minuti ha l'effetto di aumentare la resistenza del materiale.

La tesi presenta una serie di test quasi statici su muratura in scale 1/10. I campioni di muratura sono stati prodotti on una stampante 3D del tipo "*binder jet"*. Il comportamento dei giunti di malta emulato controllando la micro-geometria del modello di muratura, ovvero stampando delle indentature le quali indeboliscono il materiale in punti predefiniti. La resistenza a compressione e la rigidezza del materiale sono stati definiti sperimentalmente tramite sei test a compressioni su dei muretti in scala. I muretti avevano una resistenza media a compressione di 10.4 MPa e una rigidezza media di 4038 MPa. I muri sono stati soggetti a "*drift ratios"* fino a 1 %, ed hanno esibito un meccanismo di rottura comparabile alla rottura per "*sliding"*. I diagrammi forza spostamento hanno delle caratteristiche simili a quelli della muratura prototipo con snellezza simile e simile meccanismo di rottura.

Infine, la tesi presenta la campagna sperimentale effettuata to modelli in scale 1/40 di elementi in cemento armato. Viene proposto di utilizzare stampanti 3D per fabbricare le gabbie di armatura e di usare "*micro-concrete"*. Le proprietà meccaniche di entrami i materiali sono stati quantificate sperimentalmente. Successivamente, i risultati dei test ciclici quasi-statici su modelli in scale 1/40 di elementi a sbalzo sono presentati. Campioni con differenti configurazioni per l'armatura longitudinale e trasversale sono stati testati. I risultati sperimentali sono poi stati confrontati con i risultati numerici ottenuti grazie ad un modello OpenSees, il quale è stato calibrato con le proprietà meccaniche dei materiali ottenute sperimentalmente.

Table of Contents

1. Introduction

Abstract

This chapter introduces the reader to the work presented in this dissertation, which is related to small-scale physical modelling of masonry and reinforced concrete structures. Firstly, the motivation of this work is introduced, followed by a literature review with the most relevant studies. Subsequently, the research gaps and objectives of this study are identified. Finally, the outline of the dissertation structure and its key contributions are presented.

1.1 Motivation and problem statement

Earthquakes are one of the principal causes of casualties worldwide amongst all natural disasters as reported by (CRED Centre for Research and Epidemiology of Disasters, 2015). A portion of the total number of casualties is due to the collapse of civil structures. Moreover, earthquakes have a disruptive effect on society not only in terms of human losses but also with regard to the economic losses they cause. For instance, the total economic losses due to the 2010-2011 Canterbury earthquake are estimated at around $NZ 40 billion (Insurance council of New Zealand, 2019). Another example is given by the direct economic losses from earthquakes in Italy since 1968 until 2018, which are estimated to have reached $ 94 billion (Swiss RE, 2019).

Over the years the understanding of the seismic behavior of masonry and reinforced concrete (RC) structures has improved and this led to the design of more resilient and safe structures. However, the earthquake behavior of masonry and RC structures is still an open research subject. Masonry buildings have a higher level of complexity compared to other building materials caused by the large dispersion of material and construction methods used in different countries. However, a common source of uncertainty in both masonry and RC structures lies in the interaction between different structural components, especially under dynamic loading.

The study of single structural components, i.e. mechanical characterization of single beams, columns, walls with openings, piers, etc., is necessary but not sufficient to define the seismic behavior of an entire building. The interaction between single components during seismic events is assessed through system-level dynamic tests, which are aimed at the development of more accurate numerical models to predict the seismic behavior of structures.

System-level dynamic tests are a powerful tool to improve the understanding of the seismic behavior of masonry and RC structures. Unfortunately, it is often problematic to perform system-level dynamic tests of whole structures because of the size of the test units. These are generally of large dimensions, e.g. multistory buildings (Miglietta et al., 2021; Panagiotou et al., 2011), consequently it is prohibitive to test entire structures at full-scale, both because of the limited number of facilities that are able to accommodate such large test units and because of the costs associated with these tests.

The lack of numerous shake table tests of masonry and RC structures makes the data set on which numerical models can be validated and calibrated very limited. Consequently, the

performance of the numerical models used to predict the seismic response of structures is often grossly insufficient. For instance, blind prediction contests (Candeias et al., 2017; Panagiotou et al., 2011) show large discrepancies in the numerical predictions compared to the experimental results. System level dynamic tests would allow the validation and, hence, the improvement of the system level assumptions (global damping formulation, component interaction, boundary conditions, etc.) of the numerical models. These have been identified as a main source of errors numerical modeling (Bradley, 2013).

Therefore, the work presented in this dissertation is motivated by the need for a reliable and affordable experimental methodology to perform dynamic testing of civil engineering structures at a reduced cost. A methodology for faster and affordable shake table tests would foster the development of more refined and accurate numerical models and facilitate the validation of the system-level assumptions, which in turn could be used to mitigate the disastrous effects of earthquakes.

1.2 Background and state-of-the-art

1.2.1 The concept of statistical model validation

The validation of global level assumptions is a key step towards more refined and accurate numerical models of masonry and RC structures. In addition, Bachmann et al. (2018) argued that it is not always possible to validate numerical models deterministically (i.e. by trying to predict the response to individual ground motion). To this end, Bachmann et al. (2018, 2019) claimed that the conventional validation test of reproducing the experimentally obtained response to a particular ground motion with acceptable accuracy is too strict of a validation test for structural models. To support this, they claimed that the earthquake engineering design problem involves predicting the statistics of the response to an ensemble of ground motions characterizing a given seismic hazard; not to a single ground motion. The statistical validation is a weaker model validation test that requires that the structural model only be unbiased and introduce less uncertainty than the uncertainty of the excitation itself. Bachmann et al. (2018, 2019) applied this weaker (but sufficient) validation procedure on the 1963 Housner dynamic response model of an uplifting structure. They performed 600 shake table tests using a well-defined and repeatable uplifting structure as well as 600 numerical simulations of these tests and compared both the individual test responses and the statistical aggregates of these responses focused on predicting limit states such as overturning or maximum tilt angle. They showed that the 1963 Housner model passes the weak validation test even though it fails the

strong validation test. In other words, in this case the motion-to-motion variability is more important than the accuracy of the structural model. Therefore, the numerical model is good enough for the scope of Earthquake Engineering. Similar results were obtained by Vassiliou et al. (2021a, 2021b). The above procedure bypasses the important issue of repeatability in shake table testing. To the best of the author's knowledge there has not been a thorough study on the repeatability of large-scale RC structures shake table tests, as this requires testing multiple identical (to constructional accuracy) and virgin specimens. Shake table tests of rocking structures (these are easier to test multiple times as they do not get damaged) have shown that repeatability is not observed, thus making any deterministic blind prediction contests of rocking structures essentially useless. However, the tests are repeatable in the statistical sense, i.e. the CDF of the response to multiple excitations is repeatable. It is worth noting that the concept of comparing seismic analysis methods in terms of the statistics of the response to sets of ground motions rather than in terms of individual responses is not something novel in Earthquake Engineering. It can be seen in Chapter 23 of the 4th edition of Chopra's Structural Dynamics textbook (Chopra, 2012). However, up to now it involved comparisons between different analysis methods (usually a more approximate against a more refined, taken as benchmark); not between an analysis method and experimental tests. The optimal validation procedure question extends beyond Earthquake and Structural Engineering. Roy & Oberkampf (2011) describe a comprehensive framework for verification, validation, and uncertainty quantification in scientific computing that resembles the method proposed herein. The above argumentation shows that statistical validation might not constitute only a "good to have" approach, but a necessity sourcing from the stochastic nature of the seismic response of a system. Extending this statistical validation method to more realistic structures is not trivial. Since testing of RC and masonry specimens involves damaging them, one would need multiple virgin specimens. This is cost- and time-wise not viable in full scale, and this is the reason why researchers have been limited to perform comparisons between individual excitations, often in the context of blind prediction contests. Such contests give a clear picture of the current state-of-the art in numerical modeling of masonry and RC structures.

1.2.2 Overview of blind prediction contests of shake table tests

Mendes et al. (2017) describes the results of a blind prediction contest organized during the 9th International Masonry Conference (9IMC, July 2014). In this contest, 25 world experts on masonry were invited to present blind-predictions for two one-story masonry structures, which were tested on the shake table of the University of Lisbon under a ground motion that

was gradually scaled until the collapsed. The two mock-ups had three walls and a U-shaped plan. Both structures had an opening in the front wall and a top gable. One of the side walls had a window and the other side wall was blind. The main difference between the two test units was the type of masonry used to construct them; one was a brick masonry while the other one was a stone masonry. The details of the two masonry mock-ups are reported in (Candeias et al., 2017). All participants were provided with the as built mechanical properties (obtained from laboratory tests) of the structures and the exact input ground motions. They were invited to predict the PGA that cause collapse. The experts adopted three modeling approaches: a) rigid block dynamics, b) Finite Elements (FE), and c) Discrete Elements (DE). The PGA at collapse for the stone masonry mock-up predicted by the participants ranged from 0.22-2.50 g with a coefficient of variation of 63%. The actual PGA at collapse measured during the experiment was equal to 1.07 g. It is worth noting that also the collapse mechanism predicted by the participants was not always correct. Similarly, the predictions of the PGA at collapse for the brick specimen ranged from 0.30-1.00 g (COV = 39%), which are lower than the experimental result of 1.27 g.

The uncertainty in the prediction of the dynamic behavior of masonry structures is thoroughly analyzed by Parisse et al. (2021). In this paper, the authors analyzed the results of blind prediction tests in which several experts were asked to predict the behavior of two masonry structures subjected to dynamic loading and the results were compared to assess the dispersion in the predictions. The outcome of this exercise showed that the wide range of numerical modeling techniques and analysis results in a large dispersion of the predictions.

Concerning RC structures, blind prediction contests show that the contestants do not predict the response of the tested specimens with reasonable accuracy, even for structures that are simpler than the ones constructed in practice. For instance, in 2010, a simple RC column was tested on the shake table of UCSD under a set of 6 ground motions (Schoettler et al., 2012; Terzic et al., 2015). A total of 41 teams of experts (17 from professional practice and 24 from the academia) were invited to predict the response. The measured response and the predictions for the maximum top displacement showed a large dispersion. Interestingly, after the test series of six ground motions the column did not appear to have failed. However, only 14 out of 41 contestants predicted “no failure”, while the rest predicted “failure”. In addition, within the group that predicted failure, there was a large dispersion related to the mode of failure.

Panagiotou et al. (2011) tested a full-scale 7-story RC building slice with a rectangular wall under 4 ground motions and 21 teams were invited to predict the response. Again, the results showed a large dispersion between the contestants and most of them failed to predict the response of the tested structure with reasonable accuracy.

The blind prediction contests clearly show that even state-of-the-art numerical models are often inadequate. In order to improve them, it is necessary to perform more shake table tests aimed at their calibration and validation. However, these are often prohibitively expensive. To make the experimental investigation of large tests units such as masonry building and RC structure more affordable, several authors have investigated the option of using small-scale models.

1.2.3 Small scale testing of masonry and RC models

Several authors used small scale models to study the static and dynamic behavior of solid brick masonry (Mohammed et al., 2011; Mohammed & Hughes, 2011) and hollow clay brick masonry (Petry & Beyer, 2014) at different scales (1/2- , 1/4-, 1/5-, and 1/6-scale). The focus of these studies was to create replica models of prototype structures to infer about the strength and displacement capacity of unreinforced masonry structures. In order to achieve this the models needed to respect the condition of similarity according to the scaling laws derived from dimensional analysis (Barenblatt & Isaakovich, 1996; Harris & Sabnis, 1999).

Petry and Beyer (2014) investigated the effects of scaling on masonry walls. They performed a comprehensive experimental campaign on walls both at full-scale and at 1/2-scale. The mechanical properties were measured at both scales through compression tests on wallets, diagonal compression tests, and shear test on masonry triplet. Subsequently, the in-plane lateral cyclic behavior of walls at both scales was tested. The results showed that already at 1/2- scale there is distortion, especially in terms of displacement capacity and lateral stiffness of the model masonry.

Abrams (1996) investigated the effect of scale and loading rate on reduced scale masonry structure through static and dynamic tests of 3/8-scale unreinforced masonry structure. The model structure was constructed with model clay bricks. Mechanical properties of the model masonry were assessed with material tests done on scaled masonry assembly. The results of the reduced scale dynamic tests were compared to results of static tests of the prototype structure. The comparison of the tests showed differences in the crack patterns and lateral force capacity.

Tomaževič and Velechovsky (1992) investigated the dynamic response of small-scale masonry structures by manufacturing and testing models up to 1/7-scale. After testing several samples on a shake-table they concluded that 1/5- scale is to be considered a limit to test models made of prototype material in order to gain insight on the dynamic behavior of masonry structures. At these scales (1/2- to 1/5- scale), it is still necessary to use large facilities when the system-level behavior is sought. Another level of complexity, at this scale, concerns the need of additional masses to preserve similitude of stresses.

Attempts to reduce the size of RC and masonry specimens to scales smaller than 1/7-scale do exist in literature. Ritter (2017) built a 1/75- scale model of an unreinforced masonry building. However, the scope of his study was to investigate the soil structure interaction (SSI). Consequently, the focus of the author was on features that affect the SSI, i.e. capturing the friction between the structure and the soil, preserving the similitude of stress in the soil, and preserving global stiffness of the model structure. There is no interest in capturing the strength of the model structure, e.g. failure mechanisms, masonry strength, etc.

DeJong and Vibert (2012) tested 1/20-scale models of a masonry spire with the sole purpose of validating a discrete element method model (DEM). Since in this type of structures the strength of the material is not considered crucial, no attempts to preserve similitude of stresses was made.

In parallel, aiming at studying soil structure interaction (SSI) problems with a centrifuge, geotechnical engineers have built small scale physical models of RC elements. Knappett et al. (2011) investigated the mechanical behavior of RC elements at 1/40-scale. The characterization of the specimens included the study of RC beams with and without shear reinforcement, as well as models with smooth and rough rebars. The tests consisted of a series of three- and four-point bending tests and the results were in good agreement with prototype elements. The manufacturing of the specimens was done manually and this resulted in a time-consuming process, which limits the number of specimens that can be produced.

Loli et al. (2014) used small-scale RC model of a bridge pier. Similarly to Knappett et al. (2011), the results of this study were promising, however, the manufacturing of the samples was labor intensive and time consuming. All rebars and shear reinforcement were shaped and positioned manually in the formworks before casting. Such procedure leads to inaccuracy in the reinforcement position, long construction time, and limitations in the available sizes of reinforcement.

Moehle and Sozen (1978) used small scale models of reinforced concrete structures. In their study, dynamic tests of 10 story reinforced concrete frames were performed. The model reinforced concrete structure had beams with 38x38mm gross cross section and columns with 51x38mm cross sections. 13 gauge (2.3 mm) wires were used for the longitudinal reinforcement and 10 gauge (2.0 mm) wires were use as shear reinforcement. The test results were compared to calculated quantities. The response frequencies of the model structure were considerably different from the calculated ones. The displacement obtained from the calculations compared fairly well to the measured values during the earthquake simulations. The calculated forces were substantially less than the measured values. The discrepancies in the forces was attributed to differences in the in stiffness between the specimen and the numerical model.

In addition to the studies on scaled masonry and RC structures, it is useful to report some of the studies performed on physical modeling of steel structures. Moncarz and Krawinkler (1981) presented a complete study on the development of small-scale physical models of steel structures with emphasis on the selection of adequate model materials to create true-replica models of steel structures and the introduction of a correction factor to account for the distortion of the models.

Lignos et al. 2010 tested two 1/8-scale 4-storey moment-resisting frames on a shake table and compared them to analytical predictions. The physical models consisted of two substructures: the scaled model of the moment resisting frame and a mass simulator. The latter was connected with “rigid” links in the horizontal direction at each floor level. The experimental campaign concluded that simple analytical models are able to predict the dynamic response of the moment resisting frame under seismic loading.

1.3 Research gap and objectives

It is not cost efficient to perform extensive large-scale tests to produce the large amount of data that is necessary to validate and improve the global level assumptions of numerical models used in earthquake engineering. However, small scale testing can provide a viable alternative. This thesis uses 3D printing to suggest a methodology to build small scale specimens (of scales as low as 1:40) for the physical modelling of masonry and RC structures. The main advantages of this manufacturing technique are the increase in construction speed, consistency across multiple samples, control of the material properties, and low cost of sample production.

Before these physical models are used in a centrifuge to physically model whole structures, the following research gaps need to be filled: a) The mechanical behavior of the 3D

printed material should be determined; and b) The component-level quasi-static cyclic behavior of the specimens need to be controlled and understood.

This thesis presents experimental studies (supported by numerical simulations) that contribute towards addressing the above research gaps by achieving the following objectives: a) Study the mechanical properties of the bulk printed material that can be used for the manufacturing of physical models of masonry; b) Understand the dependence of these properties on the printing parameters using polynomial-chaos-expansion (PCE) and Sobol's indices; c) Create a 3D printed physical model of a masonry wall and test it cyclically; and d) Build and test a physical model of a RC beam using a 3D printed reinforcing cage.

1.4 Structure of the dissertation

This dissertation comprises six chapters. Chapter 1 presents a short introduction on the strategies to validate numerical models to capture the system level behavior of masonry and RC structures subject to seismic actions. It also discusses the problem of shake table testing of civil engineering structures and the necessity to manufacture small-scale models to reduce the cost associated with shake table tests.

Chapter 2 presents the results of mechanical characterization of the 3D printed material used to manufacture small-scale masonry structures. It focuses on the orthotropic behavior of material printed with a sand-based binder jet 3D printer. The experimental campaign shows that 3D printed material is slightly anisotropic. In addition, the effect of curing time on the compressive and bending strength of the material is experimentally determined.

Chapter 3 further investigates the mechanical properties of 3D printer material produced with a sand-based binder jet 3D printer. It focuses on the dependence of the mechanical properties on the settings of the 3D printer. As 3D printers have different settings (input parameters) that are strictly linked to the performances of material produced, to reduce the number of tests needed in the experimental campaign, a design of experiment approach is applied. Sparse polynomial chaos expansion (PCE) is used to derive a functional relationship between input parameters and mechanical properties. Finally, to quantify the weight that each input parameter has on the mechanical properties, Sobol's indices are computed as a by-product of the polynomial chaos expansion.

Chapter 4 presents the experimental results of quasi-static cyclic tests conducted on 1/10-scale masonry walls manufactured with a sand-based binder jet 3D printer. The chapter

shows a novel approach to manufacture small-scale physical models of masonry walls with the use of a single material (3D printed). To this end the behavior of the mortar joints is emulated by controlling the micro-geometry in the model masonry by printing micro-notches. The cyclic tests are performed on 11 model walls with different joint designs and pre-compression levels. All samples have fixed-ends boundary conditions and subjected to drift ratios of up to 1 %.

Chapter 5 describes the development of 1/40-scale reinforced concrete flexural members and the results of quasi static cyclic tests. The sample consisted of a reinforcement cage which is entirely produced with selective laser melting (SLM) and micro-concrete. The mechanical properties of both the reinforcement and the model concrete are determined experimentally with uniaxial tension tests, uniaxial compression tests, and four point bending tests. In addition, the chapter shows a comparison between the cyclic behavior of the manufactured micro reinforced concrete samples and the numerical model developed in Opensees.

The dissertation closes with Chapter 6, which summarizes the key findings and contributions of this work, as well as suggestions for future research.

1.5 References

Abrams, D. (1996). Effects of scale and loading rate with tests of concrete and masonry structures. *Earthquake Spectra*, *12(1),* 13-28.

Bachmann, J., Strand, M., Vassiliou, M. F., Broccardo, M., & Stojadinovic, B. (2018). Is rocking motion predictable? *Earthquake Engineering & Structural Dynamics*, *47*(2), 535–552. https://doi.org/10.1002/eqe.2978

Bachmann, J., Strand, M., Vassiliou, M. F., Broccardo, M., & Stojadinovic, B. (2019). Modelling of rocking structures: Are our models good enough? In *2nd International Conference on Natural Hazards & Infrastructure (ICONHIC 2019)*.

Barenblatt, G. I., & Isaakovich, B. G. (1996). *Scaling, self-similarity, and intermediate asymptotics: dimensional analysis and intermediate asymptotics*. Cambridge University Press.

Bradley, B. A. (2013). A critical examination of seismic response uncertainty analysis in earthquake engineering. *Earthquake Engineering and Structural Dynamics*, (42), 1717–1729. https://doi.org/DOI: 10.1002/eqe.2331

Candeias, P. X., Campos Costa, A., Mendes, N., Costa, A. A., & Lourenço, P. B. (2017). Experimental assessment of the out-of-plane performance of masonry buildings through shaking table tests. *International Journal of Architectural Heritage*, *11*(1), 31–58.

Ceci, A. M., Contento, A., Fanale, L., Galeota, D., Gattulli, V., Lepidi, M., & Potenza, F. (2010). Structural performance of the historic and modern buildings of the University of L'Aquila during the seismic events of April 2009. *Engineering Structures*, *32*(7), 1899–1924.

Chopra, A. K. (2012). *Dynamics of structures: theory and applications to earthquake engineering* (4th ed.). Prentice Hall: Pearson.

CRED Centre for Research and Epidemiology of Disasters. (2015). The human cost of natural disasters 2015: a global perspective. Centre for Research on Epidemiology of Disasters,

Université catholique de Louvain.
DeJong, M. J., & Vibert, C. (2012). Seismic response of stone masonry spires: Computational and experimental modeling. *Engineering Structures*, *40*, 566–574.
Eberhard, M. O., Baldridge, S., Marshall, J., Mooney, W., & Rix, G. J. (2010). The mw 7.0 Haiti earthquake of January 12, 2010: USGS/EERI advance reconnaissance team report. *US Geological Survey Open-File Report*, *1048*, 58.
Harris, H. G., & Sabnis, G. (1999). *Structural modeling and experimental techniques*. CRC press.
Knappett, J. A., Reid, C., Kinmond, S., & O'Reilly, K. (2011). Small-scale modeling of reinforced concrete structural elements for use in a geotechnical centrifuge. *Journal of Structural Engineering*, *137*(11), 1263–1271.
Loli, M., Knappett, J. A., Brown, M. J., Anastasopoulos, I., & Gazetas, G. (2014). Centrifuge modeling of rocking-isolated inelastic RC bridge piers. *Earthquake Engineering & Structural Dynamics*, *43*(15), 2341–2359.
Lignos, D. G., Krawinkler, H., & Whittaker, A. S. (2011). Prediction and validation of sidesway collapse of two scale models of a 4-story steel moment frame. *Earthquake Engineering & Structural Dynamics, 40*(7), 807-825.
Mendes, N., Costa, A. A., Lourenço, P. B., Bento, R., Beyer, K., de Felice, G., et al. (2017). Methods and approaches for blind test predictions of out-of-plane behavior of masonry walls: A numerical comparative study. *International Journal of Architectural Heritage*, *11*(1), 59–71.
Miglietta, M., Damiani, N., Guerrini, G., & Graziotti, F. (2021). Full-scale shake-table tests on two unreinforced masonry cavity-wall buildings: effect of an innovative timber retrofit. *Bulletin of Earthquake Engineering*, *19*(6), 2561–2596.
Moehle, J. P., & Sozen, M. A. (1978). Earthquake simulation tests of a ten-story reinforced concrete frame with a discontinued first-level beam. *Civil Engineering Studies* SRS-451.
Mohammed, A., & Hughes, T. G. (2011). Prototype and model masonry behaviour under different loading conditions. *Materials and Structures*, *44*(1), 53–65.
Mohammed, A., Hughes, T. G., & Mustapha, A. (2011). The effect of scale on the structural behaviour of masonry under compression. *Construction and Building Materials*, *25*(1), 303–307. https://doi.org/10.1016/j.conbuildmat.2010.06.025
Moncarz, P.D., & Krawinkler H. (1981). *Theory and application of experimental model analysis in earthquake engineering*. Stanford University.
Panagiotou, M., Restrepo, J. I., & Conte, J. P. (2011). Shake-table test of a full-scale 7-story building slice. Phase I: Rectangular wall. *Journal of Structural Engineering*, *137*(6), 691–704.
Parisse, F., Cattari, S., Marques, R., Lourenço, P. B., Magenes, G., Beyer, K., et al. (2021). Benchmarking the seismic assessment of unreinforced masonry buildings from a blind prediction test. In *Structures* (Vol. 31, pp. 982–1005). Elsevier.
Petry, S., & Beyer, K. (2014). Scaling unreinforced masonry for reduced-scale seismic testing. *Bulletin of Earthquake Engineering*, *12*(6), 2557–2581.
Ritter, S. (2017). Experiments in tunnel-soil-structure interaction. *PhD Thesis, University of Cambridge*.
Roy, C. J., & Oberkampf, W. L. (2011). A comprehensive framework for verification, validation, and uncertainty quantification in scientific computing. *Computer Methods in Applied Mechanics and Engineering*, *200*(25–28), 2131–2144.
Schoettler, M., Restrepo, J., Guerrini, G., & Duck, D. E. (2012). A full-scale, single-column bridge bent tested by shake-table excitation.
Swiss RE. (2019). *L ' Aquila , 10 anni dopo*. *Swiss RE Institute* (Vol. 2).
Terzic, V., Schoettler, M. J., Restrepo, J. I., & Mahin, S. A. (2015). Concrete column blind

prediction contest 2010: outcomes and observations. *PEER Report*, *1*, 1–145.

Tomaževič, M., & Velechovsky, T. (1992). Some aspects of testing small-scale masonry building models on simple earthquake simulators. *Earthquake Engineering & Structural Dynamics*, *21*(11), 945–963. https://doi.org/10.1002/eqe.4290211102

Vassiliou, M. F., Cengiz, C., Dietz, M., Dihoru, L., Broccardo, M., Mylonakis, G., et al. (2021a). Dataset from the shake table tests of a rocking podium structure. *Earthquake Spectra*, *37*(3), 2107–2125.

Vassiliou, M. F., Cengiz, C., Dietz, M., Dihoru, L., Broccardo, M., Mylonakis, G., et al. (2021b). Shake table testing of a rocking podium: Results of a blind prediction contest. *Earthquake Engineering & Structural Dynamics*, *50*(4), 1043–1062.

2. Mechanical properties of 3D printed material with binder jet technology and potential applications of additive manufacturing in seismic testing of structures

This chapter consists of the post-print version of the following published article, differing from the original only in terms of layout and formatting:

Del Giudice, L., & Vassiliou, M. F. (2020). Mechanical properties of 3D printed material with binder jet technology and potential applications of additive manufacturing in seismic testing of structures. Additive Manufacturing, 36, 101714.

Available at https://doi.org/10.1016/j.addma.2020.101714

Abstract

Additive manufacturing can be used for the construction of small-scale specimens that are useful for the understanding of the seismic behavior of conventionally constructed masonry structures. In fact, it can provide useful information for the validation of the global level assumptions that numerical models of structures have to make, but are hard to validate as large-scale tests are very expensive. To this end, this paper suggests the use of a Binder Jet printer to manufacture small-scale masonry models. The first step for such a validation procedure is the determination of the mechanical properties of the bulk material printed with a Binder Jet printer. Compression and bending tests on a sand based printer that uses furan binder shows that the bulk material presents anisotropy in compression, but to a lesser degree than other powder based printers. In tension, the anisotropy is found to be statistically insignificant – in stark contrast with values reported in the literature for powder based printers. Aging is found to be crucial for the mechanical properties: They are found to reach a plateau after 15 days of curing time. No scale phenomena were observed for length scales between 50 and 100 mm.

2.1 Introduction

In the last decade the interest and use of additive manufacturing (AM), also referred to as three-dimensional printing (3DP) in nontechnical context (Technologies, 2009) has grown drastically in both research and industry. The first AM process was introduced in the 1980s and it comprised a traced pattern submerged in a liquid polymer. A laser would harden the traced pattern into a layer creating a solid object (Drysdale et al., 1994). Since then, AM technologies have made incredible progresses allowing the use of different materials, e.g. polymers (Ligon et al.,

2017; Stansbury & Idacavage, 2016) , metals (Kalentics et al., 2017; Murr et al., 2012), cementitious (Feng et al., 2015; Salet et al., 2017) and bio materials (Lee et al., 2018) at different scales. A review of terminology related to AM can be found in (Technologies, 2009).

The most well-known application of 3D printing in Construction (Asprone, Auricchio, et al., 2018; Camacho et al., 2018; Gosselin et al., 2016; Kreiger et al., 2019; Sakin & Kiroglu, 2017) has been the attempt to construct Reinforced Concrete buildings by automated procedures (Asprone, Menna, et al., 2018; Bos et al., 2016; Menna et al., 2020). Attempts have also been made to additively manufacture seismic isolation bearings comprising a lattice structure (Amendola et al., 2017). The primary motivation of this paper lies on a different direction: our ultimate goal is not to use additive manufacturing to construct full-scale structures or products, but to create small scale and easily repeatable physical models that can help structural and geotechnical engineers understand better the behavior of the prototype structures.

To our knowledge, the first work on this field involved physical modelling of masonry and was presented by De Jong and Vibert (DeJong & Vibert, 2012), who attempted to understand the seismic behavior of stone masonry spires by studying small-scale 3D printed models. As stresses and elasticity are not considered to be crucial for this specific type of structure, no attempt to preserve similitude of stresses was made and the only important parameter was assumed to be the friction between the blocks – an assumption that cannot be made for ordinary masonry structures. Following this work, Ritter et al. 2018 (Ritter, 2018) physically modelled ordinary masonry to study Soil Structure Interaction problems in a geotechnical centrifuge, a machine that artificially increases gravity to preserve similitude of stresses in small scale testing. The main focus of the work was the soil – not masonry, so a very rough physical approximation of masonry was sufficient. Both above mentioned works used a powder based ZPrinter 350 (now out of the market) that used Binder Jet Technology.

Apart from masonry, 3D printing has been proposed for physical modelling in rocks mechanics (Jiang & Zhao, 2015; Ritter, 2018; Tian & Han, 2017). The aim is to study the influence of cracks and complex geometry on the mechanical behavior of the rock mass, for given mechanical properties of the solid material. Most of the studies related to rock mechanics have used Binder Jet printers, too.

2.2 Additive manufacturing applications in seismic testing

In earthquake engineering numerical models used for the simulation of structures make a set of assumptions to scale up from material- to component-level behavior and a set of assumptions

to scale up from component- to system (global)-level behavior (Figure 1). While a major source of error sources from global assumptions (Bradley, 2013), their experimental validation is not cost effective as it requires shake table testing of a whole structure. Therefore, Del Giudice et al. (Del Giudice et al., 2020) have suggested that the validation of the global level modelling assumptions (for a given component level behavior) can be studied using small scale (1:40) specimens and a geotechnical centrifuge. The bottleneck for the application of this concept to Reinforced Concrete (RC) structures, is the construction of the reinforcing cages by hand (Knappett et al., 2011; Loli et al., 2014). Additive Manufacturing can be used for accurate and rapid production of the steel reinforcement. Figure 2 shows additively manufactured reinforced cages used to construct small-scale specimens by Del Giudice et al. (Del Giudice et al., 2020). Efficient and low cost manufacturing of specimens for seismic testing allows for validation of numerical models in a statistical sense, using multiple virgin specimens and multiple excitations. In certain cases, this statistical approach is necessary in Earthquake Engineering (Bachmann et al., 2018).

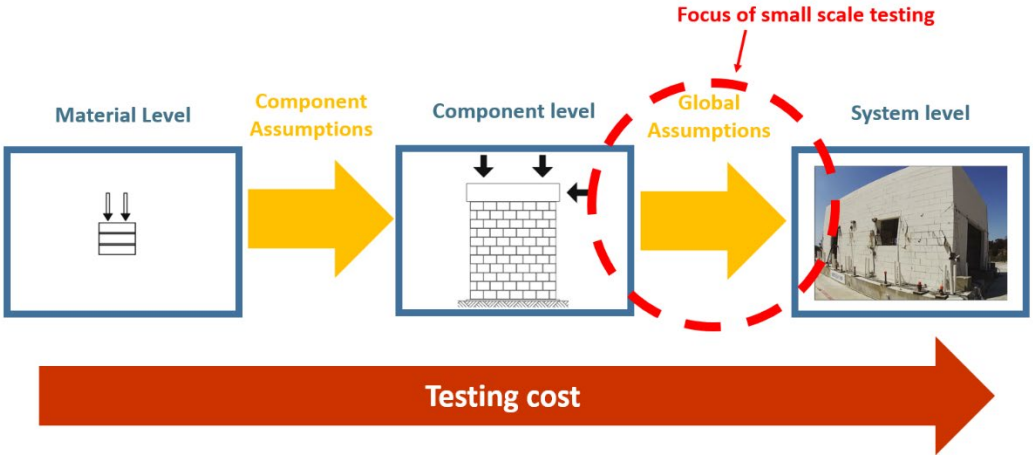

Figure 1. Schematic representation of material to component to system level transition

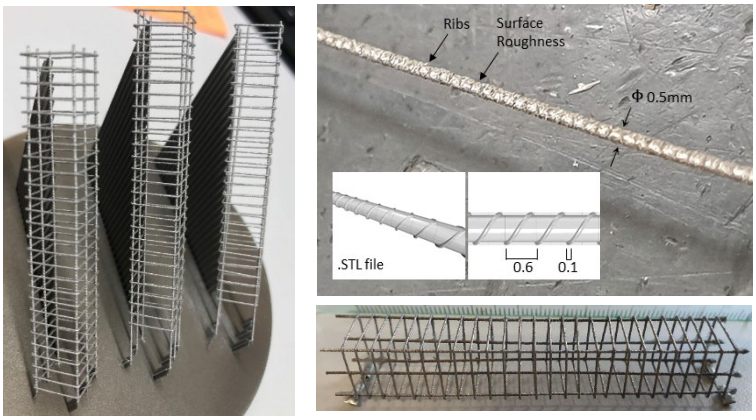

Figure 2. 3D printed reinforcement cage for small scale reinforced concrete testing (Del Giudice et al., 2020).

To expand the above concept to masonry structures, we suggest the use of a Binder Jet printer to manufacture small scale masonry specimens. As masonry comprises both bricks and mortar, the microgeometry in the masonry joints will be controlled by printing micro-notches and micro-shear-keys to emulate mortar joints. To this end, three steps need to be taken: (a) The mechanical properties of the bulk printed material with binder jet technology need to be thoroughly studied. This step has a value on its own and independently of its application in earthquake engineering. (b) Small scale (≤1:10) component level testing (testing of wallets and walls) needs to be performed and the influence of printing notches and shear keys to emulate masonry joints need to be precisely quantified. The tests should be used for determining the component-level input parameters of the numerical models that will be used in the next step. (c) Multiple shake table tests within a geotechnical centrifuge need to be performed so that they serve as dataset for validation of the global level numerical assumptions. This paper focuses on the first step, i.e. it presents experimental results on the mechanical properties of 3D printed material, manufactured with a binder jet printer, a step that has a value on its own, as these properties should be useful for other applications of binder jet additive manufacturing. Steps (b) and (c) are parts of ongoing and future research. More specifically, the main focus of this paper is the anisotropy and aging of the material. A Voxeljet 500 3D printer that is usually employed to create sand-cast molds (Coniglio et al., 2018) is used. This machine can print products up to 500×400×300mm (length×width×height). The printed sand-based material is a rather brittle material with a compressive strength around 5 MPa (Hackney & Wooldridge, 2017), making it qualitatively similar to masonry. This similarity along with the degree of flexibility granted by the process-dependency of printed materials makes it an ideal technology to manufacture masonry-like models.

2.3 3D Printer Technology

2.3.1 Materials

The printed material comprises sand and binder. The sand is a quartz-sand type GS19 with a medium grain size of 190 μm. The binder agent is a furan resin largely composed of furfuryl alcohol whose polymerization is facilitated by a p-toluenesulfonic acid (activator) (McKillip, 1989; Principe et al., 2000) premixed in the sand. More specifically the Furan resin solution is made of Furfuryl Alcohol (70–90%), 4,4'-Isopropylidendiphenol (10–20%), 1, 3-Benzenediol (2.3–3%), and 3-Aminopropyltriethoxysilane (0.1–1%). The precise composition of the solu-

tion is not provided by the manufacturer. The acid activator consists of a mixture of Xylensulphonic acid (46–50%), Toluenesulphonic acid (20–25%), and Sulphuric acid (<2.5%). The printer manufacturer recommends an activator to sand mass ratio between 0.3% and 0.33%. In this work, we used 0.3% of activator to sand mass ratio. Specifically, multiple batches of 50 kg of sand were prepared adding 150 g of activator and mixing for 30 min at 26.5 rpm. The mix was left to rest for 24 h before starting the printing process.

The droplet mass (see next section for definition of droplet) was 101.43 ng for the first two print jobs and 96.22 ng for the third print job.

2.3.2 Printing Process

The printing process consists of two alternating steps: (a) the deposition of the powder bed onto the building area through the recoater; and (b) the selective application of the binder from the print head (Figure 3 and 4).

Figure 3. Voxeljet 500 3D printer.

Unlike other BJ printers that feature a building bin and a feed bin in which the powder supply is stored (Feng et al., 2015), this printer has only one bin, in which the printing process takes place (Figure 3). The sand is delivered by a recoater, which deposits a 300µm thick layer using a vibrating blade at a constant recoating speed of 500mm/s (Figure 3). The vibration of the blade regulates the powder outflow that is essential to have an evenly distributed layer of sand. The recoater is refilled every three deposited layers in the automatic refilling station, which is a screw conveyor that brings the sand from the powder container, placed on top of the

machine to the refilling station (Figure 3, left). After each step, the base of the building bin moves downwards by a distance equal to the layer thickness (300µm) allowing the topmost layer to always be at the same level.

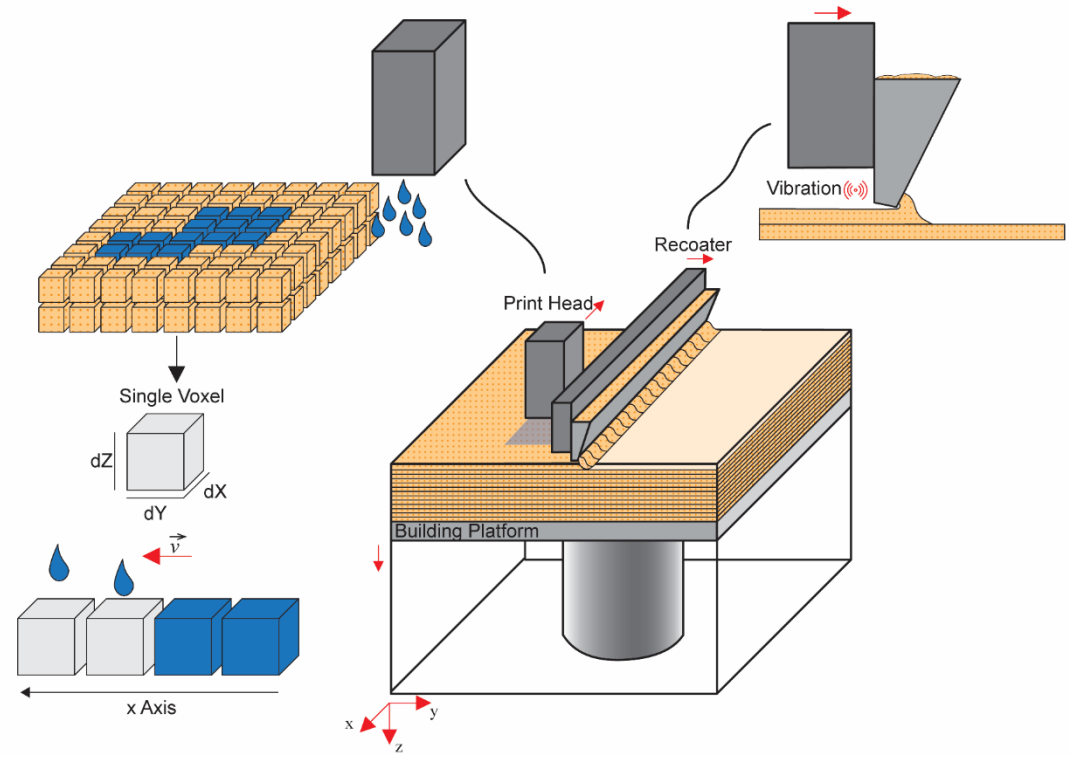

Figure 4. 3D printing process.

The print head (PH) deposits the binder through 768 piezo ceramic nozzles equally distributed on six printing modules on the bottom of the print head. In order to avoid accidental binder spillage from the nozzles a light backpressure of 20 mbar is constantly applied. The piezo ceramic outlets are activated through an electrical pulse. Each pulse creates to a single droplet of binder sprayed from a single nozzle. The pulse voltage can vary from 85.5 to 94.5 V to modify the mass of a single droplet – the higher the voltage the bigger the droplet mass. One droplet is intended to bind only the sand included in one voxel (Kaufman, 1999), which constitutes the basic unit of a three dimensional grid (it is the equivalent of a pixel for a three dimensional space).

2.3.3 Printing directions

With reference to Figure 5, the following coordinate system is defined: Z is the vertical axis. Y is the axis along which the recoater moves. X is the axis that is normal to YZ.

With reference to the coordinate system, the printing process is as follows:

(a) The printhead moves along the X axis and sprays the binder at the points defined by the input file. This defines one strip of the layer.

(b) The printhead moves along the Y axis by a distance equal to the strip, and repeats the procedure to print one more strip.

(c) After covering all the print XY area, the bin moves downwards by dZ=300 μm, the recoater applies one more layer of powder and the process repeats itself.

(d) After a curing time of 12 hours, the printed element is dug out of the bin manually (Figure 3, bottom-left). The part is cleaned in two stages, initially the extra powder is brushed off the part, and then compressed air is used to eliminate any residual powder from the surface of the part.

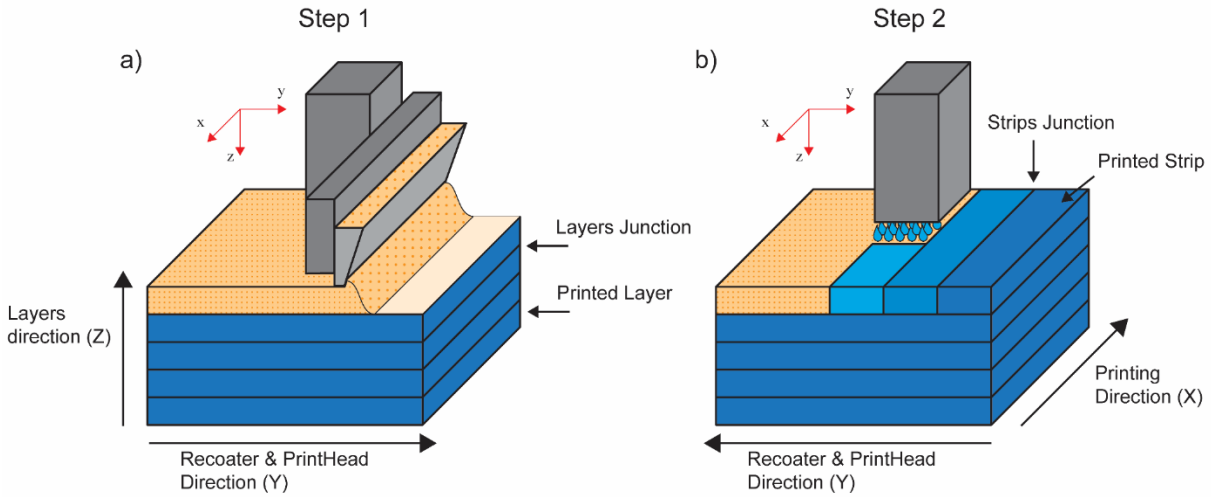

Figure 5. Printing Directions: a) recoating phase, b) binder spraying

The accuracy of the printing process is controlled by the dimension of a single voxel dX×dY×dZ. dZ is fixed and equal to the layer thickness (300 μm). dY is also fixed and it is equal to 85 μm, a value controlled by the accuracy of the recoater in the Y-axis. Finally, dX is variable and can range from 80 to 150 μm. Once the voxel's dimension is set, the pulse frequency, f, and the printing velocity, v, are related through $f = v/dX$. The above printing process should result in a material with orthotropic/anisotropic behavior, as with other Binder Jet printers (Salet et al., 2017).

2.4 Experimental Program

The aim of the experimental program carried herein is to investigate the mechanical behavior of the 3D printed material. Specifically, it aims to assess two aspects: a) the mechanical properties of the bulk 3D printed material along all 3 axis and possible scale/size effects; and b) the

evolution of the mechanical properties with time (aging). To this end, two distinct experimental campaigns were performed.

The anisotropy is assessed performing compression and bending tests on specimens loaded in different directions with respect to the printing directions. The tests were conducted on specimens of different sizes to evaluate any possible scale/size effects.

To assess the aging of the material, we printed 70 cubes and 65 prisms for compression and bending tests respectively, stored them in a room with controlled environmental conditions, and tested them over a thirty-day period.

2.4.1 Specimen Preparation

The specimens were printed in three different print jobs.

The first print job included the cubes used for compression tests. It included 3 different sizes (side length of 50mm, 75mm, and 100mm). For each of the 3 axes (Figure 6a), 4 specimens were printed. In total 3×3×4=36 specimens were printed and tested. Each group of 4 specimens was named according to the size of the cube and to the test orientation. For example, C50X is the group of cubes with a 50mm side that was tested in compression along the X direction. The tests were performed 7 days after printing. The binder that was used in the print job was 1 month old and was to expire 5 months after printing.

The second print job included the prisms used for bending tests. Three size groups were printed: 15x15x60 mm, 40x40x160mm, and 65x65x210mm. In this case, two directions need to be defined: The direction of the longitudinal axis of the specimen and the direction of the loading (Figure 6b), resulting in 6 different test orientations. Three specimens were printed for each test case resulting in a total of 3×6×3=56 specimens. Each group of 3 specimens is named according to the size of the cross section, the longitudinal axis of the prism and the loading direction. For example, B40XY is the group of prisms with cross section 40 by 40 mm, printed with a longitudinal axis along the Y printing direction and loaded along the X printing direction. The tests were performed 7 days after printing. The binder that was used in the print job was 1.5 months old and was to expire 4.5 months after printing.

The third print job included the specimens to study the evolution of compression and tension strength with time. To this end, there were printed a) 70 cubes with edge length of 50mm; and b) 65 prisms of 40x40x160mm. The binder that was used in the print job was 3 months old and was to expire 3 months after printing. The specimens were stored in a controlled

environmental conditions room, i.e. 55% relative humidity and 20±2 C°. These specimens were printed and tested along only one direction. One can assume that the evolution of strength with time along the other directions follows a similar pattern.

It is reasonable to assume that the mechanical properties of the bulk material depend on the binder to sand ratio. Therefore, the printing parameters were specifically tuned in order to obtain the same binder percentage in all print jobs. The printing settings are summarized in the Table 1.

2.4.2 Mechanical Tests

2.4.2.1 Uniaxial Compression Test

The characterization of the uniaxial compressive strength of the specimens was performed in accordance to ASTM C109/C109M-20 (ASTM International, 2020). The tests were carried out with a Universal Testing Machine (UTM) from Zwick/Roell Retroline equipped with a 200kN Load Cell. The tests were performed in displacement control at a constant strain rate of 0.01 s^{-1} in all specimens and all sizes. Figure 7 shows the testing rig used for compression tests.

		Print Job 1	Print Job 2	Print Job 3
Print Speed	[m/s]	0.38	0.38	0.36
Frequency	[Hz]	4000	4000	4000
dX Resolution	[µm]	95	95	90
Pulse Voltage	[V]	89.6	89.6	89.6
Droplet Mass	[ng]	101.43	101.43	96.22
Binder mass ratio (m_{binder}/m_{total})	[%]	2.125	2.125	2.128
Binder volumetric ratio (V_{binder}/V_{total})	[%]	1.699	1.699	1.672
Recoating Speed	[m/s]	0.5	0.5	0.5

Table 1. Printer parameters.

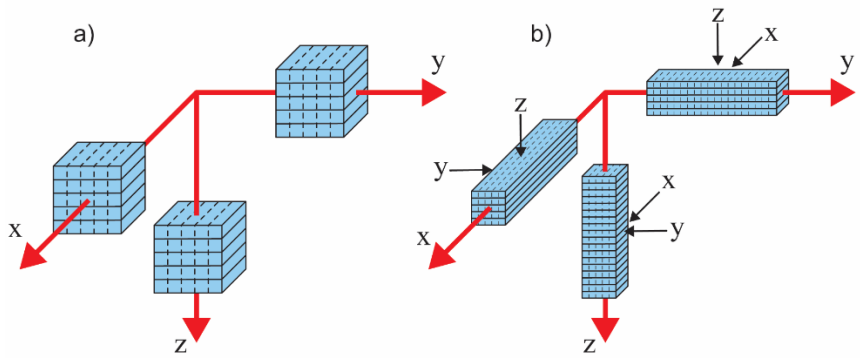

Figure 6. Loading Directions, a) compression test, b) bending test.

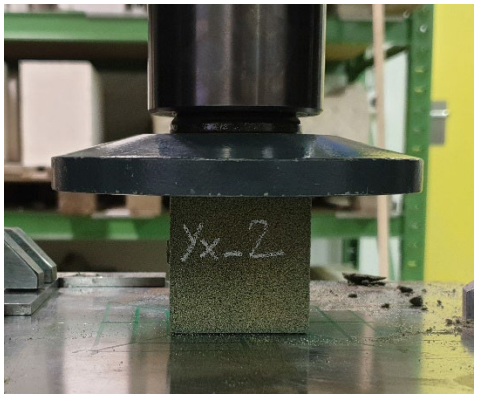

Figure 7. Compression Test.

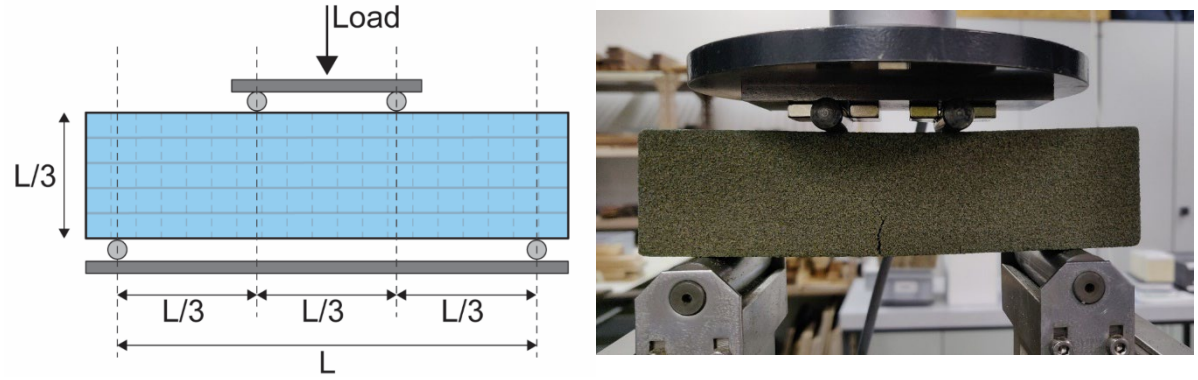

Figure 8. **a)** Four Point Bending Test Setup; **b)** Four Point Bending Test.

2.4.2.2 **Four Point Bending Tests**

The flexural strength of the 3D printed material was assessed through 4 point bending tests. The reference standard for these tests is ASTM C78/C78M-18 (ASTM International, 2018). According to the latter, the span length, L, must be 3 times the height of the cross section, d (Figure 8). The ratio d / L has been kept constant for all specimens, e.g. the specimens with cross section height d = 15 mm, were tested with a loading span of 45mm, whereas those with d = 65 mm were tested with L = 195mm. The UTM used for the bending tests is a Zwick 1454, equipped with a 10kN load cell. We used a different testing rig because the 10kN load cell is more accurate in measuring small loads.

2.5 Results and discussion

2.5.1 Mechanical properties and scale/size effects

2.5.1.1 **Compression tests**

The results are divided in groups by loading orientation and size. The failure mode is the same for all tests regardless of the loading configuration and of the size. Two types of failure are

observed: a) explosive failure; and b) distributed cracks on the four vertical faces of the specimens, in accordance to (EN, 2002). No correlation between the mode of failure and the specimen configuration was observed. Figure 9 shows a typical crack pattern of specimens with different configurations and size.

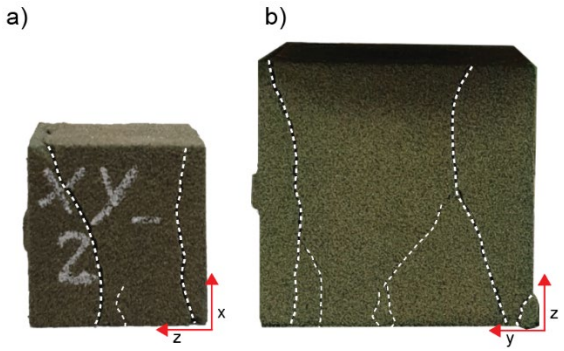

Figure 9. a) Failure of 50mm cubic specimen loaded in X direction. **b)** Failure of 75mm cubic specimen loaded in Z direction.

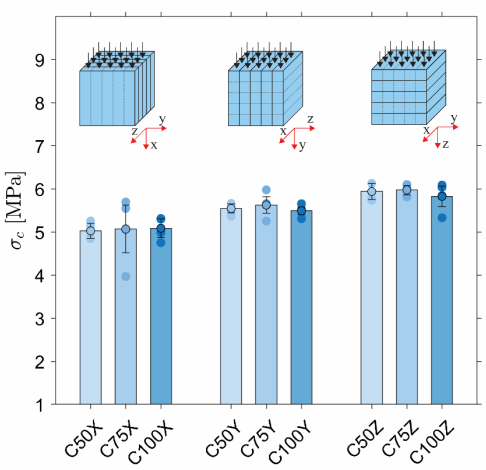

Figure 10. Compression Strength for different orientations. Naming example: C75X is a cube with a side 75mm loaded along the x direction. All specimens have been cured for 7 days.

Figure 10 shows the observed strength, defined as the maximum-recorded force divided by the area of a side of the cube. The circles represent the strength observed in each test, while the bars the mean value of each group. The error lines plot the 25th and 75th percentiles of the strength. Cubes loaded in direction X, Y, and Z have an average compressive strength of 5.05MPa (CoV of 8.81%), 5.55MPa (CoV of 3.52%), and 5.90MPa (CoV of 4.10%) respectively. This indicates that there is a difference in average strength with respect to the loading orientation. Note that these average values per direction include all specimens of all sizes.

To formally verify the dependence of compression strength on printing orientation, a one-way Analysis of Variance (ANOVA) was performed (Montgomery & Runger, 2010). The

different orientations were regarded as the levels of the treatment in the experiments, therefore there is one factor (i.e. orientation), and three levels, (i.e. X, Y, and Z).

In this approach, two hypotheses, H_0 (which is tested) and its opposite H_1, are considered. The tested null hypothesis H_0 is rejected when the *p*-value of the hypothesis test is lower than a given statistical significance threshold α_s. A fairly large value of statistical significance of 0.1 is used to allow for a nuanced qualification of null hypothesis validity using an evidence classification scale shown in Table 2. A detailed explanation of hypothesis testing procedures can be found in (Wasserman, 2013). In this case the null hypothesis H_o is that the mean value of the compressive strength for all treatment is the same.

p-value	Evidence
<0.01	Very strong against H_o
0.01-0.05	Strong against H_o
0.05-0.10	Medium – weak against H_o
>0.10	Small or none against H_o

Table 2. Evidence classification p-value scale (Wasserman, 2013).

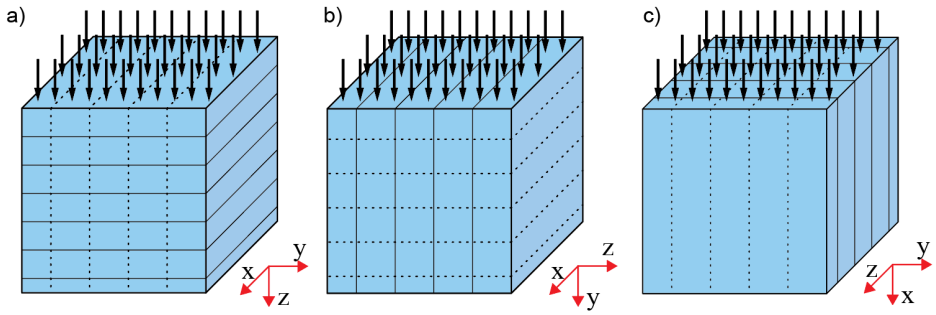

Figure 11. Loading Orientations: a) Z, b) Y, c) X

The analysis of variance produced a p-value of 1.54E-06, meaning that there is very strong evidence against H_o, i.e. against compression strength being independent of the direction. Therefore, the difference in strength is statistically significant and the material is clearly anisotropic. However, the anisotropy in compression strength is significantly smaller than the one reported by Feng et al. (Feng et al., 2015) (who used a different printer). The difference in compression strength among the three directions reported herein is less than 20%, while Feng et al. report differences as high as 55%.

The results show that specimens loading along the Z orientation exhibited the maximum strength. This emphasizes the role of the printing process in the mechanical strength of the material. The joints between subsequent layers and adjacent strips can be considered as weak links that affect the overall mechanical behavior of the printed parts.

To evaluate any possible scale/size effect, we performed an ANOVA assuming the size as factor of interest. Then the null hypothesis H_o tested is that the compression strength is independent of the size of the specimen. Three ANOVAs were performed; one for each direction. The p-values are 0.98, 0.66, and 0.72, for the samples loaded along X, Y, and Z, respectively. All p values are larger than 0.10 indicating that there is small or none evidence against H_o. Hence, it is concluded that for the samples considered, size does not influence the compression strength of the material. This contradicts the results of Feng et al. (Feng et al., 2015) where 50mm cubic specimens were significantly stronger than 70.7mm ones.

2.5.1.2 **Bending tests**

The specimens exhibited a brittle behavior. No evident cracks were visible until the maximum load was attained. Once the maximum load was reached, a crack initiated at the bottom of specimen within the load span. The crack propagated instantaneously through the specimen dividing the prism in two. The failure mode was the same for all specimens and no differences along different loading directions were observed.

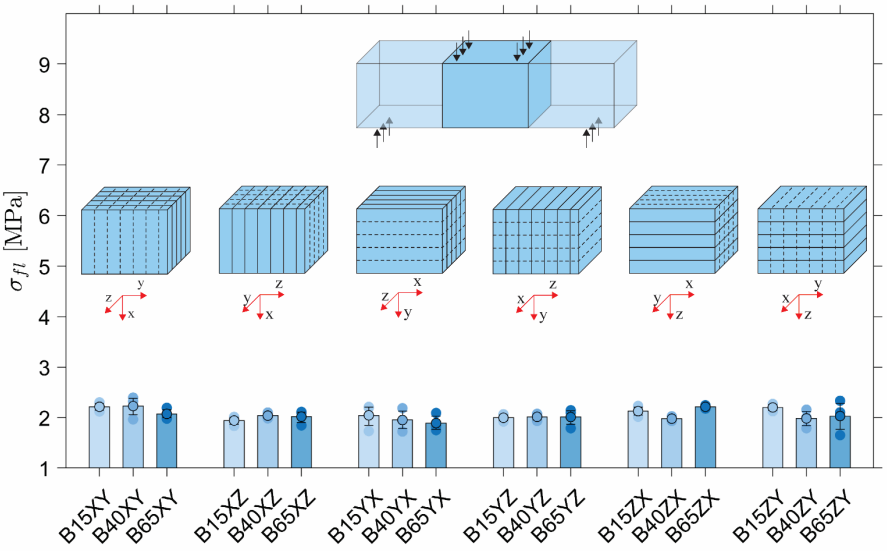

Figure 12. Tensile Strength for different orientations. Naming example: B40XY is a prism with a cross section of 40 by 40mm loaded along the x printing direction, while its longitudinal axis lies on the y printing direction. All specimens have been cured for 7 days.

The maximum tension stress in the material was computed according to:

$$\sigma_{fl} = \frac{F\,L}{b^3}$$

where, F is the load applied by the actuator, L is the span length (Figure 8), and b is the side length of the square cross section. Figure 12 reports the calculated flexural strength for each

test as well as the 25th, 50th, and the 75th percentile for each configuration. Specimens loaded in XY, XZ, YX, YZ, ZX, and ZY direction have a mean flexural strength of 2.16MPa (CoV 1.1%), 1.99MPa (CoV 0.5%), 1.96MPa (2.2%), 2MPa (CoV 0.6%), 2.1MPa (CoV 0.6%), and 2MPa (CoV 2%) respectively. Figure 12 suggests that the printing orientation does not seem to influence the tension strength. This is tested with a one-way ANOVA in which the specimen configurations are considered as different levels, and the null hypothesis H_o refers to the equality of the mean flexural strength along different directions. The ANOVA yielded a p-value of 0.078, which according to Table 2, indicates medium or weak evidence against the null hypothesis.

Moreover, a Tukey-Kramer (Tukey, 1977) multiple comparison tests, at a 5% level of significance was performed to verify that all mean values are different. All 15 combinations are tested. For each combination, the null hypothesis H_o tested is that the flexural strength is independent of the configuration. The results of the tests are offered in Table 3 and show that in all combinations there is little to none evidence against H_o. Therefore, it can be concluded that the flexural strength is independent of the printing orientation and that there is no anisotropy in terms of flexural strength. This is in stark contrast to the results reported by Feng et al. (Feng et al., 2015) where the flexural strength for tension normal to the printing layers is more than 10 times larger than the one within the printing layers. Evidently, the two printing methods and setups produce very different materials, because they use different binders and powders resulting into different chemical reaction rates: In the case of Feng et al. [8] the time interval between the two layers is significant compared to the time it takes for the chemical reactions

First Element	Second Element	Lower Bound	Mean Difference	Upper Bound	p-value
B-XY	B-XZ	-0.052	0.172	0.397	0.223
B-XY	B-YX	-0.016	0.209	0.434	0.082
B-XY	B-YZ	-0.060	0.165	0.389	0.269
B-XY	B-ZX	-0.160	0.065	0.290	0.954
B-XY	B-ZY	-0.125	0.100	0.325	0.770
B-XZ	B-YX	-0.188	0.037	0.261	0.997
B-XZ	B-YZ	-0.233	-0.008	0.217	1.000
B-XZ	B-ZX	-0.332	-0.107	0.118	0.717
B-XZ	B-ZY	-0.297	-0.072	0.153	0.930
B-YX	B-YZ	-0.269	-0.045	0.180	0.991
B-YX	B-ZX	-0.369	-0.144	0.081	0.415
B-YX	B-ZY	-0.334	-0.109	0.116	0.705
B-YZ	B-ZX	-0.324	-0.099	0.125	0.777
B-YZ	B-ZY	-0.289	-0.064	0.161	0.957
B-ZX	B-ZY	-0.190	0.035	0.260	0.997

Table 3. Tukey-Kramer Pair-Wise comparison.

to evolve, while this is less pronounced in the case of the sand and binder used in this work. La Grange et al. (La Grange et al., 2018) performed a series of 3 point bending tests on specimens printed with a Voxeljet1000 printer. The printer is the same with the one used in this study; yet of larger size. They used the same binder, but do not report details on the sand they used. Instead of letting the specimens cure at 55% relative humidity and 20±2 C°, they cured them at 110ºC for 2 hours. They report 25% higher values of strength. Therefore, it can be confirmed that the strength of the bulk material also depends on curing process and sand.

2.5.2 Aging of the material

Preliminary tests showed that the strength of the printed bulk material strongly depends on curing time. Primkulov et al. (Primkulov et al., 2017) have studied the influence of different curing temperatures and times on the compression strength of material printed with binder jet technology and cured in the oven. However, to the authors' knowledge, aging in terms of both compression and bending strength under room conditions has not been discussed. Therefore, this section explores the strength of the bulk material as a function of curing time by means of uniaxial compression and four point bending tests. One size and one loading direction was chosen for all specimens, assuming that aging is neither strongly size-dependent nor loading-direction-dependent. For the uniaxial compression tests, 70 cubes of side length 50mm were printed. The cubes were tested along the Z printing direction, which is the direction of maximum strength for the material. For the bending tests, 65 prisms of 40x40x160mm were printed. The specimens were of the "ZX" configuration, i.e. the loading direction lies along the Z printing axis while the longitudinal axis of the prism is parallel to the X printing axis.

Compression and bending tests were conducted every 12 hours for the first two days and then every two-three days. Figure 13 shows the force - deformation curve for indicative tests performed after different curing time. The force was measured with a load cell, while the deformation was measured through the vertical stroke of the actuator. It is evident that the specimens tested within the first two-three days in compression exhibited a ductile failure in contrast to all the other specimens, which failed in brittle manner. After the first days, all specimens were substantially less deformable and they exhibited either explosive failure or distributed cracks on the vertical faces of the cube, as described in the European standard (EN, 2002) and shown in Figure 8.

Bending tests showed that there is a clear difference in failure mechanism between short-cured (up to three days of curing) and long-cured specimens (cured for more than 3 days).

Testing of the short-cured specimens showed that a crack forms at the bottom of the specimen once the maximum load is attained. Then, the crack slowly propagates in the vertical direction (Figure 14a).

Long-cured specimens, showed an abrupt failure once the maximum load was reached. The failure corresponded to the onset of a sharp vertical crack dividing the specimens in two halves (Figure 14b). The compressive and flexural strength of all specimens are reported in Table 4 and plotted against time in Figure 15. It is clear that both compressive and flexural strength strongly depend on the curing time. The strength grows rapidly within the first 2 days after the end of the printing process. The secant rate of growth during the first 2 days is 1.8MPa/day and 0.58 MPa/day for compressive and flexural strength respectively, reaching an average strength of 3.6MPa and 1.02MPa, in compression and bending. After this rapid increase the secant rate of strength increase from day 2 to day 15 slows down to 0.10 MPa/day and 0.035 MPa/day, in compression and bending respectively. From the 15th day, the compressive and tension strengths reaches a plateau of 5MPa and 1.5 MPa respectively. Therefore, it is concluded that it takes 15 days for the material compression and tension strength to stabilize, at least for the length scales considered. The aging of the 3D printed material, i.e. the strength build up over time, can be related to the kinetic of the polymerization.

(Guigo et al., 2007) studied the kinetic of acid catalyzed Furfuryl alcohol polymerization both in isothermal and non-isothermal conditions. They found that in isothermal curing the kinetic of the polymerization follows a linear behavior until reaching a plateau. This behavior is comparable to the strength build-up observed for the 3D printed material object of the herein study.

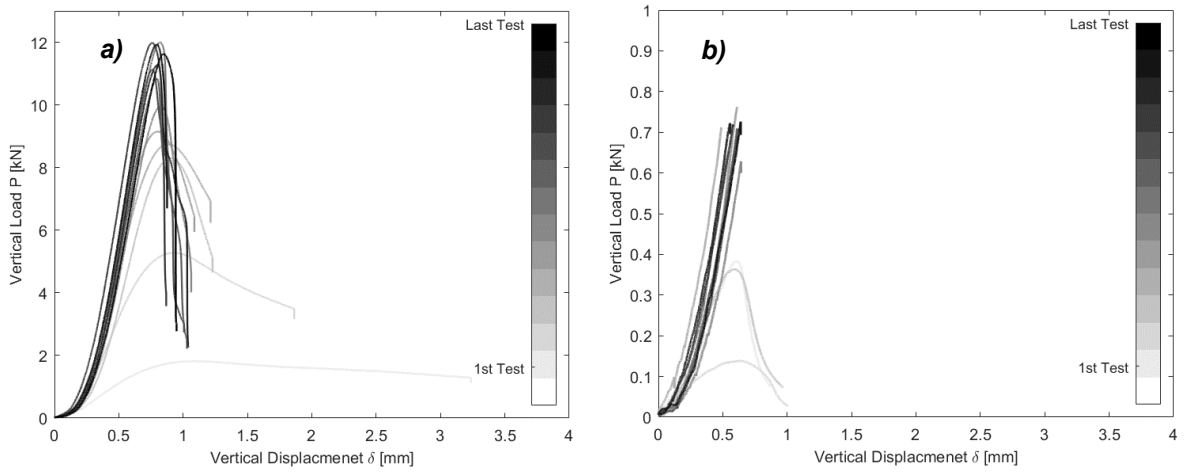

Figure 13. Load-Displacement Curves at different curing time. **a)** Compression tests. **b)** Bending tests

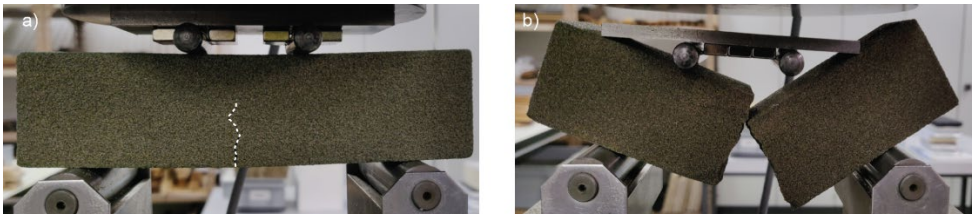

Figure 14. a) Crack pattern young specimens. **b)** Sudden failure of old specimens.

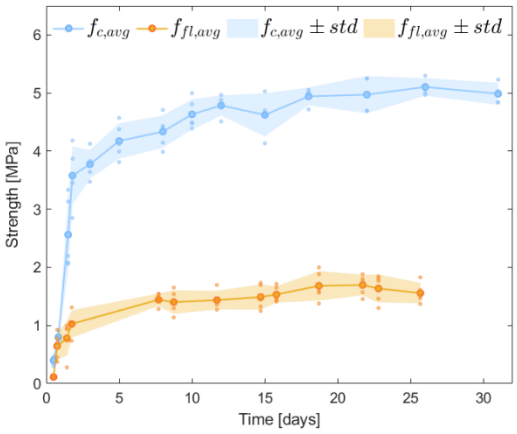

Figure 15. Strength build-up over time.

The strength obtained during the aging tests (3rd print job) after 7 days is smaller than the strength obtained during the compression and tension tests (1st and 2nd print job). This can be attributed to the binder being 1.5 months older and closer to its expiration date. Therefore, it should be concluded that the mechanical properties also depend on the age of the binder at the time of the print.

	Compressive Strength		Flexural Strength	
Time Days	Mean [MPa]	CoV [%]	Mean [MPa]	CoV [%]
0.5	0.40	17.75	0.11	18.29
1	0.80	9.07	0.65	35.56
1.5	2.56	24.18	0.78	37.98
2	3.58	13.94	1.03	22.85
3	3.77	6.44	-	-
5	4.17	7.25	-	-
8	4.34	6.41	1.44	7.35
9	-	-	1.40	14.38
10	4.63	5.56	-	-
12	4.79	3.61	1.44	11.17
15	4.46	11.02	1.49	14.59
-	-	-	1.53	9.15
18	4.94	3.08	-	-
-	-	-	1.68	15.06
22	4.97	6.44	1.70	10.41
-	-	-	1.64	14.75
26	5.10	2.92	1.56	11.20
31	4.99	3.78	-	-

Table 4. Compressive and Flexural Strength with respect to curing time

2.6 Conclusions

3D printing can be useful in earthquake engineering. In particular, it can be used for the manufacturing of small- scale physical models of structures. Testing the physical models in a geotechnical centrifuge can provide valuable datasets for the validation of the global level assumptions often done in simulations of the seismic response of structures. Binder Jet technology shows potential for the manufacturing of small-scale models of masonry structures, as its compressive strength is similar to masonry.

This paper studied the compressive and tensile behavior of the material printed with a Voxeljet 500 sand based printer using a furan binder. Compression and bending tests were performed along the different printing directions. Unlike materials tested in previous studies, the compressive strength only loosely depends on the printing orientation while the tensile strength shows no statistical significance on orientation. Therefore it is lowly anisotropic. Compressive and tensile strength lie on the order of 5-6 MPa (depending on orientation) and 1.5MPa respectively. Both depend on the age of the binder at the printing time.

Moreover, this paper explored the aging of the printed material. It showed that under room conditions of 55% relative humidity and 20±2 C°, it takes 15 days for the compressive and bending strength of the material to reach a plateau.

No scale/size phenomena were observed for cubes with sides between 50 and 100mm.

Declaration of competing interests

The author declare that they have no known competing financial interests or personal relationships that could have appeared to influence the work reported in this paper.

Acknowledgments

The tests to evaluate the aging of the material were performed by ETH students Liliana Florez Hernandez, Eliane Kalberer, Franziska Siegenthaler, and Linghang Sun within the framework of their Master's Project.

Luigi D'Avico, PhD student in the Physical Chemistry of Building Materials of the ETH, assisted with the chemistry related part of the paper.

This work was supported by the European Research Council (ERC) under Starting Grant 803908. The methods, results, opinions, findings, and conclusions presented in this report are those of the authors and do not necessarily reflect the views of the funding agency.

References

Amendola, A., Benzoni, G., & Fraternali, F. (2017). Non-linear elastic response of layered structures, alternating pentamode lattices and confinement plates. *Composites Part B: Engineering*, *115*, 117–123.

Asprone, D., Auricchio, F., Menna, C., & Mercuri, V. (2018). 3D printing of reinforced concrete elements: Technology and design approach. *Construction and Building Materials*, *165*, 218–231. https://doi.org/10.1016/j.conbuildmat.2018.01.018

Asprone, D., Menna, C., Bos, F. P., Salet, T. A. M., Mata-Falcón, J., & Kaufmann, W. (2018). Rethinking reinforcement for digital fabrication with concrete. *Cement and Concrete Research*, *112*, 111–121. https://doi.org/10.1016/J.CEMCONRES.2018.05.020

ASTM International. (2018). *C78/C78M-18 Standard Test Method for Flexural Strength of Concrete (Using Simple Beam with Third-Point Loading). ASTM International*. West Conshohocken, PA. https://doi.org/https://doi.org/10.1520/C0078_C0078M-18

ASTM International. (2020). *C109/109M-20 Standard Test Method for Compressive Strength of Hydraulic Cement Mortars (Using 2-in . or [50-mm] Cube Specimens). ASTM International*. West Conshohocken, PA. https://doi.org/https://doi.org/10.1520/C0109_C0109M-20

Bachmann, J. A., Strand, M., Vassiliou, M. F., Broccardo, M., & Stojadinović, B. (2018). Is rocking motion predictable? *Earthquake Engineering and Structural Dynamics*, *47*(2), 535–552. https://doi.org/10.1002/eqe.2978

Bos, F., Wolfs, R., Ahmed, Z., & Salet, T. (2016). Additive manufacturing of concrete in construction: potentials and challenges of 3D concrete printing. *Virtual and Physical Prototyping*, *11*(3), 209–225. https://doi.org/10.1080/17452759.2016.1209867

Bradley, B. A. (2013). A critical examination of seismic response uncertainty analysis in earthquake engineering. *Earthquake Engineering & Structural Dynamics*, *42*(11), 1717–1729.

Camacho, D. D., Clayton, P., O'Brien, W. J., Seepersad, C., Juenger, M., Ferron, R., & Salamone, S. (2018). Applications of additive manufacturing in the construction industry–A forward-looking review. *Automation in Construction*, *89*, 110–119.

Coniglio, N., Sivarupan, T., & El Mansori, M. (2018). Investigation of process parameter effect on anisotropic properties of 3D printed sand molds. *International Journal of Advanced Manufacturing Technology*, *94*(5–8), 2175–2185. https://doi.org/10.1007/s00170-017-0861-5

DeJong, M. J., & Vibert, C. (2012). Seismic response of stone masonry spires: Computational and experimental modeling. *Engineering Structures*, *40*, 566–574.

Drysdale, R. G., Hamid, A. A., & Baker, L. R. (1994). *Masonry structures: behavior and design*.

EN, B. S. (2002). 12390-3. Testing hardened concrete; part 3: compressive strength of test specimens. *British Standards Institution*.

Feng, P., Meng, X., Chen, J.-F., & Ye, L. (2015). Mechanical properties of structures 3D printed with cementitious powders. *Construction and Building Materials*, *93*, 486–497. https://doi.org/10.1016/J.CONBUILDMAT.2015.05.132

Del Giudice, L., Wrobel, R., Leinenbach, C., & Vassiliou, M. F. (2020). Static Testing of Additively Manufactured Microreinforced Concrete Specimens for Statistical Structural Model Validation at a Small Scale. In *8th International Conference on Advances in Experimental Structural Engineering (8AESE)*.

Gosselin, C., Duballet, R., Roux, P., Gaudillière, N., Dirrenberger, J., & Morel, P. (2016). Large-scale 3D printing of ultra-high performance concrete – a new processing route for architects and builders. *Materials & Design*, *100*, 102–109.

https://doi.org/10.1016/J.MATDES.2016.03.097

La Grange, J. J., Nyembwe, K., Van Tonder, P. J. M., De Beer, D. J., & Van Wyk, T. (2018). Determining the effect of three-dimensional printing orientation on the bending strength of sand moulds and cores when using a voxeljet additive manufacturing machine.

Guigo, N., Mija, A., Vincent, L., & Sbirrazzuoli, N. (2007). Chemorheological analysis and model-free kinetics of acid catalysed furfuryl alcohol polymerization. *Physical Chemistry Chemical Physics*, *9*(39), 5359–5366.

Hackney, P. M., & Wooldridge, R. (2017). Characterisation of direct 3D sand printing process for the production of sand cast mould tools. *Rapid Prototyping Journal*, *23*(1), 7–15. https://doi.org/10.1108/RPJ-08-2014-0101

Jiang, C., & Zhao, G. F. (2015). A Preliminary Study of 3D Printing on Rock Mechanics. *Rock Mechanics and Rock Engineering*, *48*(3), 1041–1050. https://doi.org/10.1007/s00603-014-0612-y

Kalentics, N., Boillat, E., Peyre, P., Gorny, C., Kenel, C., Leinenbach, C., et al. (2017). 3D Laser Shock Peening – A new method for the 3D control of residual stresses in Selective Laser Melting. *Materials and Design*, *130*, 350–356. https://doi.org/10.1016/j.matdes.2017.05.083

Kaufman, A. E. (1999). Introduction to volume graphics. In *SIGGRAPH* (Vol. 99, pp. 24–47).

Knappett, J. A., Reid, C., Kinmond, S., & O'Reilly, K. (2011). Small-scale modeling of reinforced concrete structural elements for use in a geotechnical centrifuge. *Journal of Structural Engineering*, *137*(11), 1263–1271.

Kreiger, E. L., Kreiger, M. A., & Case, M. P. (2019). Development of the construction processes for reinforced additively constructed concrete. *Additive Manufacturing*, *28*, 39–49.

Lee, J. M., Sing, S. L., Zhou, M., & Yeong, W. Y. (2018). 3D bioprinting processes: A perspective on classification and terminology.

Ligon, S. C., Liska, R., Stampfl, J., Gurr, M., & Mülhaupt, R. (2017, August 9). Polymers for 3D Printing and Customized Additive Manufacturing. *Chemical Reviews*. American Chemical Society. https://doi.org/10.1021/acs.chemrev.7b00074

Loli, M., Knappett, J. A., Brown, M. J., Anastasopoulos, I., & Gazetas, G. (2014). Centrifuge modeling of rocking-isolated inelastic RC bridge piers. *Earthquake Engineering & Structural Dynamics*, *43*(15), 2341–2359.

McKillip, W. J. (1989). Chemistry of Furan Polymers (pp. 408–423). https://doi.org/10.1021/bk-1989-0385.ch029

Menna, C., Mata-Falcón, J., Bos, F. P., Vantyghem, G., Ferrara, L., Asprone, D., et al. (2020). Opportunities and challenges for structural engineering of digitally fabricated concrete. *Cement and Concrete Research*, *133*, 106079.

Montgomery, D. C., & Runger, G. C. (2010). *Applied statistics and probability for engineers*. John Wiley & Sons.

Murr, L. E., Martinez, E., Amato, K. N., Gaytan, S. M., Hernandez, J., Ramirez, D. A., et al. (2012). Fabrication of metal and alloy components by additive manufacturing: Examples of 3D materials science. *Journal of Materials Research and Technology*. Elsevier Editora Ltda. https://doi.org/10.1016/S2238-7854(12)70009-1

Primkulov, B., Chalaturnyk, J., Chalaturnyk, R., & Zambrano Narvaez, G. (2017). 3D Printed Sandstone Strength: Curing of Furfuryl Alcohol Resin-Based Sandstones. *3D Printing and Additive Manufacturing*, *4*(3), 149–156. https://doi.org/10.1089/3dp.2017.0032

Principe, M., Martínez, R., Ortiz, P., & Rieumont, J. (2000). The polymerization of furfuryl alcohol with p-toluenesulfonic acid: photocross-linkeable feature of the polymer. *Polímeros*, *10*(1), 8–14.

Ritter, S. (2018). Experiments in tunnel-soil-structure interaction. University of Cambridge.

Sakin, M., & Kiroglu, Y. C. (2017). 3D Printing of Buildings: Construction of the Sustainable Houses of the Future by BIM. *Energy Procedia*, *134*, 702–711. https://doi.org/10.1016/J.EGYPRO.2017.09.562

Salet, T. A. M., Bos, F. P., Wolfs, R. J. M., & Ahmed, Z. Y. (2017). 3D concrete printing–a structural engineering perspective. In *2017 fib Symposium-High Tech Concrete: Where Technology and Engineering Meet* (pp. xliii–lvii). Springer.

Stansbury, J. W., & Idacavage, M. J. (2016). 3D printing with polymers: Challenges among expanding options and opportunities. In *Dental Materials* (Vol. 32, pp. 54–64). Elsevier Inc. https://doi.org/10.1016/j.dental.2015.09.018

Technologies, A. C. F. on A. M. (2009). Standard terminology for additive manufacturing—general principles and terminology. ISO/ASTM52900-15.

Tian, W., & Han, N. V. (2017). Mechanical properties of rock specimens containing pre-existing flaws with 3 D printed materials. *Strain*, *53*(6), e12240.

Tukey, J. W. (1977). *Exploratory data analysis* (Vol. 2). Reading, Mass.

Wasserman, L. (2013). *All of statistics: a concise course in statistical inference*. Springer Science & Business Media.

3. Global sensitivity analysis of 3D printed material with binder jet technology by using surrogate modeling and polynomial chaos expansion

This chapter consists of the pre-print version of the following accepted article, differing from the original only in terms of layout and formatting:

Del Giudice, L., Sudret, B., Marelli, S., & Vassiliou, M. F. (2023). Mechanical properties of 3D printed material with binder jet technology and potential applications of additive manufacturing in seismic testing of structures. Progress in Additive Manufacturing.

Available at https://doi.org/10.1007/s40964-023-00459-y

Abstract

The mechanical properties of 3D printed materials produced with additive manufacturing depend on the printing process, which is controlled by several tuning parameters. This paper focuses on Binder Jet technology and studies the influence of printing resolution, activator percentage, droplet mass, and printing speed on the compressive and flexural strength, as well as on the Young's modulus of the bulk printed material. As the number of tests required using a one factor at a time approach is not time efficient, a Design of Experiments approach was applied and optimal points in the 4-dimensional parameter space were selected. Then Sobol' sensitivity indices were calculated for each mechanical property through polynomial chaos expansion. We found that the mechanical properties are primarily controlled by the binder content of the bulk material, namely printing resolution and droplet mass. A smaller dependence on the activator percentage was also found. The printing speed does not affect the mechanical properties studied. In parallel, curing of the specimens at 80 to 115 ºC for 30 to 120 minutes increases their strength.

3.1 Introduction

Since it was introduced in the 1980s (Wohlers, 2014), additive manufacturing (AM) has evolved in what is considered by many to be a disrupting technology bound to change the manufacturing process in several industries (Shahrubudin et al., 2019). Additive manufacturing technology is also referred to as three-dimensional printing (3DP), or rapid prototyping (ISO/ASTM52900-15, 2009), although the latter is nowadays considered to be misleading.

While 3DP is still used to manufacture unique prototypes, it is also used to manufacture production parts made out of a wide variety of materials, e.g., polymers (Ligon et al., 2017; Stansbury & Idacavage, 2016), metals (Murr, 2015), and cementitious materials (Feng et al., 2015). AM has recently found applications in different industries like Civil Engineering by means of concrete 3D printers (Asprone et al., 2018; Bos et al., 2016; Camacho et al., 2018; Menna et al., 2020). It has also been used in Civil and Seismic Engineering as a tool to create small-scale physical models of reinforced concrete (Del Giudice et al., 2021, 2022), masonry structures (DeJong & Vibert, 2012; Ritter, 2017), and rock specimens (Jiang & Zhao, 2015; Primkulov et al., 2017).

3D printed material properties depend not only on the type of the raw material used, but also on the parameters of the printing process. In fact, regardless of the type of technology employed (fused-deposited-material, binder jetting, selective laser sintering, etc.), all 3D printers have a multitude of parameters ("input" of the printing process) that can be tuned, which in turn affect the characteristics of the printed material. For instance, fused-deposited-material (FDM) 3D printers allow the user to choose between different filament materials and diameters, nozzle size and shape, layer height, type of infill pattern, printing temperature, printing speed, etc. (Aw et al., 2018; Mueller et al., 2015). Other printing technologies involve different parameters; nonetheless, the characteristics of the printed materials are all affected by the printing process parameters. Therefore, it is important to quantify the effect that the input parameters have on the output properties (i.e. the properties of the printed material), and consequently to optimize the input parameters to yield optimal characteristics for each application. Depending on the application, it could be of interest to maximize the mechanical performance of the printed material (e.g. tensile strength, compressive strength, stiffness etc.), to improve its thermal performance (e.g. thermal conductivity, thermal capacity, etc.), or to yield the best finish quality of the printed parts. Therefore, performing a sensitivity analysis to find the weight that each printing parameter has on the output quantity of interest is a critical step to optimize the manufacturing process.

The simplest type of study to assess the influence of an input parameter would be a one-factor-at-the-time (OFAT) approach, which consists of changing one input parameter while keeping all the others constant. This approach, although of simple conception, comes at the expense of a very high experimental cost (Montgomery, 2017), as the required tests linearly increase with the number of input parameters that need to be explored. More efficient and cost-effective experimental studies have been already used to characterize the properties of 3D

printed parts. Mueller et al. 2015 (Mueller et al., 2015) used a Design of Experiment (DoE) approach to create and efficient experimental design and used Analysis of Variance (ANOVA) (Antony, 2014; Montgomery, 2017) to quantify the effect of the printing parameters on the mechanical properties of parts manufactured with inkjet 3D printing technology. Xiao et al. 2019 (Xiao et al., 2019), focused on the process parameter optimization of 3D printed continuous fiber/epoxy composites (CCD/EPCs) using support vector regression (SVR) (Smola & Schölkopf, 2004) to create a surrogate model of the relationship between printing parameters and mechanical properties of the parts.

This paper studies the influence of the input process parameters on the mechanical properties of parts manufactured with a Voxeljet VX500, sand-based Binder Jetting 3D Printer (BJ3DP). We identify four input parameters that influence the mechanical properties, i.e. print speed, droplet mass, voxel resolution, and activator percentage (for given curing temperature and time). The quantities of interest (QoIs) are the compressive strength, flexural strength, and Young's modulus of the printed material along the three loading directions. To assess the effect that each input parameter has on the quantity of interest a surrogate model was developed using sparse polynomial chaos expansion (PCE) (Blatman & Sudret, 2011; Lüthen et al., 2022) and the first-order and total Sobol' indices are computed directly from the coefficients of the PCE (Sudret, 2008).

3.2 Binder jetting 3D printer

The principal application of BJ3DP is in the foundry industry to create intricate molds that would be impractical to build with traditional manufacturing techniques (Upadhyay et al., 2017). BJ3DP is also used in the research, to build physical models of rocks (Jiang & Zhao, 2015; Tian & Han, 2017) and masonry structures (DeJong & Vibert, 2012; Ritter, 2017).

3.2.1 Printing process

The 3D printer used to manufacture the specimens of this study is a Voxeljet VX500. It has a building space of 500×400×300 mm (length × width × height). BJ3DP is similar to other powder-based processes, as it uses an inkjet Printer Head (PH) to spray the binder onto the job box (build platform). In a nutshell, the printing process consists of two alternating steps: a) the deposition of a thin layer of powder on the build platform using a recoater; b) the precise application of binder from the printer head in selected location defined in the CAD model (Fig. 1 and Fig. 2).

The sand is stored in the sand container located on top of the machine (Figure 2) which is filled manually before the print job is started. The sand is transported from the external container to an automatic refilling station via a screw conveyor. The recoater is then refilled automatically every three deposited layers at the refilling station.

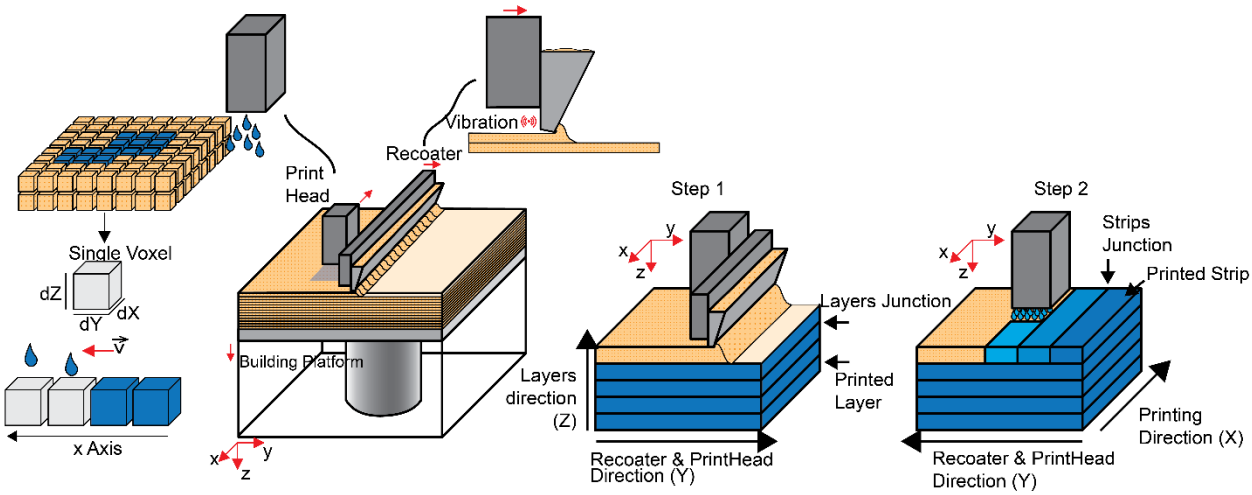

Figure 1. Schematic of the BJ3DP process.

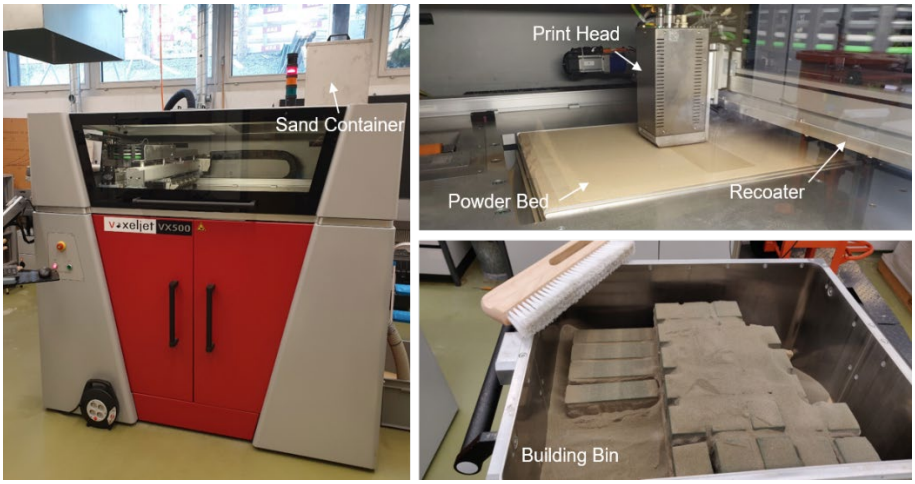

Figure 2. Voxeljet VX500 binder jet 3D printer.

The sand is delivered on the build platform by the recoater, which deposits a 300 µm thick layer using a vibrating blade at a constant recoating speed of 500 mm·s^{-1}. The vibration of the blade is generated by a vibration motor set to 5400 rpm and it regulates the powder outflow, which is essential to have an evenly distributed and compacted powder bed (Zhao et al., 2019).

After the powder bed is deposited, the printer head (PH) selectively sprays the binder through the 768 piezo-ceramic nozzles equally distributed across the six printing modules at the bottom of the PH. The piezo-ceramic outlets are activated with an electrical pulse with voltage that can be modified by the user. The pulse causes the piezo-ceramic elements to deform, which in turn produce a single droplet of binder per nozzle. The correlation between pulse voltage and droplet mass is linear as shown in Figure 3. The pulse voltage can vary from 85.5 to 98 V (according to the manufacturer). In this range, the resulting droplet mass ranges from 104 to 116 ng.

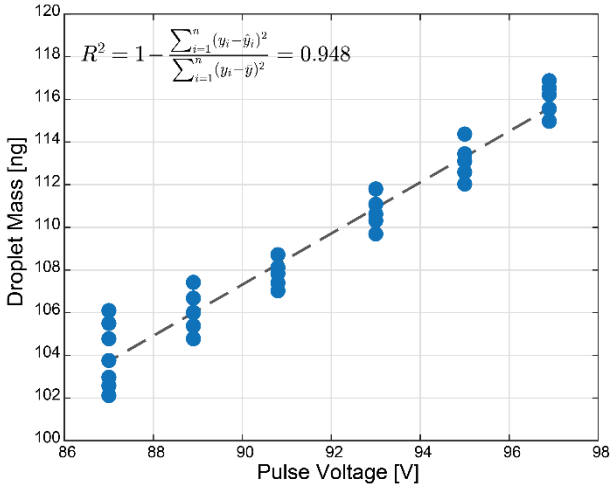

Figure 3. Pulse voltage vs droplet mass correlation.

One droplet is intended to bind only the sand included in one voxel, which constitutes the basic unit of a three-dimensional grid. The voxel size is defined by three dimensions called dX, dY, and dZ, which refer to the resolution in X, Y, and Z direction, respectively. The resolution in Z direction is fixed and it is equal to the layer thickness (300μm). The resolution in Y direction is fixed at 85μm, whereas the resolution in X can range from 80μm to 150μm. The speed of the print head along the X direction (see Figure 1) can be set between 0.30 and 0.50m/s,

3.2.2 3D printed material

The printed material comprises sand and binder. The sand is a quartz-sand type GS19 with a medium grain size of 190 μm. The binder agent is a furan resin largely composed of furfuryl alcohol whose polymerization is facilitated by a p-toluenesulfonic acid (activator) (McKillip, 1989; Principe et al., 2000; Schmitt, 1974) premixed in the sand. More specifically the furan resin solution is made of Furfuryl Alcohol (70–90%), 4,4'-Isopropylidendiphenol (10–20%),

1, 3-Benzenediol (2.3–3%), and 3-Aminopropyltriethoxysilane (0.1–1%). The precise composition of the solution is not provided by the manufacturer. The acid activator consists of a mixture of Xylensulphonic acid (46–50%), Toluenesulphonic acid (20–25%), and Sulphuric acid (<2.5%). The printer manufacturer recommends an activator-to-sand mass ratio between 0.3% and 0.33%. Specifically, multiple batches of 80 kg of sand were prepared adding 0.3-033% of the sand weight of activator and mixing for 45 min at 26.5 rpm.

3.2.3 Orthotropy of the material

The 3D printing process produces a material that is orthotropic by construction as shown in (Feng et al., 2015; Del Giudice & Vassiliou, 2020). Therefore, the compressive strength and the Young's modulus must be tested along three directions, X, Y, and Z (Figure 1 and Figure 4, left). For the flexural strength, two directions must be defined; a) the direction of the longitudinal axis of the specimen and b) the loading direction along which the load of the 4 point bending is applied. Figure 4 (right) shows the orientation of the specimens within the printing space.

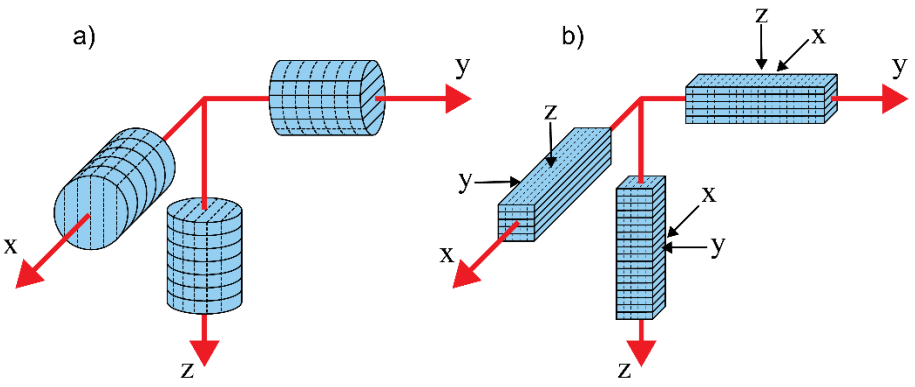

Figure 4. Loading directions: (a) compression test, (b) bending test.

3.3 Global sensitivity analysis framework

Global sensitivity analysis (GSA) aims at quantifying the effect of the input variables on the response quantities of interest of the BJ3DP material. In particular, we perform an analysis of variance (ANOVA) by calculating a set of Sobol' indices (Saltelli et al., 2008; Sobol, 1993) for each response quantity. The application of this methodology can be divided in four steps. First, the response quantities of interest must be identified and the input/process parameters that affect them are selected. Second, the values of the input parameters that will be used to print the samples are defined using latin-hypercube-sampling (LHS) (McKay, 1992). Third, the specimens are printed according to the experimental design defined in the second step and

the tests necessary to obtain the desired QoI are carried out. Each print job includes three cylinders to be tested in compression (along the different loading directions) and six bars to be tested in bending (along the different combinations of the directions of the longitudinal axis of the specimen and the loading axis). Finally, a surrogate model using PCE is constructed from the measurements, and the Sobol' indices are obtained as a by-product of the PCE coefficients (Sudret, 2008).

3.3.1 Input / Output identification

The relevant input parameters, to be included in the experimental design, depend on the quantity of interest (QoI) considered. In this study the QoIs are the mechanical properties of the printed material, i.e. compressive strength, Young's modulus, and flexural strength, along different loading directions. These outputs are quantified experimentally through uniaxial compression tests on cylindrical samples with 50 mm diameter and 100 mm height and four-point bending tests on samples with dimensions of 30x30x120 mm. The choice of the relevant input parameters starts with the understanding of the 3D printing process and the identification of the factors that are expected to have an impact on the strength of the material. As the material strength is expected to depend on the strength of the matrix of polymers (binder), the mechanical properties should depend on the volumetric binder ratio. Therefore, the first two input parameters that are included in the study are the voxel resolution (dX) and the droplet mass, as they both influence the volumetric binder ratio. The third selected input parameter is the activator ratio which affects the kinematics of the polymerization process. The fourth and last input parameter investigated in the study is the printing speed, which can have an effect on the curing process of subsequent strips of deposited binder, hence potentially affecting the overall strength of the sample. Table 1 shows the four input parameters selected in this study and their ranges.

Parameters	min	max
Activator (%)	0.30	0.33
dX Resolution (μm)	80.00	150.00
Print Speed (mm/s)	0.30	0.50
Droplet Mass (ng)	105.00	115.00

Table 1. Input parameters and ranges.

3.3.2 Influence on curing time and temperature

Apart from the 4 printing parameters, the mechanical properties of the printed material depend on the post-printing curing. Freshly printed samples are of low mechanical strength (Del Giudice & Vassiliou, 2020). However, with time, the polymerization reaction of the furfuryl

alcohol increases the strength of the printed material. Previous studies on the curing of such material have shown that heat accelerates the strength build up and yields a stronger material compared to curing at low temperature for an extended period of time (Del Giudice & Vassiliou, 2020; Primkulov et al., 2017). Therefore, before performing the sensitivity analysis on the printing process parameters, the influence of different curing times and temperatures was be assessed. To this end, a series of uniaxial compression tests was performed. A total of 35 cylindrical samples with diameter 50mm and height of 100mm were tested along the Z direction (direction defined in Figure 1). The samples were cured at temperatures of 80°C and 115°C for 30, 60, 120 minutes, respectively. Five samples from each temperature – curing time combination were tested. In addition, five control samples that did not undergo heat treatment were tested. The control samples were cured in a climate-controlled chamber at 22°C and 55% relative humidity for 40 days. Figure 5 shows the box plots of the compressive strength for each treatment strategy. Clearly, the various treatment strategies increase the compressive strength compared to the control specimens. Among the different treatments, the differences are smaller. The treatment at 80 °C seems to result in smaller variability than the one at 115 ºC. When treated at 80 ºC, different durations of treatment resulted in similar results, as also observed by Primkulov et al. (Primkulov et al., 2017). Therefore, it was decided to cure all the samples used in the subsequent sensitivity analysis at 80°C for 30 minutes.

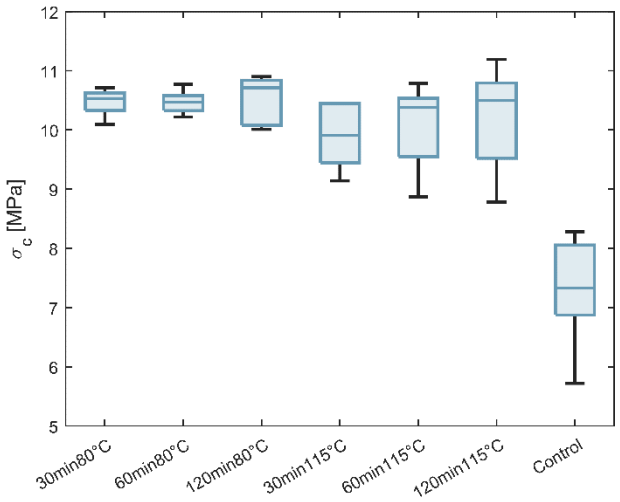

Figure 5. Compressive strength of 3D printed material after thermal cure. The box plot shows the compressive strength of the material treated at 80°C and 115°C for 30, 60, and 120 minutes, as well as the control specimen.

3.3.3 Experimental Design

Once the input parameters and their ranges were identified (Table 1), the experimental design, i.e. the combinations of input parameters values used to print the samples for the mechanical

tests, was defined using Latin Hypercube Sampling (LHS). Each data point of the experimental design corresponds to a print job with three compression samples and six bending samples, for a total of nine tests. To minimize the experimental cost of the study a sequential quasi-LHS sampling strategy (Wang, 2003) was used. This method sequentially generates sample points while preserving the properties of LHS, e.g. space-filling. Unlike the standard LHS, a series of small subsets of six sample points are generated such that each subset remains approximately LHS and the union of all subsets is still an LHS. This methodology has the advantage of not defining a priori the experimental design (ED) size but allowing to proceed step-by-step and to enrich the ED, if necessary. Three subsets of six data points were used for a total of 18 different print jobs. The experimental design is shown in Figure 6. The diagonal plots show the histogram of the values of each parameter. The off-diagonal plots show the values of the parameters for each of the 18 print jobs. The values of the input parameters are reported in Table 2.

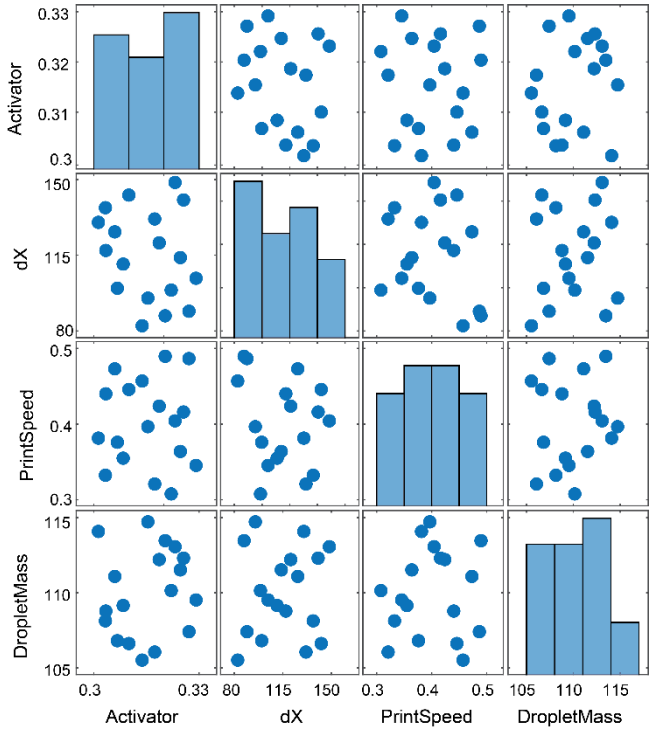

Figure 6. Experimental design using optimized LHS.

3.3.4 Sample preparation and testing

The preparation of the print jobs started with the preparation of the sand necessary for the printing process. 80kg of sand was used for each print job and it was mixed for 45 min with the activator according to the experimental design as reported in Table 2. Then the pulse voltage was adjusted to yield droplets of mass equal to the one specified in the experimental design.

The voxel resolution and the print speed were adjusted directly by the printer software. Finally the specimens were printed and cured at 80°C for 30min, as discussed in Section 2.2. The process was repeated for all 18 combinations of process parameter values.

Subset LHS	Data Point	Activator %	dX µm	Print Speed mm/s	Droplet Mass ng
1	1	0.323	148.64	0.480	112.64
	2	0.314	82.39	0.456	105.05
	3	0.315	95.14	0.396	114.92
	4	0.306	125.79	0.473	111.13
	5	0.303	136.97	0.332	108.59
	6	0.329	104.34	0.345	109.65
2	7	0.301	130.19	0.381	113.96
	8	0.319	120.71	0.423	111.72
	9	0.322	98.87	0.307	110.43
	10	0.308	110.90	0.354	109.15
	11	0.327	89.09	0.486	107.40
	12	0.312	142.78	0.445	106.03
3	13	0.303	117.19	0.440	109.00
	14	0.325	140.56	0.416	112.20
	15	0.307	99.72	0.375	106.72
	16	0.325	113.90	0.363	111.95
	17	0.320	87.00	0.489	113.74
	18	0.318	131.75	0.320	106.26

Table 2. Input parameters for selected input variables

The cylindrical samples were tested in uniaxial compression to assess the Young's modulus and compressive strength according to the SIA 262-Annex G Standard (SIA 262/1:2013, 2013). The strains were measured using an axial extensometer, which measures strains on opposite sides of the samples independently (Figure 7).

Four-point bending tests were performed on the prismatic samples to determine the flexural strength of the material. The setup shown in Figure 7 consisted of two supports with a span of 110 mm and two loading pins with a span of 40 mm. The distance between the bottom supports and the loading pins was 30 mm. The samples were loaded in displacement control at a constant rate of 0.5 mm/min until failure.

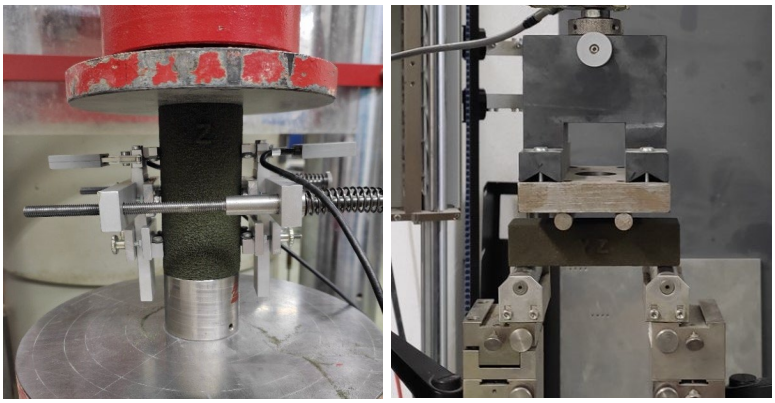

Figure 7. Left, Uniaxial compression tests and axial extensometer. Right, Four point bending test.

3.3.5 Polynomial chaos expansion and global sensitivity analysis

To quantify the fraction of variability of the QoI that is due to the variability of the input parameters, Sobol' sensitivity indices were used (Saltelli et al., 2008; Sobol, 1993). This method belongs to the class of variance-decomposition-based sensitivity analysis, which rely on the decomposition of the variance of a QoI as a sum of terms representing the contribution of each input variable, or combinations thereof. Unlike regression-based methods, e.g., Pearson's or Spearman's correlation coefficients, variance-based methods do not rely on linearity or monotonicity of the relationship between input and QoI (Gibbons & Chakraborti, 2014).

Historically, the computation of Sobol' indices has been based on Monte Carlo-based estimation. However, the number of samples required is large ($O(10^3)$ per input variable) and in case of experimentally expensive processes (as is the case for the mechanical characterization of 3D printed material), it is practically not feasible. An alternative way to compute Sobol' indices is to post-process the coefficients of a polynomial chaos expansion (PCE) of the QoIs (Sudret, 2008).

3.3.6 Sobol'-Hoeffding decomposition and sensitivity analysis

Let $\mathbf{X} = \{X_1,...,X_M\}$ denote an *M*-dimensional vector of input properties and *Y* denote the generic realization of the QoI, considering the 3D printing process as a black-box. Assume that the vector of input variables has support $\mathcal{D}_{\mathbf{X}}$ and an independent joint probability density function $f_{\mathbf{X}}(\boldsymbol{x}) = \prod_i^M f_{X_i}(x_i)$, where f_{X_i} is the marginal PDF of the *i-th* input parameter. Sobol' (1993) asserts that any square-integrable mapping $Y = \mathcal{M}(\mathbf{X})$ with respect to the probability measure associated with the joint PDF can be expanded as the sum of functions of increasing dimensionality (Sobol, 1993):

$$\mathcal{M}(\mathbf{X}) = \mathcal{M}_0 + \sum_{i=1}^{M} \mathcal{M}_i(X_i) + \sum_{1 \le i \le j \le M} \mathcal{M}_{i,j}(X_i, X_j) + ... + \mathcal{M}_{1,2,...M}(\mathbf{X}) \tag{1}$$

or equivalently:

$$\mathcal{M}(\mathbf{X}) = \mathcal{M}_0 + \sum_{\substack{\mathbf{u}\subset\{1,\ldots,M\} \\ \mathbf{u}\neq\emptyset}}^{M} \mathcal{M}_{\mathbf{u}}(\mathbf{X}_{\mathbf{u}}) \tag{2}$$

where $\mathcal{M}_0$ is constant and represents the mean value of *Y*, while $\mathbf{X_u}$ is a sub-vector of $\mathbf{X}$ containing the elements indexed by the subset $\mathbf{u} \subset \{1,\ldots,M\}$. The number of summands in Equation (1) is $2^M - 1$. The Sobol' decomposition is unique when the following holds:

$$\mathbb{E}[M_{\mathbf{u}}(\mathbf{X}_{\mathbf{u}})] = \int_{\mathcal{D}_{\mathcal{X}}} \mathcal{M}_{\mathbf{u}}(\mathbf{X}_{\mathbf{u}}) f_{X_k}(X_k) dx_k = 0, \text{ if } k \in \mathbf{u} \tag{3}$$

where $\mathcal{D}_{\mathcal{X}}$ and f_{X_k} represent the support and the marginal PDF of X_k, respectively. In this setting, orthogonality of the summands also holds:

$$\mathbb{E}[M_{\mathbf{u}}(\mathbf{X}_{\mathbf{u}}) \cdot M_{\mathbf{v}}(\mathbf{X}_{\mathbf{v}})] = 0, \text{ if } \mathbf{u} \neq \mathbf{v} \tag{4}$$

Given Equations (3) and (4), the total variance of $\mathcal{M}(\mathbf{X})$ can be decomposed as

$$D = \mathrm{Var}[\mathcal{M}(\mathbf{X})] = \sum_{\substack{\mathbf{u}\subset\{1,\ldots,M\} \\ \mathbf{u}\neq\emptyset}} D_{\mathbf{u}} \tag{5}$$

where

$$D_{\mathbf{u}} = \mathrm{Var}[\mathcal{M}_{\boldsymbol{u}}(\mathbf{X}_u)] = \mathbb{E}[\mathcal{M}_{\boldsymbol{u}}^2(\mathbf{X}_u)] \tag{6}$$

corresponds to the partial variance of the index set **u**. The associated Sobol' index $S_{\boldsymbol{u}}$ is defined as the ratio between the partial variance and the total variance of the $\boldsymbol{u}$-indexed set of input variables:

$$S_{\mathbf{u}} = \frac{D_{\mathbf{u}}}{D} \tag{7}$$

The influence of each parameter X_i, when considered separately, is given by the first-order indices $S_i^{(1)} = D_i / D$. Second-order indices $S_{ij}^{(2)}$ describe the influence of pairs of input parameters $\{X_i, X_j\}$ which are not already accounted in S_i and S_j, respectively. Total Sobol' indices S_i^{tot} represent the total effect of an input variable X_i, including its first-order effect and all interactions with other input variables.

3.3.7 Sobol' indices from polynomial chaos expansion

PCE is a well-known surrogate modelling technique, namely a spectral decomposition method that projects the model response onto a functional basis of orthonormal multivariate polynomial

in the input variables (Berveiller et al., 2006; Xiu & Karniadakis, 2002). Such method is used to substitute an expensive model or, in the case of this paper, an expensive experimental process with an inexpensive surrogate, representing the outputs of the process with a polynomial function of its inputs. PCE is particularly suitable in studies with a limited number of data points for its proven robustness to noise (Torre et al., 2019). The decomposition of the model response of QoI $Y = \mathcal{M}(\mathbf{X})$ is then a linear superposition of nonlinear functions:

$$\hat{Y} = \mathcal{M}^{\mathrm{PCE}}(\mathbf{X}) = \sum_{\boldsymbol{\alpha}\in\mathcal{A}} \mathcal{Y}_{\boldsymbol{\alpha}} \Psi_{\boldsymbol{\alpha}}(\mathbf{X}) \tag{8}$$

where $\{\Psi_{\boldsymbol{\alpha}}, \boldsymbol{\alpha} \in \mathcal{A}\}$ is a set of multivariate orthonormal polynomial basis with respect to the input vector with independent component $\mathbf{X} \sim f_{\mathbf{X}}(\mathbf{x}) = \prod_i^M f_{\mathbf{X}_i}(\mathbf{x}_i)$, $\boldsymbol{\alpha} = (\alpha_1, ..., \alpha_M) \in \mathbb{N}^N$ is a multi-index that defines the polynomial degree of the input variables, and $\mathcal{Y}_{\boldsymbol{\alpha}}$ corresponds to the polynomial coefficients. The infinite sum in Equation (8) needs to be truncated to a finite series. This can be achieved with different methods, i.e. maximum-degree, maximum-interaction or hyperbolic norm truncation (Blatman & Sudret, 2011). The set of coefficients of the PCE is calculated by minimizing the expected mean-square approximation by solving:

$$\widehat{\mathcal{Y}}_{\boldsymbol{\alpha}} = \arg\min_{\mathcal{Y}_{\boldsymbol{\alpha}}} \mathbb{E}[(Y - \hat{Y})] \tag{9}$$

To minimize the associate experimental design in high dimensional or highly nonlinear models, sparse and basis-adaptive regression techniques have been developed in the recent literature (Lüthen et al., 2021; Lüthen et al., 2022).

The condition of orthonormality of the PCE basis allows one to compute the mean and variance of $\mathcal{M}^{PCE}(\mathbf{X})$ analytically from the $\mathcal{Y}$ coefficients at no extra cost as follows:

$$\hat{\mu} = \mathbb{E}[\mathcal{M}^{\mathrm{PCE}}(\mathbf{X})] = \mathbb{E}\left[\sum_{\boldsymbol{\alpha}\in\mathcal{A}} \mathcal{Y}_{\boldsymbol{\alpha}} \Psi_{\boldsymbol{\alpha}}(\mathbf{X})\right] = \mathcal{Y}_0 \tag{10}$$

$$\hat{\sigma}^2 = \mathrm{Var}\left[\left(\mathcal{M}^{\mathrm{PCE}}(\mathbf{X}) - \mathcal{Y}_0\right)^2\right] = \sum_{\boldsymbol{\alpha}\in\mathcal{A}} \mathcal{Y}_{\boldsymbol{\alpha}}^2 \tag{11}$$

Equations (10) and (11) hold because $\Psi_0 \equiv 1$. Therefore, when the PCE of *Y* is already constructed, the Sobol'-Hoeffding decomposition of Equation (2) can be rewritten as

$$\mathcal{M}^{\mathrm{PCE}}(\mathbf{X}) = \mathcal{M}_0^{\mathrm{PCE}} + \sum_{\substack{\mathbf{u}\subset\{1,...,M\} \\ \mathbf{u}\neq\varnothing}}^{M} \mathcal{M}_u^{\mathrm{PCE}}(\mathbf{X}_{\mathbf{u}}) \tag{12}$$

and the summands $\mathcal{M}_u^{PCE}(\mathbf{X_u})$ in (12) can be written as

$$\mathcal{M}_{\mathbf{u}}^{\mathrm{PCE}}(\mathbf{X_u}) = \sum_{\boldsymbol{\alpha}\in\mathcal{A}_{\mathbf{u}}} \mathcal{Y}_{\boldsymbol{\alpha}} \Psi_{\boldsymbol{\alpha}}(\mathbf{X_u}) \tag{13}$$

Where $\mathcal{A}_{\mathbf{u}} = \{\boldsymbol{\alpha} \in \mathcal{A} : \alpha_m \neq 0 \text{ if and only if } m \in \mathbf{u}\}$ represents the set of multi-indices that depend only on $\boldsymbol{u}$. According to Equations (12) and (13), the total and partial variances of $\mathcal{M}^{PCE}(\mathbf{X})$ is given by

$$\begin{aligned} D &= \mathrm{Var}\left[\mathcal{M}^{\mathrm{PCE}}(\mathbf{X})\right] = \sum_{\boldsymbol{\alpha}\in\mathcal{A}} \mathcal{Y}_{\boldsymbol{\alpha}}^2 \\ D_{\boldsymbol{u}} &= \mathrm{Var}\left[\mathcal{M}_{\mathbf{u}}^{\mathrm{PCE}}(\mathbf{X})\right] = \sum_{\boldsymbol{\alpha}\in\mathcal{A}_{\mathbf{u}}} \mathcal{Y}_{\boldsymbol{\alpha}}^2 \end{aligned} \tag{14}$$

Consequently, the first-order and total Sobol' indices are obtained from

$$\begin{aligned} S_i^{(1)} &= \frac{\sum_{\boldsymbol{\alpha}\in\mathcal{A}_i} \mathcal{Y}_{\boldsymbol{\alpha}}^2}{\sum_{\boldsymbol{\alpha}\in\mathcal{A}} \mathcal{Y}_{\boldsymbol{\alpha}}^2}, \qquad \mathcal{A}_i = \left\{\boldsymbol{\alpha} \in \mathcal{A} : \alpha_i > 0, \alpha_{i\neq j} = 0\right\} \\ S_i^{\mathrm{tot}} &= \frac{\sum_{\boldsymbol{\alpha}\in\mathcal{A}_i^{\mathrm{tot}}} \mathcal{Y}_{\boldsymbol{\alpha}}^2}{\sum_{\boldsymbol{\alpha}\in\mathcal{A}} \mathcal{Y}_{\boldsymbol{\alpha}}^2}, \qquad \mathcal{A}_i = \left\{\boldsymbol{\alpha} \in \mathcal{A} : \alpha_i > 0\right\} \end{aligned} \tag{15}$$

Therefore, Sobol' indices can be obtained directly as a by-product of the PCE without any additional cost [24]. Sobol' indices provide a quantitative insight on the importance of any input parameter. However, they do not include information about the direction in which the input parameters affect the outcomes, or whether the relationship of the each input parameter to the QoI is linear or nonlinear. To gain further insight on the effect of the input parameters on the QoIs, univariate effects are computed (Abbiati et al., 2020; Deman et al., 2016; Harenberg et al., 2019). Univariate effects can be defined as the conditional expectation of a quantity of interest as a function of a single parameter, where expectations are taken over all other parameters:

$$\mathcal{M}_i^{(1)}(\theta_i) = \mathbb{E}\left[\mathcal{M}(\boldsymbol{\Theta} \mid \Theta_i = \theta_i\right] \tag{16}$$

They can be interpreted as an average or as a robust relationship between one input parameter and the quantity of interest (Harenberg et al., 2019). In the case of PCE models, univariate effects have a closed analytical form, which is closely related to the first-order Sobol' decomposition:

$$\mathcal{M}_i^{(1)}(X_i) = \sum_{\boldsymbol{\alpha}\in\mathcal{A}_i} \mathcal{Y}_{\boldsymbol{\alpha}} \Psi_{\boldsymbol{\alpha}}(X_i), \quad \mathcal{A}_i = \left\{\boldsymbol{\alpha} \in \mathcal{A} : \alpha_i > 0, \quad \alpha_{i\neq j} = 0\right\} \tag{17}$$

In this paper, the computation of PCE, Sobol' indices, and univariate effects are performed using UQLab, which is a MATLAB toolbox developed by the Chair of Risk, Safety and Uncertainty Quantification of ETH Zurich (Marelli & Sudret, 2014).

3.4 Results and discussion

This section reports the results of the mechanical tests as described in Section 3.3, the global sensitivity analysis procedure through the construction of a PCE surrogate model of the QoI, and the calculation of Sobol' indices from the coefficients of PCE as described in Section 3.4.2.

The uniaxial compression tests and the four-point bending tests produced a total of 12 outputs for each input parameter value combination. These are the Young's modulus along X, Y, and Z (Ex, Ey, Ez), the uniaxial compressive strength along X, Y, and Z (σ^{C}_{x}, σ^{C}_{y}, σ^{C}_{z}), and the flexural/bending strength along XY, XZ, YX, YZ, ZX, ZY (σ^{B}_{xy}, σ^{B}_{xz}, σ^{B}_{yx}, σ^{B}_{yz}, σ^{B}_{zx}, σ^{B}_{zy}). Two letters are used to define the name of the bending strength. The first letter indicates the direction of the centerline of the sample whereas the second letter refers to the loading direction.

Data Point	Ex	Ey	Ez	σ^{B}_{xy}	σ^{B}_{xz}	σ^{B}_{yx}	σ^{B}_{yz}	σ^{B}_{zx}	σ^{B}_{zy}	σ^{C}_{x}	σ^{C}_{y}	σ^{C}_{z}
	GPa	GPa	GPa	MPa	MPa	MPa	MPa	MPa	MPa	MPa	MPa	MPa
1	3.89	3.76	3.88	2.91	2.16	3.03	2.07	2.85	3.05	8.30	6.70	8.80
2	5.28	5.34	5.08	4.45	3.81	4.29	3.52	5.00	4.79	12.60	11.00	14.40
3	4.96	4.80	4.71	4.01	3.19	4.11	3.00	4.24	4.37	11.10	9.60	12.10
4	4.36	4.72	3.60	2.82	2.63	3.16	2.20	2.76	3.07	9.40	7.30	9.40
5	3.83	3.87	3.62	2.34	2.07	2.29	1.85	1.95	2.13	8.00	6.20	7.80
6	4.62	4.61	4.38	3.64	2.88	3.73	2.86	3.48	3.65	11.60	9.70	11.70
7	4.41	4.14	4.06	3.04	2.48	3.02	2.52	3.02	3.05	9.90	8.30	10.30
8	4.74	5.08	4.75	3.58	3.43	3.92	3.08	4.13	4.23	11.90	11.00	12.10
9	5.32	5.09	4.79	4.07	3.87	4.37	3.95	4.84	4.70	13.60	12.50	13.10
10	4.99	5.25	4.56	3.80	2.89	3.90	3.07	4.13	3.87	12.70	11.00	12.40
11	6.08	5.74	5.18	4.30	3.90	4.63	3.47	5.30	5.40	14.90	13.30	14.70
12	4.13	4.17	3.59	2.85	2.40	2.85	2.21	2.63	2.95	8.10	6.50	8.40
13	4.44	4.52	4.10	3.93	3.26	3.77	3.08	4.43	4.00	11.50	10.30	11.50
14	4.40	4.48	4.05	3.20	2.82	3.21	2.38	3.16	3.70	10.10	9.50	10.20
15	4.89	5.14	4.57	4.03	3.47	3.90	3.07	4.97	5.10	13.20	11.80	12.80
16	5.07	4.66	4.49	4.03	3.43	4.00	3.27	4.30	4.17	12.00	11.40	12.20
17	5.42	5.61	4.72	4.10	3.90	4.00	3.80	5.30	5.63	15.30	14.30	15.70
18	4.59	4.65	4.32	3.37	3.29	3.28	3.11	3.43	3.57	10.50	9.80	11.00

Table 3. Young's modulus in X, Y, and Z direction (Ex, Ey, Ez). Flexural strength in XY, XZ, YX, YZ, ZX, and ZY direction (σ^{B}_{xy}, σ^{B}_{xz}, σ^{B}_{yx}, σ^{B}_{yz}, σ^{B}_{zx}, σ^{B}_{zy}). Uniaxial compressive strength in X, Y, and Z direction (σ^{C}_{x}, σ^{C}_{y}, σ^{C}_{z}).

The results are reported in Table 3 for all input process parameters and they are shown in Figure 8 as scatter plots. The plots show a clear trend of all QoI in relation to the voxel resolution

(dX). All output parameters tend to decrease almost linearly with increasing dX regardless of the value of the other input parameters. Figure 8 does not show any clear correlation between mechanical properties and activator percentage, print speed, and droplet mass. The correlation between inputs and outputs is quantified with Pearson's correlation coefficients and reported in Table 4.

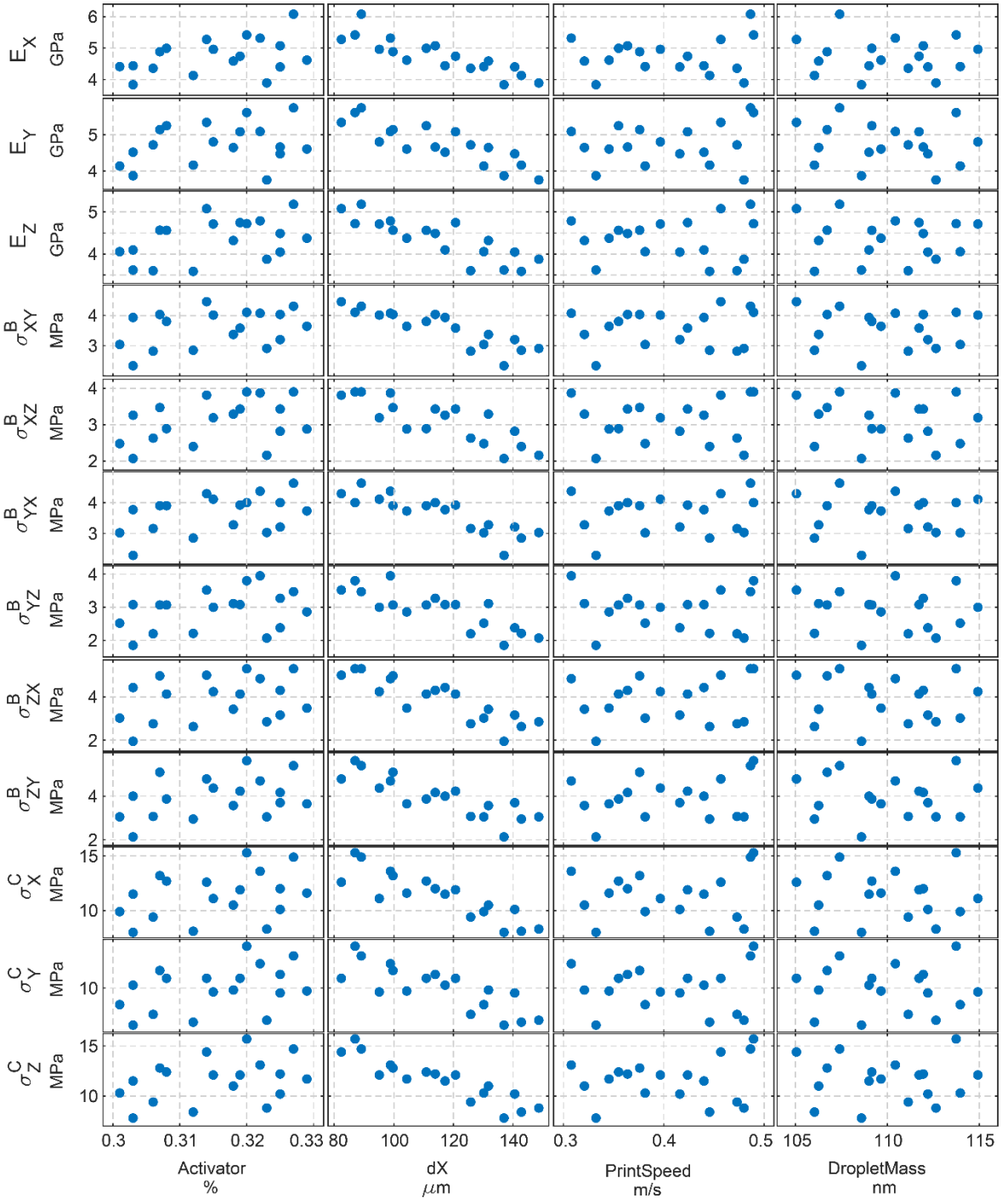

Figure 8. Scatter plots of the QoI against the process input parameters.

3.4.1 Surrogate model using PCE

The experimental design defined in Section 3.2, and the results of the mechanical tests shown in Section 4, are used to train the PCEs of the QoI. The PCEs were constructed using the Matlab based software UQLab (Marelli & Sudret, 2014). The model was trained with all 18 data points of the ED, due to the small sample size. The coefficients of the PCE were computed using Least Angle Regression (LARS) (Efron et al., 2004). The equations of the PCEs are shown explicitly in the Appendix and can be used to calculate the predicted values of the mechanical properties analytically. Figure 9 shows the leave-out-out cross validation error of the trained PCEs. Leave-one-out cross validation (Blatman & Sudret, 2011) involves training the meta-model on n-1 points and using the remaining point for validation (where n is the size of the experimental design). Therefore, each on the 18 points in each subplot of Figure 9, represents the prediction vs the experimental value of point i (i=1-18) when the model is trained in the remaining 17 points.

	Ex	Ey	Ez	σ^{B}_{xy}	σ^{B}_{xz}	σ^{B}_{yx}	σ^{B}_{yz}	σ^{B}_{zx}	σ^{B}_{zy}	σ^{C}_{x}	σ^{C}_{y}	σ^{C}_{z}
Activator	0.40	0.26	0.43	0.34	0.37	0.42	0.35	0.29	0.38	0.33	0.39	0.35
dX	-0.87	-0.85	-0.85	-0.88	-0.83	-0.87	-0.83	-0.87	-0.85	-0.87	-0.80	-0.91
Print Speed	0.12	0.19	0.02	0.08	0.07	0.11	-0.07	0.16	0.24	0.07	0.04	0.16
Droplet Mass	-0.08	-0.16	-0.08	-0.11	-0.14	-0.03	-0.08	-0.08	-0.03	-0.04	0.00	-0.03

Table 4. Pearson's correlation coefficients between input parameters and the mechanical properties.

3.4.2 Sobol' indices and univariate analysis

Once the surrogates of each QoI are developed, the Sobol' indices are computed at no extra cost, as discussed in Section 3.4.2. Figure 10 shows the first-order and total Sobol' indices for all four input parameters (dX, activator percentage, print speed, and droplet mass). The error bars represent the 95% confidence interval of the sensitivity indices computed with 500 bootstrap replications of the PCEs (Dubreuil et al., 2014).

Figure 11 shows the univariate effect of all input parameters on the predicted value of the compressive strength σ_Z^C. These plots give an insight about the direction in which the input parameters affect the QoI σ_Z^C. The univariate effects are computed from PCEs according to the description in Section 3.4.2. The same figure also reports with dashed lines the 95% confidence interval of the univariate effects, computed with 500 bootstrap replications on the PCEs [51].

As expected, the univariate effect of the dX resolution shows that there is a monotonically decreasing linear relationship with the σ_Z^C. The univariate effects of the print speed and

of the droplet mass are completely flat, meaning that there is no appreciable effect of these input variables on the QoI σ_z^C. The univariate effect of the activator percentage on σ_z^C is nonlinear. However, the Sobol' index is below 0.1 which indicates that the overall effect of the acti-

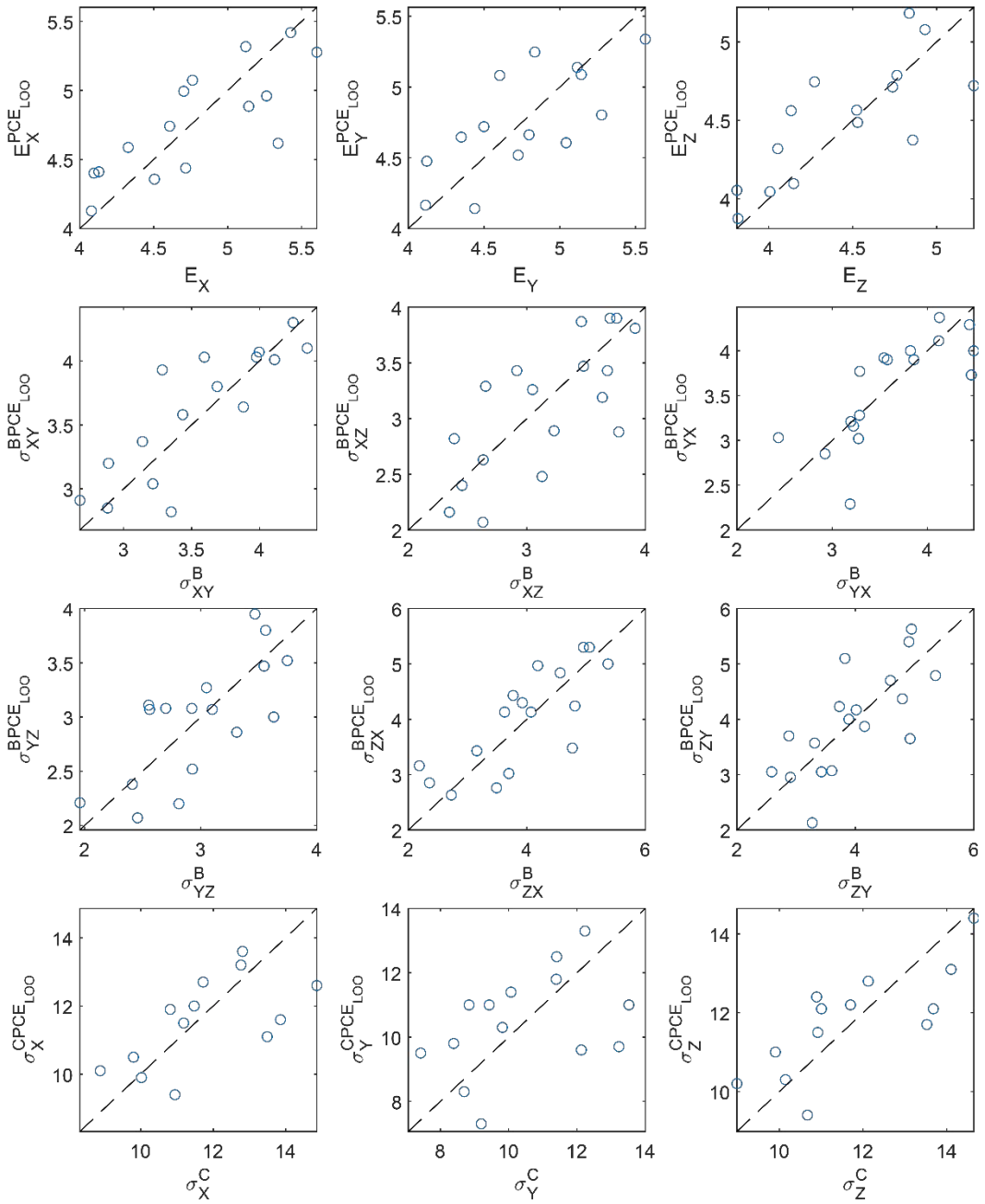

Figure 9. Comparison between QoI and corresponding leave-one-out cross validation PCE estimates.

vator percentage on σ_z^C is marginal. The variability observed in the result indicates that there exists a relatively large uncertainty of the value of the QoI, because of the sample size. However, the scope of this paper is not the prediction of the outputs, but rather the use of PCE to

compute the Sobol' indices. In that sense, the only purpose of the PCE is to provide a method to compute the Sobol' indices.

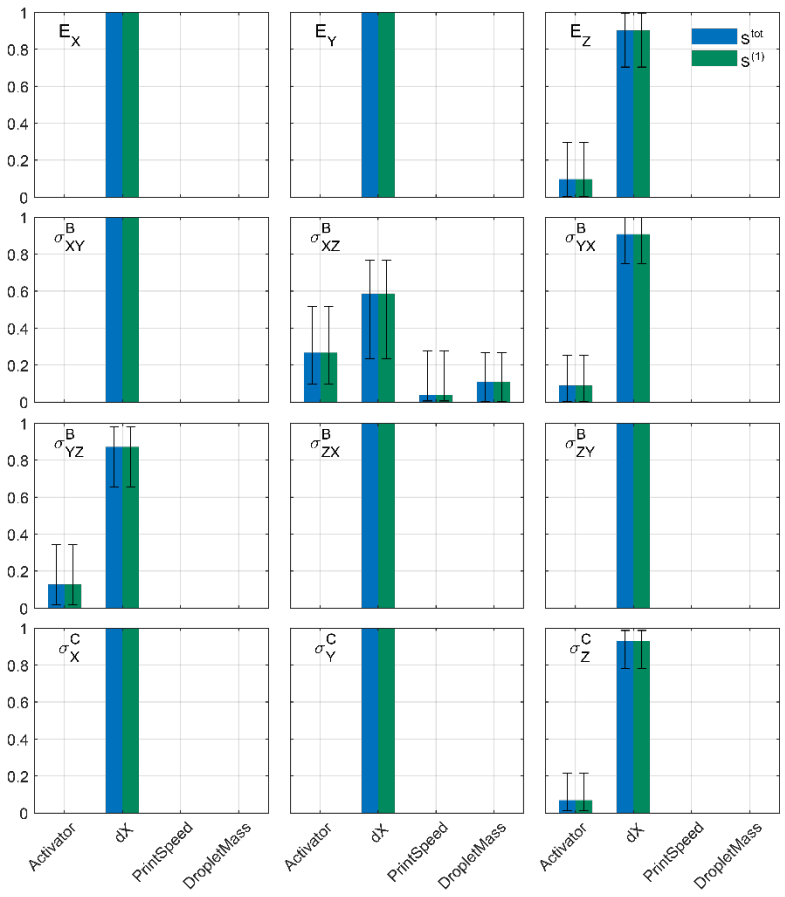

Figure 10. First order and Total Sobol' indices of the QoI.

According to Figure 10, the voxel resolution (dX) is by far the most influential parameters for all QoI. Based on the printing process, one droplet of binder is sprayed in each voxel. Hence, decreasing the voxel's volume, increases the binder weight per printed bulk material volume ratio (w/v) defined as "Binder w/v Content":

$$\text{Binder w/v content} = \frac{\text{BinderMass [ng]}}{\text{BulkMaterialVolume } [\mu\text{m}^3]} \tag{18}$$

Thus, it is reasonable to assume that the Binder w/v content is a physically meaningful parameter that controls the mechanical properties of the printed material. Interestingly, the droplet mass is also an input parameter that controls the Binder w/v content. However, as the range within which it could be varied (due to limitations of the printer) was small, its effects was not captured by the Sobol' index. Figure 12 plots all QoIs as a function of the binder w/v content, as well as linear regressions on the results. It shows that for the range of values of the input

parameters examined, a linear dependence of the QoIs solely on the w/v ratio provides a relatively good approximation of the QoIs (R^2 between 0.61 and 0.82), despite disregarding the dependence on the activator percentage.

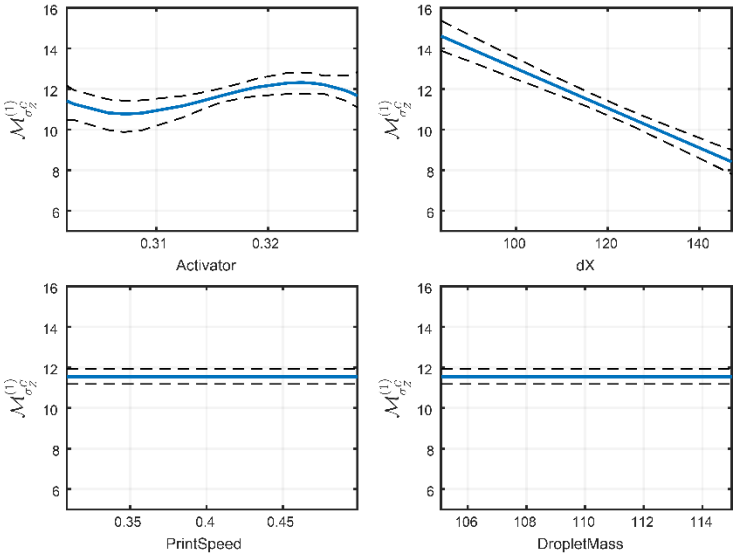

Figure 11. Univariate effect of the input parameters on σ^{C}_{z}.

3.5 Conclusions

This paper systematically studied the dependence of several mechanical properties of a material printed with binder jet technology on the printing process parameters. To reduce the number of the tests needed, a design of experiments approach was applied, and polynomial chaos expansion was used to compute the related Sobol' indices. For the range of the parameters studied, it was found that the compressive and flexural strength, as well as the Young's modulus depend primarily on the binder content of the printed material (therefore on the print resolution and on the binder droplet mass). A lower but not negligible dependence on activator percentage was also found. The printing speed did not significantly affect the mechanical properties of the material. However, the mechanical properties are significantly affected by the post processing of the material: Curing at 80-130 ºC for 30 to 120 min significantly increased its strength.

Appendix

The PCEs described in Section 3.4 and calculated in using UQLab (Marelli & Sudret, 2014) are provided explicitly for each of the 12 QoIs. The functions are expressed as a function of the four input parameters, i.e. droplet mass, print speed, dX resolution, and activator percent-

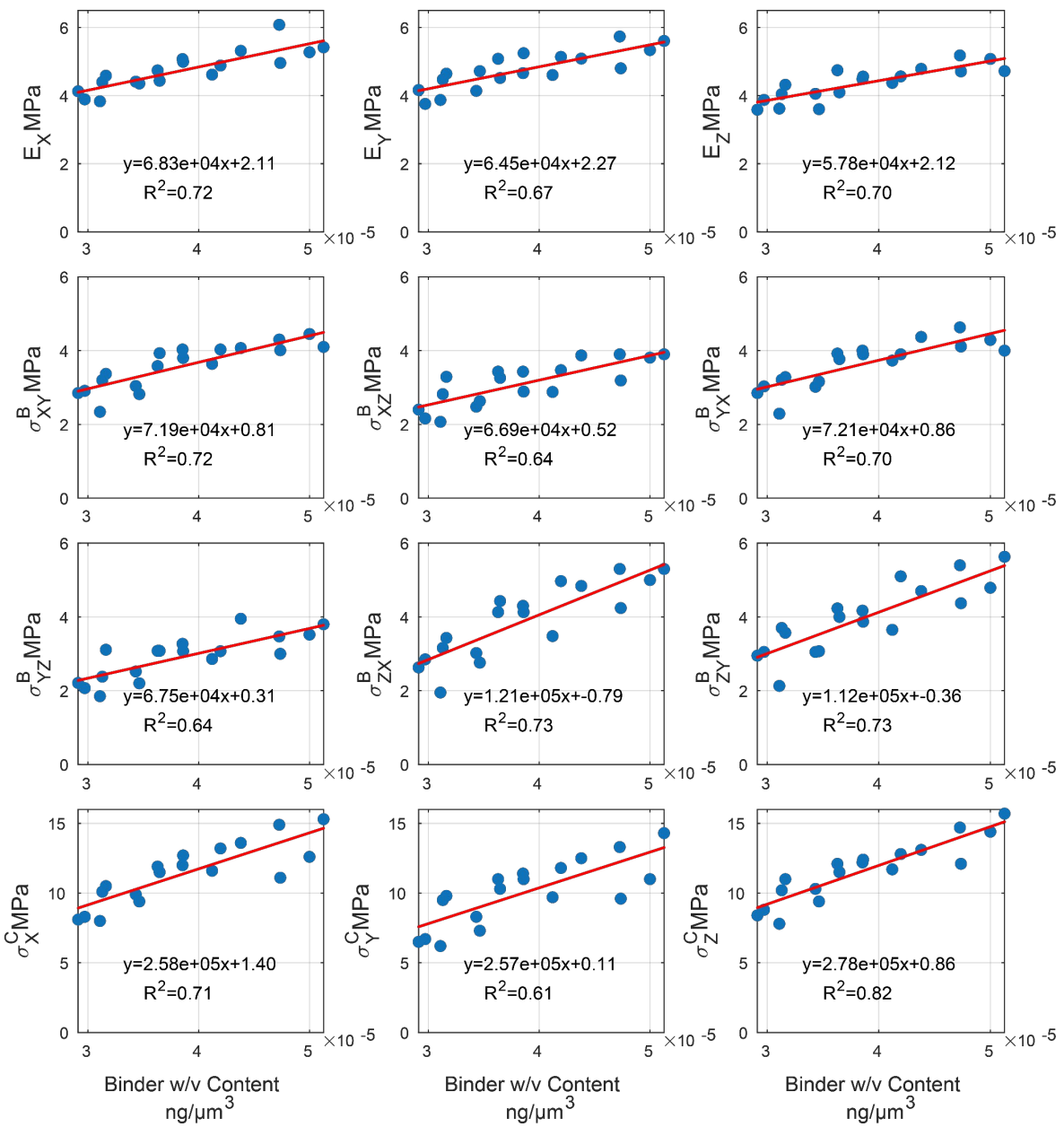

Figure 12. Scatter plots of the QoI against Binder content (w/v).

age. The experimental design was performed assuming a uniform distribution of the input parameters. Orthonormal Legendre polynomials (Sudret, 2008) $\tilde{P}_n(\xi)$ (n represent the degree of the polynomial) were used as a basis for the PCE to respect the property of orthogonality to the uniform input distributions (Table 5). The orthonormal Legendre polynomials are defined over [-1, 1] and the input parameters must be first transformed to standard uniform variables $\mathcal{U} \sim (-1,1)$ as follows

$$\mathrm{X}_i = F_{\mathrm{X}_i}^{-1}\left(\frac{\xi_i + 1}{2}\right) \rightarrow \xi_i = 2F_{\mathrm{X}_i}(\mathrm{X}) - 1 \tag{19}$$

where ξ_i represent the transformed input variables. The index i represent the relative input variable: $i = 1, 2, 3, 4$ correspond to droplet mass, print speed, dX resolution, and activator percentage, respectively. Then the equations of the PCEs are:

$$E_X^{PCE} = 4752.90 - 484.92\tilde{P}_1(\xi_3) \tag{20}$$

$$E_Y^{PCE} = 4763.67 - 467.32\tilde{P}_1(\xi_3) \tag{21}$$

$$E_Z^{PCE} = 4357.19 - 384.255\tilde{P}_1(\xi_3) + 126.56\tilde{P}_1(\xi_4) \tag{22}$$

$$\sigma_{XY}^{B,PCE} = 3.59 - 0.518\tilde{P}_1(\xi_3) \tag{23}$$

$$\begin{aligned}\sigma_{XZ}^{B,PCE} = {} & 3.05 - 0.22\tilde{P}_1(\xi_1) + 0.13\tilde{P}_1(\xi_2) - 0.46\tilde{P}_1(\xi_3) + 0.16\tilde{P}_1(\xi_4) \\ & -0.25\tilde{P}_2(\xi_3) - 0.10\tilde{P}_2(\xi_4) - 0.02\tilde{P}_3(\xi_2) + 0.30\tilde{P}_3(\xi_4)\end{aligned} \tag{24}$$

$$\sigma_{YX}^{B,PCE} = 3.63 - 0.48\tilde{P}_1(\xi_3) + 0.15\tilde{P}_1(\xi_4) \tag{25}$$

$$\sigma_{YZ}^{B,PCE} = 2.89 - 0.53\tilde{P}_1(\xi_3) + 0.20\tilde{P}_3(\xi_4) \tag{26}$$

$$\sigma_{ZX}^{B,PCE} = 3.89 - 0.86\tilde{P}_1(\xi_3) \tag{27}$$

$$\sigma_{ZY}^{B,PCE} = 3.98 + 0.77\tilde{P}_1(\xi_3) \tag{28}$$

$$\sigma_X^{C,PCE} = 11.40 - 1.85\tilde{P}_1(\xi_3) \tag{29}$$

$$\sigma_Y^{C,PCE} = 10.04 - 1.83\tilde{P}_1(\xi_3) \tag{30}$$

$$\sigma_Z^{C,PCE} = 11.54 - 1.97\tilde{P}_1(\xi_3) + 0.29\tilde{P}_1(\xi_4) - 0.45\tilde{P}_3(\xi_4) \tag{31}$$

n	$\tilde{P}_n(\xi)$
0	1
1	$\sqrt{3}\xi$
2	$\sqrt{5}\frac{1}{2}\left(3\xi^2 - 1\right)$
3	$\sqrt{7}\frac{1}{2}\left(5\xi^2 - 3\xi\right)$
4	$\sqrt{9}\frac{1}{8}\left(35\xi^4 - 30\xi^2 + 3\right)$

Table 5. Orthonormal Legendre polynomial of degree $n = 0$ through $n = 4$.

Declaration of competing interest

On behalf of all authors, the corresponding author states that there is no conflict of interest.

References

Abbiati, G., Marelli, S., Tsokanas, N., Sudret, B., & Stojadinović, B. (2020). A global sensitivity analysis framework for hybrid simulation. *Mechanical Systems and Signal Processing*, *146*. https://doi.org/10.1016/j.ymssp.2020.106997

Antony, J. (2014). *Design of experiments for engineers and scientists*. Elsevier.

Asprone, D., Menna, C., Bos, F. P., Salet, T. A. M., Mata-Falcón, J., & Kaufmann, W. (2018). Rethinking reinforcement for digital fabrication with concrete. *Cement and Concrete*

Research, *112*, 111–121. https://doi.org/10.1016/J.CEMCONRES.2018.05.020

Aw, Y. Y., Yeoh, C. K., Idris, M. A., Teh, P. L., Hamzah, K. A., & Sazali, S. A. (2018). Effect of printing parameters on tensile, dynamic mechanical, and thermoelectric properties of FDM 3D printed CABS/ZnO composites. *Materials*, *11*(4), 466.

Berveiller, M., Sudret, B., & Lemaire, M. (2006). Stochastic finite element: A non intrusive approach by regression. *European Journal of Computational Mechanics*, *15*(1–3), 81–92. https://doi.org/10.3166/remn.15.81-92

Blatman, G., & Sudret, B. (2011). Adaptive sparse polynomial chaos expansion based on least angle regression. *Journal of Computational Physics*, *230*(6), 2345–2367. https://doi.org/10.1016/j.jcp.2010.12.021

Bos, F., Wolfs, R., Ahmed, Z., & Salet, T. (2016). Additive manufacturing of concrete in construction: potentials and challenges of 3D concrete printing. *Virtual and Physical Prototyping*, *11*(3), 209–225. https://doi.org/10.1080/17452759.2016.1209867

Camacho, D. D., Clayton, P., O'Brien, W. J., Seepersad, C., Juenger, M., Ferron, R., & Salamone, S. (2018). Applications of additive manufacturing in the construction industry–A forward-looking review. *Automation in Construction*, *89*, 110–119.

DeJong, M. J., & Vibert, C. (2012). Seismic response of stone masonry spires: Computational and experimental modeling. *Engineering Structures*, *40*, 566–574.

Deman, G., Konakli, K., Sudret, B., Kerrou, J., Perrochet, P., & Benabderrahmane, H. (2016). Using sparse polynomial chaos expansions for the global sensitivity analysis of groundwater lifetime expectancy in a multi-layered hydrogeological model. *Reliability Engineering & System Safety*, *147*, 156–169.

Dubreuil, S., Berveiller, M., Petitjean, F., & Salaün, M. (2014). Construction of bootstrap confidence intervals on sensitivity indices computed by polynomial chaos expansion. *Reliability Engineering and System Safety*, *121*, 263–275. https://doi.org/10.1016/j.ress.2013.09.011

Efron, B., Hastie, T., Johnstone, I., & Tibshirani, R. (2004). Least angle regression. *The Annals of Statistics*, *32*(2), 407–499. https://doi.org/10.1214/009053604000000067

Feng, P., Meng, X., Chen, J.-F., & Ye, L. (2015). Mechanical properties of structures 3D printed with cementitious powders. *Construction and Building Materials*, *93*, 486–497.

Gibbons, J. D., & Chakraborti, S. (2014). *Nonparametric statistical inference*. CRC press.

Del Giudice, L., & Vassiliou, M. F. (2020). Mechanical properties of 3D printed material with binder jet technology and potential applications of additive manufacturing in seismic testing of structures. *Additive Manufacturing*, *36*, 101714. https://doi.org/10.1016/j.addma.2020.101714

Del Giudice, L., Wrobel, R., Katsamakas, A. A., Leinenbach, C., & Vassiliou, M. F. (2021). Cyclic testing of 1: 40 scale cantilever RC elements with digitally manufactured reinforcement. In *8th International Conference on Computational Methods in Structural Dynamics and Earthquake Engineering (COMPDYN 2021)* (pp. C–18965).

Del Giudice, L., Wróbel, R., Katsamakas, A. A., Leinenbach, C., & Vassiliou, M. F. (2022). Physical modelling of reinforced concrete at a 1:40 scale using additively manufactured reinforcement cages. *Earthquake Engineering and Structural Dynamics*, *51*(3), 537–551. https://doi.org/10.1002/eqe.3578

Harenberg, D., Marelli, S., Sudret, B., & Winschel, V. (2019). Uncertainty quantification and global sensitivity analysis for economic models. *Quantitative Economics*, *10*(1), 1–41.

ISO/ASTM52900-15. (2009). *ACF on AM Technologies, Standard terminology for additive manufacturing-general principles and terminology*.

Jiang, C., & Zhao, G. F. (2015). A Preliminary Study of 3D Printing on Rock Mechanics. *Rock Mechanics and Rock Engineering*, *48*(3), 1041–1050. https://doi.org/10.1007/s00603-014-0612-y

Ligon, S. C., Liska, R., Stampfl, J., Gurr, M., & Mülhaupt, R. (2017, August 9). Polymers for 3D Printing and Customized Additive Manufacturing. *Chemical Reviews*. American Chemical Society. https://doi.org/10.1021/acs.chemrev.7b00074

Lüthen, N., Marelli, S., & Sudret, B. (2021). Sparse polynomial chaos expansions: Literature survey and benchmark. *SIAM/ASA Journal on Uncertainty Quantification*, *9*(2), 593–649.

Lüthen, N., Marelli, S., & Sudret, B. (2022). Automatic selection of basis-adaptive sparse polynomial chaos expansions for engineering applications. *International Journal for Uncertainty Quantification*, *12*(3).

Marelli, S., & Sudret, B. (2014). UQLab: A Framework for Uncertainty Quantification in Matlab. In *Vulnerability, Uncertainty, and Risk: Quantification, Mitigation, and Management - Proceedings of the 2nd International Conference on Vulnerability and Risk Analysis and Management, ICVRAM 2014 and the 6th International Symposium on Uncertainty Modeling a* (pp. 2554–2563). Liverpool, United Kindom. https://doi.org/10.1061/9780784413609.257

McKay, M. D. (1992). Latin hypercube sampling as a tool in uncertainty analysis of computer models. *Proceedings - Winter Simulation Conference*, 557–564. https://doi.org/10.1145/167293.167637

McKillip, W. J. (1989). Chemistry of furan polymers. ACS Publications.

Menna, C., Mata-Falcón, J., Bos, F. P., Vantyghem, G., Ferrara, L., Asprone, D., et al. (2020). Opportunities and challenges for structural engineering of digitally fabricated concrete. *Cement and Concrete Research*, *133*, 106079.

Montgomery, D. C. (2017). *Design and analysis of experiments*. John Wiley & Sons.

Mueller, J., Shea, K., & Daraio, C. (2015). Mechanical properties of parts fabricated with inkjet 3D printing through efficient experimental design. *Materials and Design*, *86*, 902–912. https://doi.org/10.1016/j.matdes.2015.07.129

Murr, L. E. (2015). Metallurgy of additive manufacturing: Examples from electron beam melting. *Additive Manufacturing*, *5*, 40–53. https://doi.org/10.1016/j.addma.2014.12.002

Primkulov, B., Chalaturnyk, J., Chalaturnyk, R., & Zambrano Narvaez, G. (2017). 3D printed sandstone strength: curing of furfuryl alcohol resin-based sandstones. *3D Printing and Additive Manufacturing*, *4*(3), 149–156.

Principe, M., Martínez, R., Ortiz, P., & Rieumont, J. (2000). The polymerization of furfuryl alcohol with p-toluenesulfonic acid: photocross-linkeable feature of the polymer. *Polímeros*, *10*, 8–14.

Ritter, S. (2017). Experiments in tunnel-soil-structure interaction. *PhD Thesis, University of Cambridge*.

Saltelli, A., Ratto, M., Andres, T., Campolongo, F., Cariboni, J., Gatelli, D., et al. (2008). *Global sensitivity analysis: the primer*. John Wiley & Sons.

Schmitt, C. R. (1974). Polyfurfuryl alcohol resins.

Shahrubudin, N., Lee, T. C., & Ramlan, R. (2019). An overview on 3D printing technology: Technological, materials, and applications. *Procedia Manufacturing*, *35*, 1286–1296. https://doi.org/10.1016/j.promfg.2019.06.089

SIA 262/1:2013. (2013). SIA 262/1:2013 - Annex G. Concrete Structures - Supplementary specifications.

Smola, A. J., & Schölkopf, B. (2004). A tutorial on support vector regression. *Statistics and Computing*, *14*(3), 199–222.

Sobol, I. M. (1993). Sensitivity analysis for non-linear mathematical models. *Mathematical Modelling and Computational Experiment*, *1*, 407–414.

Stansbury, J. W., & Idacavage, M. J. (2016). 3D printing with polymers: Challenges among expanding options and opportunities. *Dental Materials*, *32*(1), 54–64. https://doi.org/10.1016/j.dental.2015.09.018

Sudret, B. (2008). Global sensitivity analysis using polynomial chaos expansions. *Reliability Engineering and System Safety*, *93*(7), 964–979. https://doi.org/10.1016/j.ress.2007.04.002

Tian, W., & Han, N. V. (2017). Mechanical properties of rock specimens containing pre-existing flaws with 3 D printed materials. *Strain*, *53*(6), e12240.

Torre, E., Marelli, S., Embrechts, P., & Sudret, B. (2019). Data-driven polynomial chaos expansion for machine learning regression. *Journal of Computational Physics*, *388*, 601–623.

Upadhyay, M., Sivarupan, T., & El Mansori, M. (2017). 3D printing for rapid sand casting—A review. *Journal of Manufacturing Processes*, *29*, 211–220. https://doi.org/10.1016/j.jmapro.2017.07.017

Wang, G. G. (2003). Adaptive response surface method using inherited Latin hypercube design points. *Journal of Mechanical Design, Transactions of the ASME*, *125*(2), 210–220. https://doi.org/10.1115/1.1561044

Wohlers, T. (2014). Wohlers report. *Wohlers Associates Inc*.

Xiao, H., Han, W., Ming, Y., Ding, Z., & Duan, Y. (2019). A sensitivity analysis-based parameter optimization framework for 3D printing of continuous carbon fiber/epoxy composites. *Materials*, *12*(23). https://doi.org/10.3390/ma122333961

Xiu, D., & Karniadakis, G. E. (2002). The Wiener-Askey polynomial chaos for stochastic differential equations. *SIAM Journal on Scientific Computing*, *24*(2), 619–644.

Zhao, D., Guo, W., Zhang, B., & Gao, F. (2019). Investigation on moist silica sand's circulation for sand mold printing with line-forming. *Rapid Prototyping Journal*, *25*(8), 1411–1420. https://doi.org/10.1108/RPJ-05-2018-0113

4. Physical modelling for centrifuge testing of unreinforced masonry walls using sand-based 3D printer

This chapter consists of the draft version of the following article, differing from the original only in terms of layout and formatting:

Del Giudice, L., Katsamakas, A., Liu, B., Sarhosis, V. & Vassiliou, M. F. (2023). Physical modelling for centrifuge testing of unreinforced masonry walls. *Draft*.

Abstract

Centrifuge testing of small-scale physical models of masonry structures can be useful both to study Soil Structure Interaction problems and to provide large enough datasets to statistically validate the global level assumptions of masonry numerical models. This paper proposes the use of a sand-based Binder Jet 3D printer to manufacture 1:10 scaled physical models of masonry walls. As such printers can only print one material, mortar is emulated by controlling the micro geometry of the printed material at the position of the joints, i.e. by printing joints. Walls were tested in compression and cyclic shear under fixed-fixed conditions and constant compressive load. Different notch geometries were tried. The tested specimens were found to behave similarly in compression and shear to full scale prototype walls. Therefore, such small-scale models can be used to expand centrifuge modeling in structural engineering.

4.1 Introduction

As discussed in (Del Giudice et al., 2022), there are two reasons why small scale (1:10 or even smaller) physical models of masonry are useful in structural engineering. The first reason is to use small scale physical models in centrifuge modelling of Soil Structure Interaction problems, both dynamic and static. For example, Ritter et al. (Ritter, 2017; Ritter et al., 2017, 2020) built physical models of masonry using a 3D printer and used them to study the building response to foundation settlements. In their study, they treated masonry as a homogeneous orthotropic material, an approach that can be seen as a first approximation that can be improved.

The second reason is related to Earthquake Engineering. In his opinion paper Bradley (Bradley, 2013) identified system-level ("global") assumptions (e.g. global damping formulation, component interaction, boundary conditions) of numerical models as a major and often disregarded source of error. Such an error could provide an explanation for the documented poor performance of numerical models in predicting the shake table test results of masonry

structures (Mendes et al., 2017; Parisse et al., 2021). This highlights the need for more data from system-level shake table tests, so that the system-level assumptions are better evaluated and validated. In parallel, (Bachmann et al., 2018) have shown that often it is impossible to validate numerical models deterministically (i.e. by trying to predict the response to individual ground motions). Therefore, it has been argued that models should be validated in the statistical sense (Malomo et al., 2021; Reggiani Manzo et al., 2022; Vassiliou et al., 2021; Zhong & Christopoulos, 2021, 2023), namely by trying to predict the statistical distribution of the temporal maxima of the responses to an ensemble of ground motions, with each ground motion applied to a virgin specimen. Clearly this is not feasible in full scale and (Del Giudice et al., 2022; Del Giudice & Vassiliou, 2020) have suggested that the validation of the global level assumptions could be performed against small scale shake table tests, executed within a centrifuge.

It is well known (Abrams, 1996; Benjamin & Williams, 1957; Drysdale et al., 1994; Hamid et al., 1986; Hendry & Murthy, 1965; Hendry & Sinha, 1969; Mohammed, 2006; Mohammed & Hughes, 2011; Sinha & Hendry, 1969; Tomaževič et al., 1990; Tomaževič, 1987) that scaling distorts the mechanical properties of masonry. A physical model made by a 3D printer that would unavoidably be using materials different to bricks and mortar to model masonry is expected to be even more distorted. However, the goal of the approach that this paper suggests is to validate the global level assumptions for given and experimentally obtained (at the model scale) component level behavior; not to create perfectly undistorted models. Therefore, it needs to be underlined that the purpose of the small-scale tests is not to determine the component level behavior of full-scale masonry walls. This is feasible only with large (preferably full) scale component-level tests.

Alternatively, such small-scale specimens could be manufactured by hand using small scale bricks and model-mix mortar. At a scale useful for centrifuge testing (say 1:10 or smaller), such specimens would be distorted, as the behavior of both mortar and bricks is scale dependent (Petry & Beyer, 2014). Plus, their precise manufacturing would be very time consuming. 3D printed specimens will also be distorted, but are much faster to build. A Binder Jet 3D Printer (BJ3DP) can produce a 1:10- scale model of 4 m x 4 m single story masonry building in less than 10 hours, without the presence of an operator (it can run overnight). Moreover, it does not require long curing times, as it only needs 30 min of thermal post processing at 80°C. The major difficulty is that BJ3DPs are able to print only one material, while masonry comprises two materials, namely bricks and mortar, with the former being much stronger. Multi-material

printers do exist, but they print polymers which are not suitable for modelling brittle materials like masonry, because they are ductile, and their behavior is strongly rate dependent. To overcome this drawback, this paper focuses on masonry structures with walls under relatively low axial load. Then, in-plane failure is dominated by sliding and stair-like cracks that propagate through the mortar joints. The physical models were manufactured by a single-material printer and have notches of controlled geometry at the place of the joints, so that the cracks are forced to propagate through them. So, instead of using a different material for the mortar, it is the local micro-geometry of the same material that is modulated.

This paper presents the results of 1:10 printed models of masonry walls tested in-plane under constant compressive and cyclic shear load. In total, 11 walls with geometries selected from a preliminary testing phase are tested. The effect of the notch geometry is studied by comparing the differences in stiffness, strength, and displacement capacity of the specimens with different notch geometry. The failure mode of all samples is identified by visual inspection of the samples and by using Digital Image Correlation which provides full strain fields.

4.2 Binder jet 3D printer

The BJ3DP used to manufacture the 1:10-scale model walls object of this study is a Voxeljet VX500. It has a building space of 500x400x300 mm (length x width x height). A detailed description of this printer can be found in (Del Giudice & Vassiliou, 2020). However, this section does offer a concise description of how the 3D printer works is provided in this paper to explain some of the design choices made in a later section.

The printer process consists of two alternating steps: (a) the recoater deposits a 300 μm powder bed onto the building area; (b) the print head applies the binder in predetermined locations according to the input CAD (Computer Aided Design) model (Figure 1). After the two steps are completed, the building platform lowers by 300 μm. The powder bed is essentially a layer of quartz-sand with a thickness of 300 μm and it is deposited by the recoater at a speed of 50mm/s. The recoater is equipped with a vibrating blade to create a constant sand flow. The binder is sprayed by the Print Head (PH) via 768 piezo-ceramic nozzles which are equally distributed to six printing modules located at the bottom of the PH. The piezo-ceramic outlets are activated by electrical pulses that can be modulated to increase or decrease the quantity of the binder. Each electric pulse creates a single droplet of binder that is sprayed from a single nozzle. The voltage can be set to a value ranging from 85.5 to 99.0 V and there exists a linear relationship between pulse voltage and droplet mass (Del Giudice et al., 2023). Moreover, one

droplet is intended to bind only the sand included in a single voxel (basic unit of a three-dimensional grid). The voxel size is predefined by the user of the printer and it is fully characterized by three dimensions called dX, dY, and dZ (Figure 1). These correspond to the resolution in the X, Y, and Z directions. The resolution in the Z direction is fixed to 300 μm, i.e. the thickness of the layer deposited by the recoater. The resolution in Y direction is also fixed to 85 μm by the manufacturer. The resolution in the X direction can range from 80 to 150 μm and it can be controlled by the user.

The properties of the 3D printed bulk material depend on the printer parameters selected by the user. (Del Giudice et al., 2023) quantified the influence of the printing parameters on the material properties and they concluded that the mechanical properties of the printed material are mainly controlled by the voxel resolution dX: Both the uniaxial compressive strength and the Young's modulus decrease monotonically with dX. For instance, (Del Giudice et al., 2023) shows that for dX equal to 150 μm the compressive strength is equal to 7.8MPa and the Young's modulus is equal to 3.62GPa, while for dX equal to 80 μm the compressive strength and stiffness are equal to 15.7MPa and 4.72GPa, respectively.

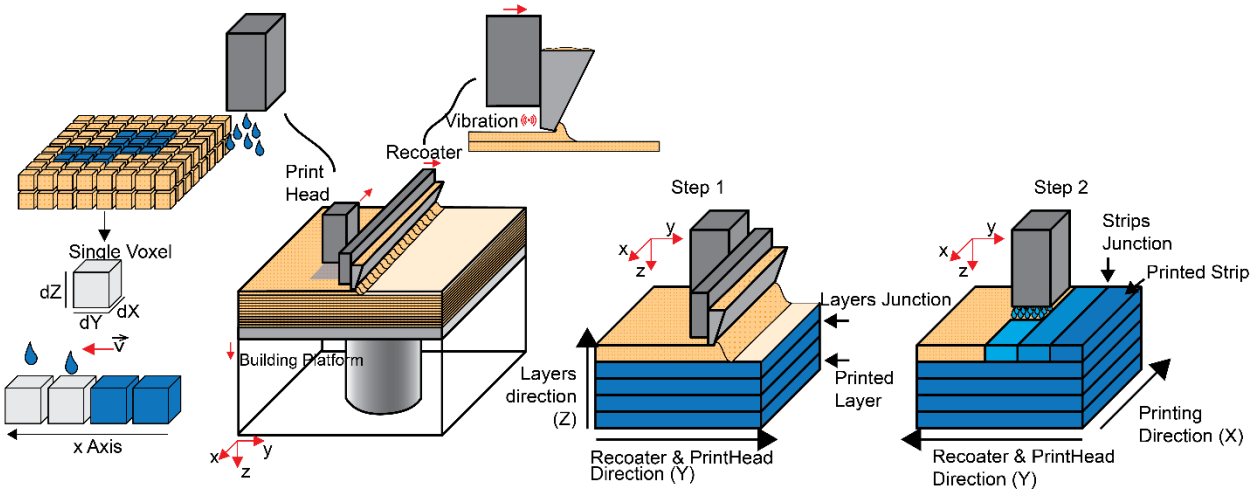

Figure 1. Schematic of the 3D printing process.

In this work, to manufacture a small-scale physical model of masonry, the Young's modulus and compressive strength were maximized by setting dX to 80 μm and the pulse voltage to 99.0 V. With these settings, according to (Del Giudice et al., 2023) the compressive strength and Young's modulus is expected to be equal to roughly 15MPa and 4.7GPa. As the exact mechanical properties of the bulk material also depend on the wear of the printer, they were experimentally obtained for the specific printjob that printed the wall specimens (Section 5).

All printed specimens were thermally post-processed at 80°C for 30 minutes (Del Giudice et al., 2023).

4.3 Specimen description

The specimens were initially designed to physically model a reference prototype studied in (Salmanpour et al., 2015) (sample T2), which is made of clay bricks and has dimensions l_w, h_w, and t_w equal to 2700mm, 2600mm, and 150mm, where l_w, h_w, and t_w correspond to the length, height, and thickness of the wall, respectively. However, the model wall dimensions were subsequently adjusted based on the capacity of the 3D printer (building volume and resolution).

The design process started by scaling the geometry of the single clay bricks used in (Salmanpour et al., 2015), i.e. 190mm in height, 150mm in thickness, and 290mm in length. These dimensions were reduced to 1:10, i.e. 19mm for the brick height, 15mm for the thickness, and 29mm for the length of each model brick. The prototype wall consisted of 13 rows of bricks and 9 full bricks in the horizontal direction. The 3d printed model also consisted of the same number of bricks.

The vertical and horizontal notches correspond to head and bed joints, respectively. Each notch is defined by its width (w_n) and thickness (t_n). The thickness, t_n, is in excess of the brick dimensions. The vertical notches go through the thickness of the wall, while the horizontal notches go through the entire length of the wall. Figure 2 shows a schematic of the model wall with the nomenclature used for the joints (notches). Bottom and top connection beams were also printed together with the model wall. These were used to connect the specimen to the test setup described in the next Section. Notably, due to the printing process described in the previous section, the notches were unavoidably full of unbound sand, as it did not flow out of the notches and it was impossible to force it out using compressed air.

This paper presents the results of tests on these 11 walls. Table 1 offers their geometric characteristics. The first six walls (SW01 - SW06) have different geometric characteristics of the horizontal and vertical notches. Specimens SW07 and SW08 are identical to SW06 and were tested to evaluate the repeatability of the tests. Specimens SW09-SW11 were identical to SW06-SW08 and were tested under smaller compressive load. SW01-SW08 were tested under compressive stress, s_o, equal to 7.21% of the compressive strength of the walls, f_x, while SW9-SW11 were tested under s_o/f_x=3.60%. These values correspond to stresses s_o equal to 0.38MPa and 0.75MPa, and compressive forces N equal to 1.51 and 3.02 kN. Also, Table 1 presents the compressive load of the specimens normalized to the compressive strength of the masonry wall,

(f_x); which was found not to significantly depend on the size of the notches tested (as discussed in detail in Section 5).

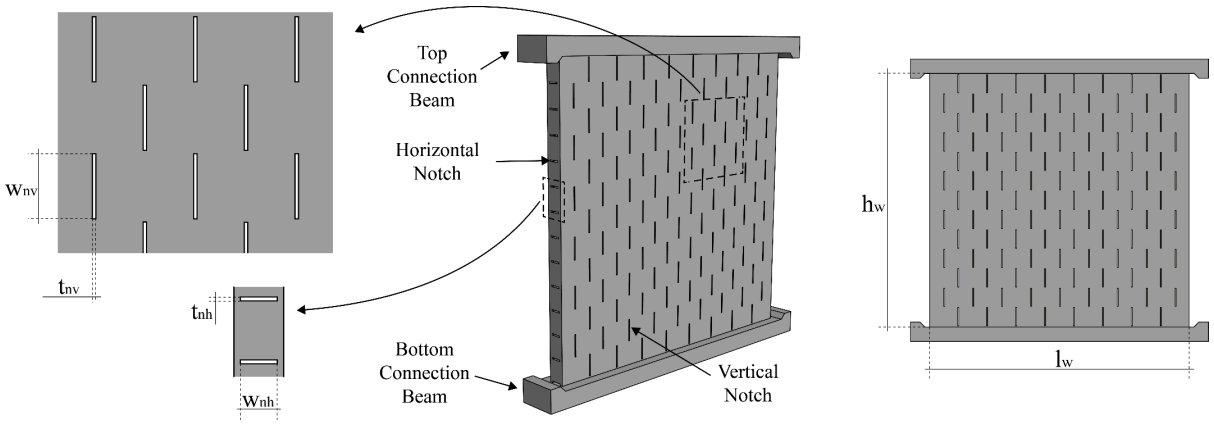

Figure 2. Geometry of the model walls.

Label	t_w	l_w	h_w	t_{nh}	w_{nh}	t_{nv}	w_{nv}	σ_0/f_b	σ_0/f_x	σ_0	N
	mm	mm	mm	mm	mm	Mm	mm	%	%	MPa	kN
SW01	15	269	259.7	1	6	1	18.9	5	7.21	0.75	3.02
SW02	15	269	259.7	1	9	1	18.9	5	7.21	0.75	3.02
SW03	15	269	259.7	1	11	1	18.9	5	7.21	0.75	3.02
SW04	15	269	262.5	1.2	6	1	18.9	5	7.21	0.75	3.02
SW05	15	269	262.5	1.2	9	1	18.9	5	7.21	0.75	3.02
SW06	15	269	262.5	1.2	11	1	18.9	5	7.21	0.75	3.02
SW07	15	269	262.5	1.2	11	1	18.9	5	7.21	0.75	3.02
SW08	15	269	262.5	1.2	11	1	18.9	5	7.21	0.75	3.02
SW09	15	269	262.5	1.2	11	1	18.9	2.5	3.60	0.38	1.52
SW10	15	269	262.5	1.2	11	1	18.9	2.5	3.60	0.38	1.52
SW11	15	269	262.5	1.2	11	1	18.9	2.5	3.60	0.38	1.52

Table 1. Model walls' labels and geometries.

Notably, more node configurations were preliminary tested, having smaller or larger notches, but they were either too weak to handle (because the notches were too wide), or did not fail with a diagonal step-like crack (because the notches were too small). These preliminary tests are not reported in detail in this paper.

4.4 Setup, measurements and testing procedure

Figure 3 shows the setup used for the in-plane cyclic loading tests. The setup was designed so that it can apply horizontal deformation, while keeping the vertical compressive force constant under fixed-fixed (i.e. zero rotation) conditions at the top and bottom ends of the specimen. Overall, the setup is a closed reaction frame which does not require a strong floor. The bottom and top connection beams of the specimen are connected to the loading beam and to the base

with stoppers which prevent the samples from sliding. The horizontal electromechanical actuator reacting on a reaction column imposes shear forces at the top of the specimens through a loading beam assembly composed of two HEA200. The vertical load is applied by two electromechanical actuators reacting on the top beam of the reaction frame. To prevent the out-of-plane motion of the loading beams, a system of restrainers was used to guide the flanges of the top loading beam (the restraining system is not shown in Figure 3).

A mixed force-displacement control was applied at the two vertical actuators, so that they apply both a constant sum of compressive load $N = N_N + N_S$ and an equal displacement $D = D_N = D_S$ that leads to zero rotation of the loading beam (N_N, N_S, D_N, D_S are the force and displacement of the northern and southern actuator respectively). The mixed force-displacement control of the vertical actuators is achieved by first coupling D_N to D_S, i.e. by enforcing that the two actuators will have the same displacement. Subsequently, to impose a constant axial force on the specimen, a force control feedback loop was developed and calibrated. The controller used as feedback a virtual channel given by the sum of the vertical forces (N_N and N_S), which was updated at each GINLink bus cycle of the control system at a frequency of 4 kHz.

The applied forces were measured with three uniaxial load cells, which were mounted coaxially to the cylinders of the electromechanical actuators (Figure 3). In addition, a multi-axial-load-cell (MALC) that can measure shear loads up to 23kN, axial load up to 182kN, and bending moment of 5kNm, was installed below the specimens. The MALC measures the applied forces without the friction of the setup. Displacements were measured with two laser sensors mounted on the north side of the specimen and pointed at the top and at the bottom stopper (Figure 4). The front side of the specimen was monitored with 3D digital image correlation (DIC). In principle DIC, is a non-contact optical metrology that uses digital image processing and numerical computation. It provides the full displacement and strain field of a surface by comparing the images of the specimen before and after deformation. This technology relies on a contrasting speckle pattern on the surface of the specimen, which can be provided by the texture of the sample or it can be artificially produced. The contrast of the speckle pattern and the size of the speckles have a dominant influence on the performance of the DIC. In order to provide the maximum contrast possible, the surface of the specimen was given two coats of matte white paint and then a speckle pattern was applied with the use of a special roller provided by Correlated Solutions (“Correlated Solutions Digital Image Correlation,” 2022) (Figure 4, right). The size of each speckle is also important to avoid aliasing (Kovarbašić et al.,

2021; Mata-Falcón et al., 2020). A rule of thumb is that each speckle must be at least 5-8 pixels, which in this case corresponds to a speckle size of 0.18mm.

The specimens were first loaded axially by the two vertical actuators. Then, the horizontal actuator applied a quasi-static cyclic shear displacement. Each cycle was repeated twice before increasing the amplitude. The loading rate was defined based on the target displacement of each cycle, i.e. for small amplitudes the actuator speed was slower, while for larger amplitudes it was faster (Table 2). The feedback used to control the horizontal actuator displacement is given by the 2 poles resolver mounted on the brushless motor of the actuator, i.e it was measured internally in the actuators; not externally.

Target drift (%)	0.10	0.20	0.30	0.40	0.50	0.60	0.70	0.80	1.00	1.20	1.50	2.00
Target Displacement (mm)	0.26	0.52	0.78	1.04	1.3	1.56	1.82	2.08	2.6	3.12	3.9	5.2
Speed (mm/s)	0.02	0.02	0.03	0.04	0.05	0.06	0.06	0.06	0.06	0.06	0.06	0.1
Period (s)	52	104	104	104	104	104	121	139	173	208	260	208

Table 2. Applied horizontal loading history.

4.5 Bulk material and wallet tests

All the specimens were printed in one batch that included a) Cylindrical specimens to determine the compressive strength of the bulk material; b) Wallets to determine the compressive strength of the masonry assembly; and c) Walls to test them under combined compressive and cyclic shear loading (see Figure 5).

The compressive strength, f_b, and the Young's modulus E_b of the printed bulk material were characterized with three uniaxial compression tests, performed according to the SIA 262-Annex G Standard (SIA 262/1:2013, 2013). The samples for these tests were cylinders with diameter of 50 mm and height of 100 mm. The compressive strength of the bulk material, f_b, was 14.95MPa (CoV = 1.7%), and the Young's modulus, E_b, was 4.67GPa (CoV = 2.9%). Both values refer to the z direction (Figure 1), as the material is slightly orthotropic (Del Giudice & Vassiliou, 2020).

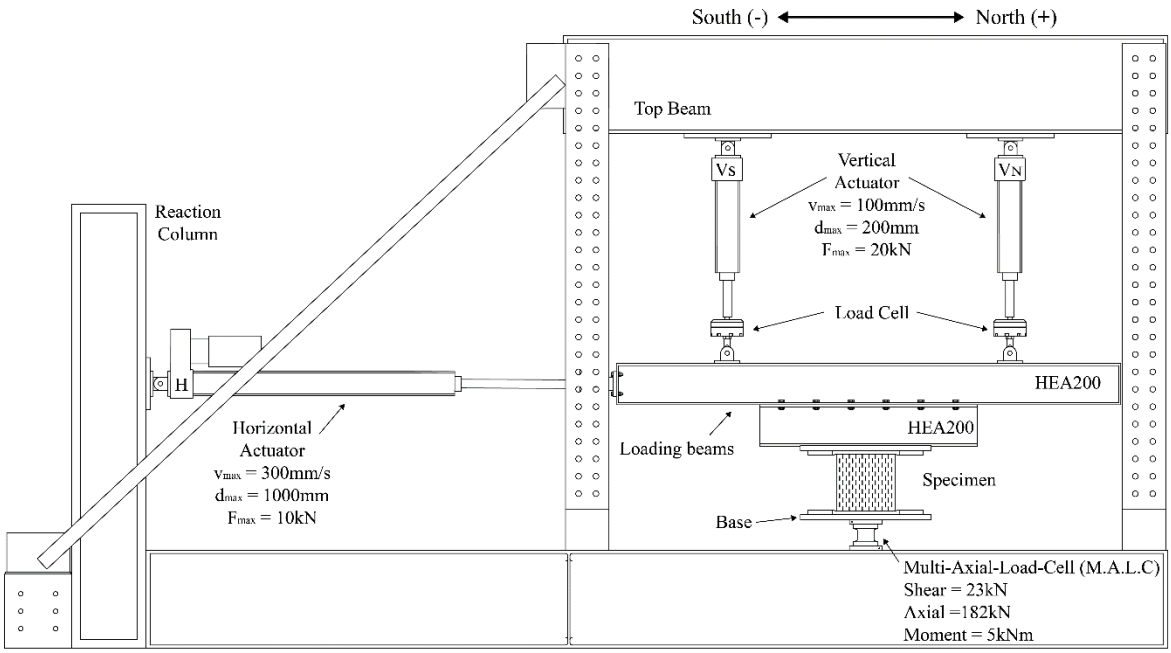

Figure 3. Schematic of the test set-up.

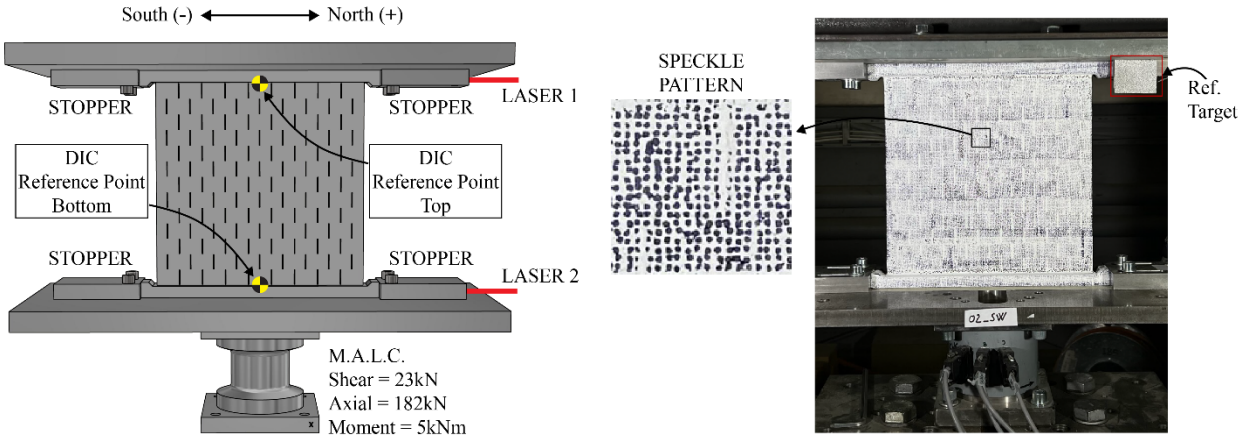

Figure 4. Instrumentation for the specimens.

The characterization of the compressive strength, f_x, and Young's modulus, E_x, of the model walls was performed on samples conforming to CEN 2002 (CEN, 2002) at a scale of 1:10, i.e. on wallets with two bricks in the horizontal direction and five bricks in the vertical direction (Figure 6). The tests were performed in a universal testing machine and the strains were measured with an axial extensometer, which measures strains on opposite sides of the samples independently. The modulus of elasticity (E_x) was then computed as the secant modulus at a stress equal to one third of the compressive strength (f_x). Six samples (W01 through W06), representing the different notch geometry of the model walls were tested (Table 3).

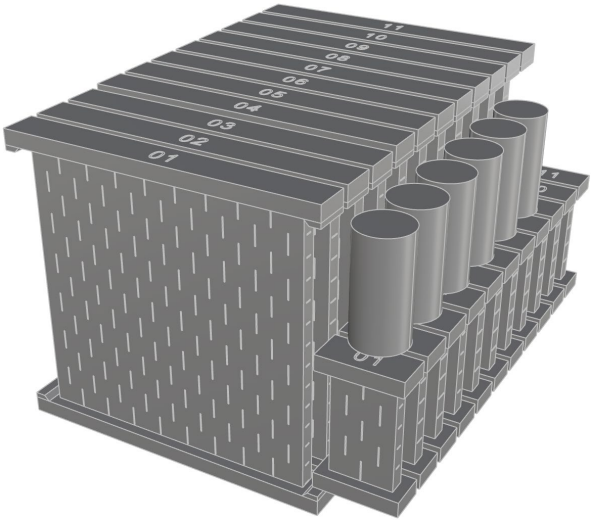

Figure 5. 3D model of the print job including, model walls, wallets, and cylindrical specimens.

The compressive strength of the wallets (f_x) and the modulus of elasticity (E_x) seem to reduce with increasing width of the horizontal notch (w_{nh}), with W03 being an outlier. However, a formal two-way analysis of variance (ANOVA) (Del Giudice & Vassiliou, 2020; Montgomery, 2017) considering w_{nh} and t_{nh} as the two treatments of the study was performed for f_x and E_x. For f , the resulting p-values were 0.38 and 0.79 for t_{nh} and w_{nh}, respectively, showing that their influence on f_x is not statistically significant – at least for the range of the values of t_{nh} and w_{nh} considered. The results of the two-way ANOVA for E_x resulted in p-values of 0.18 and 0.56 for t_{nh} and w_{nh}, respectively, which indicates that the influence of the notch geometry on the Young's modulus is not statistically significant. Therefore, the mean value of f_x=10.40MPa was used for normalizing the compressive load of the shear tests.

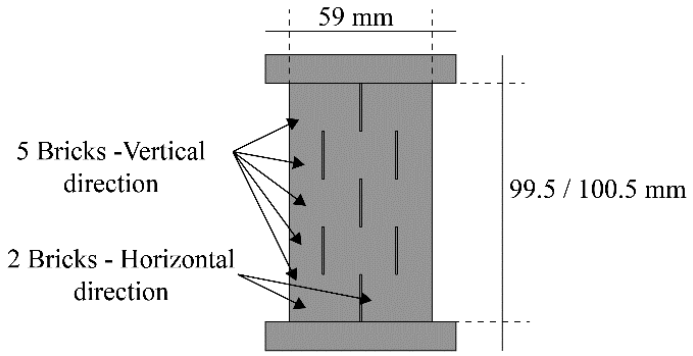

Figure 6. Wallet geometry.

Sample	t_w mm	l_w mm	h_w mm	t_{nh} mm	w_{nh} mm	w_{nv} mm	f_x MPa	E_x MPa
W01	15	59	99.5	1	6	18.9	10.350	4211.2
W02	15	59	99.5	1	9	18.9	10.339	4125.5
W03	15	59	99.5	1	11	18.9	12.441	4221.8
W04	15	59	100.5	1.2	6	18.9	10.960	4092.6
W05	15	59	100.5	1.2	9	18.9	9.288	3947.1
W06	15	59	100.5	1.2	11	18.9	9.040	3635.8

Table 3. Wallets' geometry, compressive strength, and Young's modulus horizontal to the bed joints.

4.6 Cyclic test results and discussion

4.6.1 Results

This section describes the main test results of the 1/10 in scale cyclic tests shown in Figure 3. The tests included 11 model walls whose geometry is described in Section 3 and reported in Table 1. The force-drift curves reported in this section are based on the measurements provided by the DIC. The drift ratio (δ) is defined as the difference of the horizontal displacement of two reference points at the top and bottom of each wall (Figure 4), divided by their vertical distance. The DIC measurements were chosen (instead of the lasers) in order to avoid the error induced by the sliding that might occur between the wall and the testing apparatus. It was not possible to test wall SW07, since it was damaged during installation. Therefore, results reported below do not include wall specimen SW07.

Figures 7 and 8 show the main results of the cyclic tests. In particular, Figures 7 and 8 show a) the experimental cyclic loops with their envelopes; b) the field of the principal strain, at the time instant of the peak lateral force (V_{max}); and c) the final crack pattern of each wall. Table 4 shows the maximum shear force (V_{max}) at the North and South direction, as well the maximum drifts (δ_{max}) for which the V_{max} was attained.

Walls SW01, SW02, and SW03 had the same vertical notch geometry and horizontal notch thickness. They were all tested at pre-compression level of 7.21% of the wallet compressive strength, f_x. The sole difference among them is the width of the horizontal notches (w_{nh}), which is 6 mm, 9 mm, and 11 mm, for SW01, SW02, and SW03, respectively. The test of the wall SW01 was stopped because the bottom connection beam failed at the interface with the south stopper (stoppers are shown in Figure 4). This allowed the sample to slide freely and it prevented any increase of stresses within the wall. However, the experimental curve in Figure 7 shows that SW01 did reach the post elastic branch. SW01 reached almost identical maximum forces in the north (+), and south (-) direction. The maximum force in the north direction

($V_{max,N}$) was equal to 2.33 kN and the corresponding drift ratio ($\delta_{Vmax,N}$) was equal to 0.77 %. In the south direction, the maximum lateral force ($V_{max,S}$) was equal to 2.33 kN at a drift ratio ($\delta_{Vmax,S}$) equal to 1.07 %. The principal strain field (ε_1) at $V_{max,S}$ shows an increased strain along the diagonal for the wall SW01. In addition, strain concentrations were also visible at the base of the wall due to shear sliding and the top right corner due to local crushing.

Wall SW02 had the same boundary conditions and pre-compression with SW01, but it had a larger horizontal notch width (w_{nh}) equal to 9mm. The first visible crack was at the interface between the wall and the top connection beam. The crack propagated horizontally from the top right corner through the bed joint until the middle of the wall length. Then, it continued to propagate diagonally in a diagonal step-shaped crack pattern. The crack onset started after the wall reached its maximum load ($V_{max,S}$) equal to 2.31 kN at a drift of 0.47 %. In the north direction, SW02 reached a peak load ($V_{max,N}$) equal to 2.07 kN at a drift of $\delta_{Vmax,N}$ = 0.56 %. The maximum load in both directions was followed by an abrupt strength loss, which corresponds to the crack formation. Subsequently, the wall exhibited a sliding response along the diagonal shear step-shaped cracks and the horizontal cracks. This is clearly identifiable from the experimental curve: in the last cycles there is not any increase in strength for increasing drift amplitudes; it is essentially a pure friction behavior.

Test SW03 differed from SW01 and SW02 only in w_{nh}, which was even larger and equal to 11 mm. The force-drift loop had a similar shape to the one of SW02 (Figure 7). The lateral force reached a maximum value of $V_{max,N}$ equal to 1.94 kN in the north direction at a drift of 0.42 %, and $V_{max,S}$ equal to 1.99 kN in the south direction at a drift of 0.23 %. After the peak force, there was a sudden drop in strength followed by a force plateau, which represented a sliding behavior. The failure type of SW03 was pure sliding along one horizontal bed joint (Figure 7). The sliding crack formed at the bed joint between the first and second brick row from the top of the wall. When $V_{max,S}$ occurred, the DIC showed that the principal strain, ε_1, was increased along the wall diagonally, but was overall maximum along the topmost horizontal notch where sliding occurs.

Compared to SW01, SW02 and SW03, specimens SW04, SW05 and SW06, only had thicker horizontal notches (i.e. t_{nh} equal to 1.2 mm instead of t_{nh} equal to 1 mm). Wall SW04 first developed shear cracks at the corners. The shear crack that initated immediately on the top-north side and propagated diagonally. Moreover, cracking bricks in the top two rows ob-

served. With the application of further load, cracking continued along the notches. On the contrary the crack that started at the bottom-south corner propagated horizontally and then diagonally, always through the notches. The maximum loads in the two directions were $V_{max,N}$ equal to 2.31 kN and $V_{max,S}$ equal to 2.30 kN. The corresponding drifts were $\delta_{Vmax,N}$ equal to 1.06 %, and $\delta_{Vmax,S}$ equal to 0.30 %. Although the results show a symmetric shear resistance, the drift was not symmetric in the two directions.

The experimental force-drift loops of SW05 were quite symmetric both with respect to the lateral force and to the drift ratio ($V_{max,N}$ = 1.95 kN, $V_{max,S}$ = 2.10 kN, $\delta_{Vmax,N}$ = 0.37 %, and $\delta_{Vmax,S}$ = 0.29 %). In SW05 specimen, the first crack initiated along the bed joint at the interface between the top connection beam and the wall and then propagated a diagonal step-shape mode. The results from the DIC measurements of SW05 indicate that the strains were concentrated along the vertical and horizontal notches.

SW07 and SW08 were designed to be the same as SW06 to evaluate repeatability of the tests. Unfortunately, SW07 was damaged and was not tested. Both walls SW06 and SW08 had almost identical failure modes with a horizontal sliding crack going through the topmost (SW06) and the second topmost (SW08) bed joint. In both cases, the crack started from the north side during the pulling of the horizontal actuator (north-to-south direction). In terms of shear loads and drifts, SW06 had maximum shear forces, i.e. $V_{max,N}$ equal to 1.88 kN and $V_{max,S}$ equal to1.78 kN; at drift ratios of $\delta_{Vmax,N}$ = 0.37 %, and $\delta_{Vmax,S}$ = 0.24 %; SW08 peak forces were $V_{max,N}$ = 1.52 kN, and $V_{max,S}$ = 1.68 kN at drift ratios of $\delta_{Vmax,N}$ = 0.23 %, and $\delta_{Vmax,S}$ = 0.14 %. Therefore, the maximum shear force shows some reasonable repeatability, but the relevant drift does not. This could be explained considering that the part of the force-deformation curve where the maximum is attained is relatively flat and, therefore, small changes in force would lead to relatively large changes in deformation.

SW09, SW10, and SW11 were also identical to SW06 but the pre-compression level was one half, i.e. 3.6% of f_x, which corresponds to 1.51 kN, or equivalently 0.38 MPa. Again, three specimens were tested to explore repeatability and observe average trends. Notably SW11 was the first wall that was tested and was not perfectly clamped at the bottom and some micro sliding might have occurred. All three models failed in sliding. However, the cracks in the samples propagated along one topmost or second topmost horizontal notch (Figure 8), with the staircase-shape cracks being less pronounced and only present in SW09 and SW10.

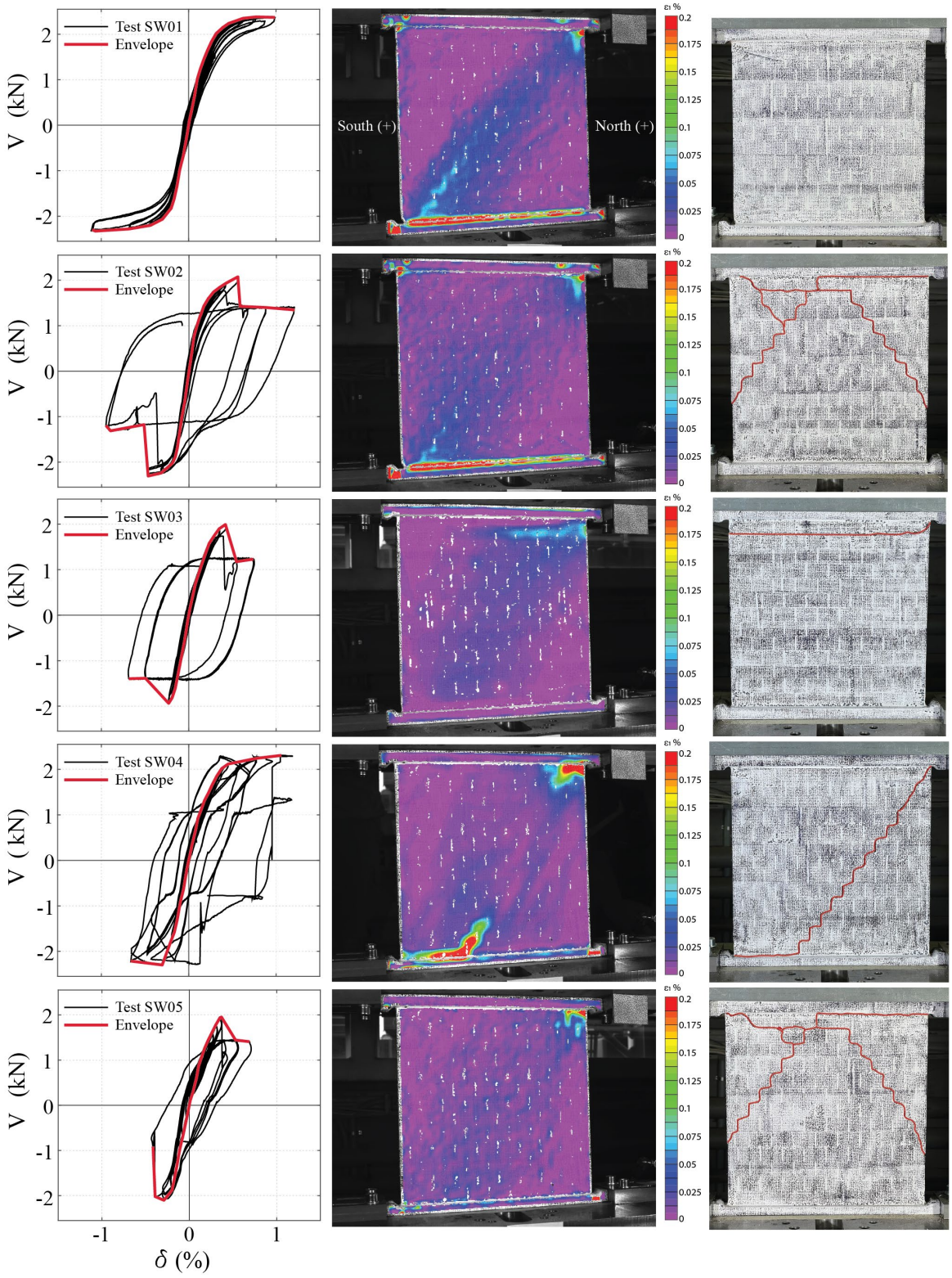

Figure 7. Left: Hysteresis loops and envelope. Center: Principal strain distribution (ε_1) at peak load F_{max}. Right: Crack pattern at failure.

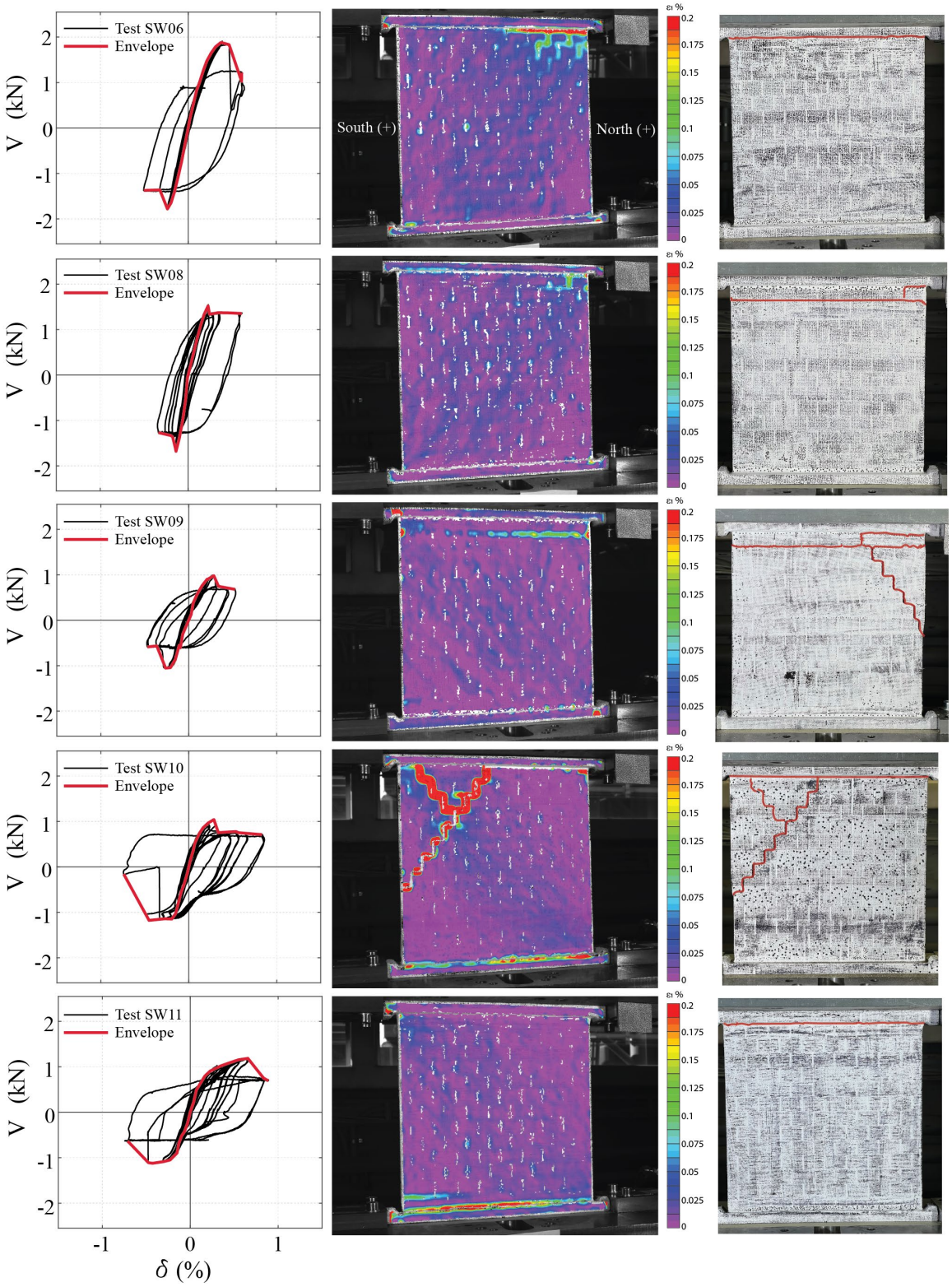

Figure 8. Left: Hysteresis loops and envelope. Center: Principal strain distribution (ε_1) at peak load F_{max}. Right: Crack pattern at failure.

As expected, the lower vertical pre-compression resulted in a reduced shear strength of the specimens. The shear strength in the north direction for SW09 was $V_{max,N}$ equal to 0.98 kN, and in the south direction was $V_{max,S}$ equal to 1.05 kN. Wall SW10 shear strength was $V_{max,N}$ equal to 0.97 kN and $V_{max,S}$ equal to 1.18 kN. Finally, the maximum forces for SW11 were $V_{max,N}$ equal to 1.10 kN, and $V_{max,S}$ equal to 1.12 kN. Again, repeatability in terms of maximum force was observed, but not in terms of deformation at maximum force, as the δ_{Vmax} of SW09 and SW10 fall relatively close to each other, but the δ_{Vmax} of SW11 is significantly larger.

Overall, only sliding modes of failure were observed. The cracks were either only horizontal (SW03, SW06, SW08, and SW11) or a mixture of staircase-like and horizontal. It seems that an increase of the notch width leads the specimen to fail on a horizontal crack (i.e. a pure sliding mode), while a decrease of the notch width promotes a staircase-like crack. For example, for SW04, w_{nh}=6mm and the crack is mainly staircase-like. In SW02 and SW05, w_{nh} equal to 9mm and the crack is a mixture of horizontal and staircase-like. In SW03 and SW06, w_{nh} equal to 11mm and the cracks are horizontal. The thickness of the notch does not seem to influence the failure mode – at least for the small variations of its value studied in this work.

	V_{max} [kN]		δ_{Vmax} [%]	
Specimen	North	South	North	South
SW01	2.38	-2.33	0.77	-1.07
SW02	2.07	-2.31	0.56	-0.47
SW03	1.99	-1.94	0.42	-0.23
SW04	2.31	-2.30	1.06	-0.30
SW05	1.95	-2.10	0.37	-0.29
SW06	1.88	-1.78	0.37	-0.24
SW08	1.52	-1.68	0.23	-0.14
SW09	0.98	-1.05	0.29	-0.26
SW10	1.04	-1.18	0.29	-0.45
SW11	1.19	-1.12	0.66	-0.43

Table 4. Maximum shear force, V_{max}, and drift ratio, δ_{Vmax}, for which V_{max} is attained, in both North and South direction.

4.6.2 Bi-linearization of the lateral force-deformation curves

The backbone curves of the hysteretic loops were approximated with bilinear (elastic, perfectly plastic) envelopes. This simplification is a common approach used for full scale specimens (Salmanpour et al., 2015; Tomazevic, 1999). The bilinear curve was defined by its effective stiffness K_{eff}, its ultimate shear load V_u, and its ultimate displacement d_u (Figure 9). Out of the several bi-linearization methods that have been suggested (Petry & Beyer, 2014; Tomazevic, 1999), this paper uses the method proposed by (Tomazevic, 1999). So, the effective stiffness taken as the secant of the backbone at $0.7V_{max}$, where V_{max} is the maximum load of the cyclic envelope. d_u was defined as the displacement corresponding to a strength degradation of 20%,

i.e. 0.8 V_{max}. The ultimate load, V_u, was obtained with an equal energy rule, namely by equating the areas under the experimental backbone, truncated at d_u, and the bilinear envelope. Finally, the elastic displacement, d_e, was equal to $d_e = V_{max} / K_{eff}$. Since the performed tests were cyclic, for each test two bilinear envelopes were obtained, i.e., one for the north direction and one for the south direction. Next, the average V_u, d_u and d_e were computed, and K_{eff} was defined as the ratio of the average V_u and the average d_e. Table 5 presents the average parameters of the idealised bilinear envelopes according to the described procedure. The parameters related to the displacements are reported in terms of drift ratio (δ). Table 5 also reports the average of V_{max}, the average of δ_{Vmax} the ratio of the average V_u over the average V_{max}, the ratio of the average δ_u over the average δ_e, and V_u normalized to the precompression load of the wall, N.

Figure 10 reports the average (among N-S directions) bilinear curves for all the tests. Walls tested with a lower level of pre-compression (1.51 kN) were plotted with solid red lines. All other colors show the tests with a pre-compression of 3.2 kN.

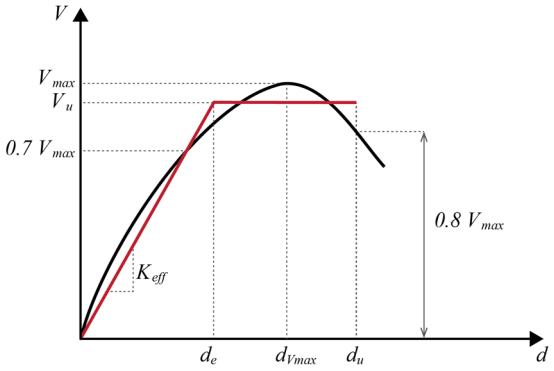

Figure 9. Parameters of the bilinear envelope proposed by Tomaževič (Tomazevic, 1999).

Test	V_{max} kN	δ_{Vmax} %	δ_e %	V_u kN	δ_u %	K_{eff} kN/mm	V_u/V_{max} -	δ_u/δ_e -	V_{max}/N
SW01	2.35	0.92	0.27	2.28	1.04	2.76	0.97	3.90	0.78
SW02	2.19	0.51	0.20	2.06	0.53	3.26	0.94	2.60	0.72
SW03	1.97	0.32	0.22	1.84	0.45	2.58	0.93	2.05	0.65
SW04	2.30	0.68	0.30	2.23	0.86	2.34	0.97	2.91	0.76
SW05	2.03	0.33	0.24	1.91	0.45	2.67	0.94	1.87	0.67
SW06	1.83	0.30	0.22	1.73	0.42	2.64	0.94	1.94	0.61
SW08	1.60	0.18	0.15	1.49	0.40	3.02	0.93	1.47	0.53
SW09	1.02	0.27	0.18	0.96	0.32	2.01	0.94	1.79	0.67
SW10	1.11	0.37	0.16	1.05	0.42	2.42	0.95	2.58	0.74
SW11	1.15	0.54	0.22	1.08	0.67	1.60	0.94	3.07	0.76

Table 5. Parameters of the idealized bilinear envelopes.

The solid black lines show the samples with a horizontal notch thickness, t_{nh}, equal to 1 mm. The black and gray dashed lines show the walls with t_{nh} equal to1.2 mm. The circular markers

indicate the samples with a horizontal notch width of w_{nh} equal to 6 mm, square markers represent specimens with w_{nh} equal to 9 mm, and the triangular markers indicate the walls with w_{nh} equal to 11 mm.

The red curves in Figure 10 are repetitions of the same tests, since SW09, SW10, and SW11 have the same geometry and pre-compression. The three samples have very similar ultimate horizontal load V_u and elastic drift δ_e, unlike the ultimate drift δ_u, which for SW11 was substantially higher. Therefore, apart from the differences in ultimate deformation for SW11, the tests on SW09-SW11 seem repeatable, at least in terms of their bilinear curve.

Figure 10 also shows a clear effect of the vertical pre-compression level on the shear resistance of the model walls: SW06, SW08, SW09, SW10, and SW11 are of the same geometry and they differ only in precompression (the red ones are precompressed with 1.51 kN while the grey ones with 3.02 kN). All these walls are identical except for the level of pre-compression. The average V_u of SW06 and SW08 is 1.61 kN, which is 56% higher than the average ultimate force of SW09-SW11 (V_u = 1.03 kN). Apparently, the horizontal strength does not scale proportionally with the level of precompression, because of the cohesion of the notches. This is also observed in prototype full scale masonry which is often described with a Mohr Coulomb criterion of the form:

$$V_u=C+\mu\times N \tag{1}$$

where V_u is the ultimate shear stress, C is the cohesion, μ is the coefficient of friction and N is the axial precompression.

The horizontal notch thickness t_{nh} has a clear but small effect in the initial stiffness K_{eff}: SW04-SW06 have larger notch thickness compared to their counterparts SW01-SW03 and a smaller K_{eff} (Figure 10).

The horizontal notch width, w_{nh}, affects the mechanical behavior of the specimens the most and the shear strength decreases with the notch size. For example, an increase in the notch size from 6 mm (SW01) to 9 mm (SW03) decreases the ultimate strength from 2.28 kN to 1.84 kN In an attempt to further investigate this behavior, one can observe that the bound part of the "bed joint" is 15 mm – 11 mm = 4 mm (for SW03) and 15 mm – 6 mm = 9 mm. That is, the "bed joints" of SW01 have a bound part twice as large as the one of SW03. However, the horizontal strength of SW01 is only 24% larger. Therefore, it can be concluded that the non-

bound part also contributes to the shear strength, as it comprises a thin layer of unbound sand in compression.

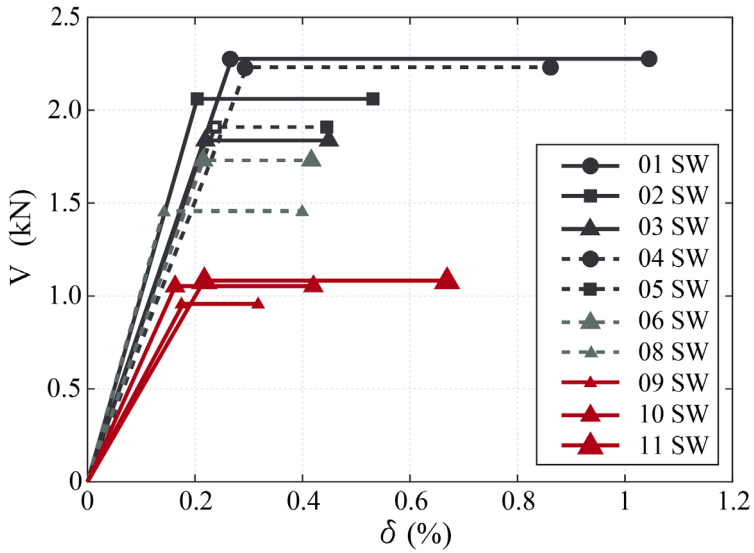

Figure 10. Bilinear envelopes of the model walls.

4.7 Comparison with prototype walls

This section compares the lateral behavior of the model walls to the behavior of prototype walls, as it has been reported in the literature (Messali et al., 2020; Salmanpour et al., 2015). The prototype walls selected for the comparison have similar geometric characteristics, failure type, and pre-compression level to the 1/10-scale model walls that were tested in this work. The first reference wall, named PT-01, is selected from the work of Salmanpour et al. 2015 (Salmanpour et al., 2015) (wall T2 in the original paper). The second prototype wall was tested by (Messali et al., 2020), and it is indicated as PT-02 (wall TUD-COMP 5 in the original paper).

A qualitative comparison unveils that both the prototype exhibited the same failure mode: Sliding, either staircase-shape or solely along the bed joints. To gain more insight on the performance of the physical model, the model and prototype walls were compared quantitatively in terms of their: a) Mohr-Coulomb failure criterion parameters; and b) bilinear curves.

4.7.1 Comparison based on Mohr Coulomb parameter values

The Mohr-Coulomb criterion has been widely used to describe the strength of walls failing in sliding (Celano et al., 2021; Magenes & Calvi, 1997). Even though some slight modifications to take into account the cracking of the cross section, the aspect ratio of the wall, and the aspect ratio of the bricks have been proposed (Celano et al., 2021), this section will use the pure Mohr

Coulomb criterion (given in Equation (1)) for reasons of simplicity and due to the lack of a large database of small-scale tests. To compute the cohesion, C, and friction coefficient, μ, of the specimens, one would need tests under multiple axial loads. The only specimens that have been tested under different axial loads, are (SW06, SW08) and (SW09-SW11). The average V_u of SW06 and SW08 is 1.09 kN (for an axial load of 1.52kN) while the average V_u of SW09-SW11 is 1.72 kN (for an axial load of 3.02). Assuming that they fail according to a Mohr Coulomb criterion, the cohesion force is C equal to 0.45kN (which implies a cohesion stress of c equal to 0.11 MPa) and the coefficient of friction is μ = 0.42. These values have been previously reported for full scale masonry structures (Celano et al., 2021), even though the cohesion is rather on the low side and found mainly in historic structures or low bond strength masonry, while the coefficient of friction is rather on the higher end. However, walls SW06-SW11 have rather wide notches (11 mm). Walls SW01, SW02, SW04, SW05 have narrower notches and their cohesion is expected to be slightly larger.

The above results show that the values of the Mohr Coulomb parameters that control the sliding strength of the model walls, are not dissimilar to the values encountered in prototype full scale masonry.

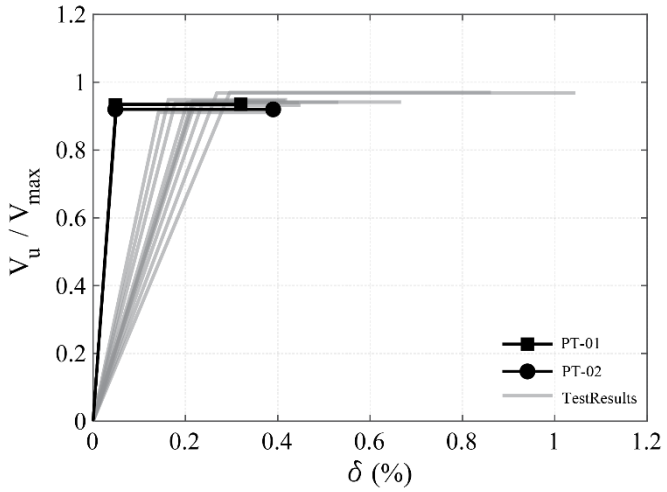

Figure 11. Comparison of the experimental bilinear envelopes and the bilinear curves from the literature (Messali et al., 2020; Salmanpour et al., 2015).

4.7.2 Comparison based on the bilinear curve

This comparison takes the form of a non-dimensional plot, where the x-axis reports the drift ratio and the y-axis the ratio between the ultimate load and the maximum load (V_u/V_{max}). Figure 10 shows the non-dimensional bilinear envelopes of the model walls (in grey), and the results of PT-01 and PT-02. PT-01 has an elastic drift equal to δ_e = 0.05 %, an ultimate drift ratio of

δ_u = 0.32 % and V_u/V_{max} = 0.93. PT-02 has an elastic drift ratio of δ_e = 0.05 %, an ultimate drift ratio equal to δ_u = 0.39 %, and V_u/V_{max} = 0.92.

The non-dimensional lateral load of the tested model walls varies from 0.93 to 0.97 (Table 5), which is in good agreement with the results of the prototype reference walls. However, the model walls have a normalized initial stiffness (defined as the initial stiffness of the bilinear curves of Figure 11) which is, on average, around 4 times lower than the one of the prototype walls. This is clearly a drawback of the physical model that should be taken into account when such a model is to be used. However, this drawback refers to a comparison to the specific prototype walls that were used for comparison.

With the exception of SW01 and SW04, the ultimate drift ratio δu is in the order of 0.4%, which is close to the values reported for the prototype walls

Therefore, the comparison of the non-dimensional bilinear curves unveils that the model walls exhibit a softer pre-yield behavior, but a similar ultimate drift.

4.7.3 Centrifuge testing: comments and considerations

An in depth analysis of the scaling laws for centrifuge tests of small-scale masonry models manufactured with binder jet 3D printers lies beyond the scope of this work. Nonetheless, insights on the interpretation of future centrifuge tests of specimens made using 3D printed masonry material are presented in this section.

Centrifuge tests of the developed masonry model will have the primary objective to preserve similitude of stresses without the need of artificial masses. This has the advantage of preserving the distribution of masses, which is crucial in dynamic testing.

Scaling laws for centrifuge testing are available in the literature for geotechnical problems (Madabhushi 2017), where the model material is typically the prototype material. To the author's knowledge, scaling laws for masonry structures in an artificial gravitational field are not available in the literature. The displacement of a structure subject to a ground motion is

$$u(t) = f\left(l, \sigma(\varepsilon), \rho, \ddot{u}_g(t), t\right) \tag{2}$$

where *u(t)* is the displacement of a point of the structure, *l* is a characteristic dimension of the structure, $\sigma(\varepsilon)$ is the stress-strain relationship of the material, ρ is the specific density of the material, *g* is the gravity constant, $\ddot{u}_g(t)$ is the ground acceleration, and *t* is the time. According

the Buckingham's theorem the above function can be rewritten as a function of independent non-dimensional variables as follows:

$$\frac{u(t)}{l} = \varphi\left(\frac{\sigma(\varepsilon)}{\rho g l}, \frac{\ddot{u}_g\left(t\sqrt{\frac{g}{l}}\right)}{g}, t\sqrt{\frac{g}{l}}\right) \tag{3}$$

Based on the first term in Equation 3, if the model material has the same density with the prototype, the gravitational field (g) needs to be increased inversely proportional to the size (l). However, the 3D printed material has a density of 1300 kg/m^3 which is in between the density of hollow clay blocks (700-1000 kg/m^3) and concrete blocks (1700-1900 kg/m^3). Therefore, the physical model will be slightly distorted. However, since the scope of the centrifuge tests is not to capture the behavior of the prototype structure but rather to validate the global level assumptions, such a distortion due the difference in density could be considered acceptable.

Admittedly, the physical models are softer than the prototypes they were compared to, because the printed material is softer than the prototype. One could try to tackle this by deviating from the standard centrifuge scaling laws. For example, modulate g according to the $E/\rho l$ ratio (where E would be the pre-yield stiffness of the material. But this would distort the post-yield behavior, which seems relatively low distorted under the usual centrifuge laws. Therefore, some sort of distortion will be unavoidable.

Assuming that the scaling laws for geotechnical centrifuge tests will be used to interpret the results of shake table tests of 3D printed masonry structure the post-elastic displacement capacity of the model masonry can be interpreted by following the following scaling law

$$dispalcement_{model} = \frac{1}{N} \cdot displacement_{prototype} \tag{4}$$

where N is the scaling factor of the geometry. Therefore, the displacements of the model need to be multiplied by the scaling factor N to get the prototype ones. For instance, the ultimate displacement for sample SW02 is equal to 1.37 mm (see Table 5), this is equivalent to 13.7 mm at prototype scale. This value is compares well to the ultimate displacements of PT-01 and PT-02 which are 8.32mm and 10.76 mm, respectively.

Before performing small-scale system level shake table test on 3D printed masonry structure it is crucial to assess not only the in-plane behavior but also the out-of-plane behavior, and the connection between 3D printed walls and with the diaphragm floor.

4.8 Conclusions

Small scale masonry physical models for centrifuge testing are useful to study both the system-level (global) assumptions of numerical models and Soil Structure Interaction problems. This paper proposes using a sand-based Binder Jet 3D Printer to create 1:10 scale physical models of masonry. As such printers can only print one material, while masonry comprises two (bricks and mortar), it is proposed to emulate mortar by modulating the micro geometry of the material at the joints by printing notches.

Depending on the geometry of the notches, compressive tests on 1:10 scale walls showed a strength between 9 and 12.4 MPa, while the Young's modulus ranged between 3.6 and 4.2 GPa. Cyclic tests under fixed-fixed conditions and constant vertical load were performed. Subsequently the backbone shear force-deformation curves were bilinearized. Approximating the shear strength with a Mohr Coulomb law, leads to a cohesion of 0.11MPa and a coefficient of friction of 0.42. These values can be encountered in full scale prototype masonry, especially of low bonding strength. The yield drift ratio of the bilinear curves was found to be one fourth of the yield drift of the prototype walls that were used for comparison – and this is a drawback of the physical model. However, the ultimate drift ratio was, in general, found to be in good agreement with the prototype walls.

In the future more tests could be performed, at more scales and under different normalized axial loads. Moreover, out-of-plane behavior should be investigated, especially if the model. It seems feasible to use a sand-based Binder Jet 3D printer to manufacture physical models of masonry walls to perform shake table tests within a geotechnical centrifuge. Multiple specimens can be rapidly built. The data generated can be used to validate the global level assumptions of numerical models used for the seismic analysis of masonry structures. Moreover, such tests can be used to study Soil Structure Interaction problems, both dynamic and static.

References

Abrams, D. (1996). Effects of scale and loading rate with tests of concrete and masonry structures. Earthquake Spectra, 12(1), 13–28.

Bachmann, J. A., Strand, M., Vassiliou, M. F., Broccardo, M., & Stojadinović, B. (2018). Is rocking motion predictable? Earthquake Engineering & Structural Dynamics, 47(2), 535–552.

Benjamin, J. R., & Williams, H. A. (1957). The behavior of one-story reinforced concrete shear walls. Journal of the Structural Division, 83(3), 1–49.

Bradley, B. A. (2013). A critical examination of seismic response uncertainty analysis in

earthquake engineering. Earthquake Engineering and Structural Dynamics, (42), 1717–1729. https://doi.org/DOI: 10.1002/eqe.2331

Celano, T., Argiento, L. U., Ceroni, F., & Casapulla, C. (2021). Literature review of the in-plane behavior of masonry walls: Theoretical vs. experimental results. Materials, 14(11). https://doi.org/10.3390/ma14113063

CEN. (2002). EN 1052–1:2002. Methods of test for masonry—part 1: determination of compressive strength. European Committee for Standardisation. Brussels, Belgium.

Correlated Solutions Digital Image Correlation. (2022). Retrieved November 16, 2022, from https://www.correlatedsolutions.com/

Drysdale, R. G., Hamid, A. A., & Baker, L. R. (1994). Masonry structures: behavior and design.

Del Giudice, L., & Vassiliou, M. F. (2020). Mechanical properties of 3D printed material with binder jet technology and potential applications of additive manufacturing in seismic testing of structures. Additive Manufacturing, 36, 101714. https://doi.org/10.1016/j.addma.2020.101714

Del Giudice, L., Wróbel, R., Katsamakas, A. A., Leinenbach, C., & Vassiliou, M. F. (2022). Physical modelling of reinforced concrete at a 1:40 scale using additively manufactured reinforcement cages. Earthquake Engineering and Structural Dynamics, 51(3), 537–551. https://doi.org/10.1002/eqe.3578

Del Giudice, L., Marelli, S., Sudret, B., & Vassiliou, M. F. (2023). Global sensitivity analysis of 3D printed material with binder jet technology by using surrogate modeling and polynomial chaos expansion. Progress in Additive Manufacturing, 1–15.

Hamid, A. A., Abboud, B., & Harris, H. G. (1986). Direct small scale modeling of grouted concrete block masonry. In US-PRC joint workshop on seismic resistance of masonry structures. Harbin, China.

Hendry, A. W., & Murthy, C. K. (1965). Comparative tests on 1/3 and 1/6 scale model brickwork piers and walls. In Proceedings of the British ceramic society (Vol. 4).

Hendry, A. W., & Sinha, B. P. (1969). Shear tests on full-scale single-storey brickwork structures subjected to precompression. British Ceramic Research Association.

Kovarbašić, M., Salzmann, R., & Mojsilović, N. (2021). Static-cyclic tests on masonry wall with asymmetric opening. In 14TH CANADIAN MASONRY SYMPOSIUM MONTREAL, CANADA.

Madabhushi, G. (2017). *Centrifuge modelling for civil engineers*. CRC press.

Magenes, G., & Calvi, G. M. (1997). In-plane seismic response of brick masonry walls. Earthquake Engineering and Structural Dynamics, 26(11), 1091–1112. https://doi.org/10.1002/(SICI)1096-9845(199711)26:11<1091::AID-EQE693>3.0.CO;2-6

Malomo, D., Mehrotra, A., & DeJong, M. J. (2021). Distinct element modeling of the dynamic response of a rocking podium tested on a shake table. Earthquake Engineering & Structural Dynamics, 50(5), 1469–1475.

Mata-Falcón, J., Haefliger, S., Lee, M., Galkovski, T., & Gehri, N. (2020). Combined application of distributed fibre optical and digital image correlation measurements to structural concrete experiments. Engineering Structures, 225, 111309.

Mendes, N., Costa, A. A., Lourenço, P. B., Bento, R., Beyer, K., de Felice, G., et al. (2017). Methods and approaches for blind test predictions of out-of-plane behavior of masonry walls: A numerical comparative study. International Journal of Architectural Heritage, 11(1), 59–71.

Messali, F., Esposito, R., Ravenshorst, G. J. P., & Rots, J. G. (2020). Experimental investigation of the in-plane cyclic behaviour of calcium silicate brick masonry walls. Bulletin of Earthquake Engineering, 18(8), 3963–3994. https://doi.org/10.1007/s10518-

020-00835-x

Mohammed, A. (2006). Experimental comparison of brickwork behaviour at prototype and model scales. Cardiff University.

Mohammed, A., & Hughes, T. G. (2011). Prototype and model masonry behaviour under different loading conditions. Materials and Structures/Materiaux et Constructions, 44(1), 53–65. https://doi.org/10.1617/s11527-010-9608-6

Montgomery, D. C. (2017). Design and analysis of experiments. John Wiley & Sons.

Parisse, F., Cattari, S., Marques, R., Lourenço, P. B., Magenes, G., Beyer, K., et al. (2021). Benchmarking the seismic assessment of unreinforced masonry buildings from a blind prediction test. In Structures (Vol. 31, pp. 982–1005). Elsevier.

Petry, S., & Beyer, K. (2014). Scaling unreinforced masonry for reduced-scale seismic testing. Bulletin of Earthquake Engineering, 12(6), 2557–2581.

Reggiani Manzo, N., Vassiliou, M. F., Mouzakis, H., & Badogiannis, E. (2022). Shaking table tests of a resilient bridge system with precast reinforced concrete columns equipped with springs. Earthquake Engineering & Structural Dynamics, 51(1), 213–239.

Ritter, S. (2017). Experiments in tunnel-soil-structure interaction. PhD Thesis, University of Cambridge.

Ritter, S., Giardina, G., DeJong, M. J., & Mair, R. J. (2017). Influence of building characteristics on tunnelling-induced ground movements. Géotechnique, 67(10), 926–937.

Ritter, S., Giardina, G., Franza, A., & DeJong, M. J. (2020). Building deformation caused by tunneling: Centrifuge modeling. Journal of Geotechnical and Geoenvironmental Engineering, 146(5), 4020017.

Salmanpour, A. H., Mojsilović, N., & Schwartz, J. (2015). Displacement capacity of contemporary unreinforced masonry walls: An experimental study. Engineering Structures, 89, 1–16. https://doi.org/10.1016/j.engstruct.2015.01.052

SIA 262/1:2013. (2013). SIA 262/1:2013 - Annex G. Concrete Structures - Supplementary specifications.

Sinha, B. P., & Hendry, A. W. (1969). Racking Tests on Storey-Height Shear Wall Structures with Openings Subjected to Precompression. Designing, Engineering and Constructing with Masonry Products, Gulf Publication Co., Houston, Texas, 192–199.

Tomazevic, M. (1999). Earthquake-resistant design of masonry buildings (Vol. 1). World Scientific.

Tomaževič, M. (1987). Dynamic modelling of masonry buildings: storey mechanism model as a simple alternative. Earthquake Engineering & Structural Dynamics, 15(6), 731–749.

Tomaževič, M., Weiss, P., Velechovsky, T., & Modena, C. (1990). Seismic behaviour of masonry buildings—shakingtable study of masonry buildings with different structural configuration—summary report, models 1, 2, 3 and 4. Test Report, Ministry of Research Activity and Technology, Ljubljana, Slovenia.

Vassiliou, M. F., Cengiz, C., Dietz, M., Dihoru, L., Broccardo, M., Mylonakis, G., et al. (2021). Shake table testing of a rocking podium: Results of a blind prediction contest. Earthquake Engineering & Structural Dynamics, 50(4), 1043–1062.

Zhong, C., & Christopoulos, C. (2021). Finite element analysis of the seismic shake-table response of a rocking podium structure. Earthquake Engineering & Structural Dynamics, 50(4), 1223–1230.

Zhong, C., & Christopoulos, C. (2023). Scaled shaking table testing of higher-mode effects on the seismic response of tall and slender structures. Earthquake Engineering & Structural Dynamics, 52(3), 549–570.

5. Physical modelling of reinforced concrete at a 1:40 scale using additive manufactured reinforced cages

This chapter consists of the post-print version of the following published article, differing from the original only in terms of layout and formatting:

Del Giudice, L., Wróbel, R., Katsamakas, A. A., Leinenbach, C., & Vassiliou, M. F. (2022). Physical modelling of reinforced concrete at a 1: 40 scale using additively manufactured reinforcement cages. Earthquake Engineering & Structural Dynamics, 51(3), 537-551.

Available at https://doi.org/10.1002/eqe.3578

Abstract

Global level assumptions of numerical models have received relatively less attention, but have been indicated to be a major source of error in numerical modeling of Reinforced Concrete (RC) structures. In parallel, it has been stated that a statistical approach involving many virgin specimens and ground motions is necessary for model validation. Such an approach would require very small-scale testing. Then, the reinforcement fabrication becomes a major issue. This paper proposes using additive manufacturing to fabricate the reinforcement cage. It presents the results from cyclic tests on 1:40 RC cantilever members. The cages were manufactured using an SLM 3Dprinter able to print rebars with submillimeter diameters. Different longitudinal and transverse reinforcement configurations were tested. A numerical model using existing Opensees elements was built and its parameters were calibrated against material level small-scale tests. It captured the cyclic response of the RC members with a reasonable accuracy. The cyclic behavior of the RC members resembles the behavior of full-scale RC members indicating that such small-scale specimens can be used for the statistical validation of the global level assumptions of numerical models.

5.1 Introduction

Small-scale testing of RC structures was the rule some 40 years ago, when large shake tables did not exist. The interested reader is referred to (Harris & Sabnis, 1999) for a list of references discussing physically modeling concrete at scales on the order of 1/5–1/8. As concrete properties are scale-dependent (Bazant & Kazemi, 1991; Bažant & Li, 1995; Belgin & Şener, 2008; Litle & Paparoni, 1966)(among many others), small scale models (smaller than 1:5) were abandoned when larger shake tables were constructed. Nowadays, there are two reasons to test RC

models at a very small scale, such as 1:40 (or smaller).

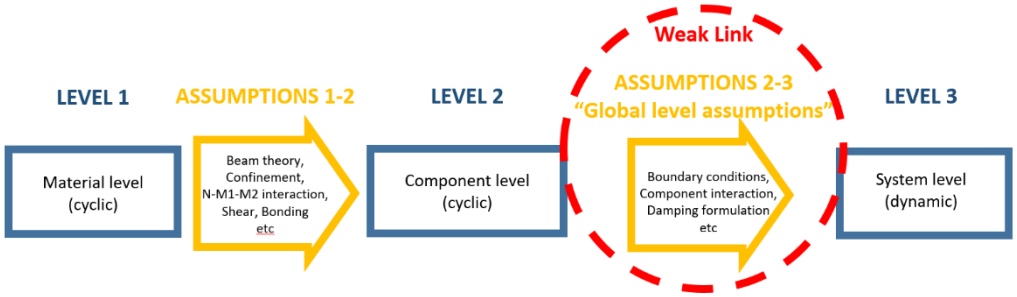

Figure 1. Schematic representation of material to component system-level transition.

The first reason is to use them in centrifuge modeling of soil structure interaction (SSI) problems, where scales between 1:20 and 1:100 are typical (Knappett et al., 2011). In such scales, the structure is only crudely modeled and typically it is attempted to preserve the similitude of stiffness using polymeric materials (Abdoun et al., 2003) or aluminum alloys (Hayward et al., 2000; Knappett & Madabhushi, 2009) while the strength is usually distorted, unless models with notches are used (Deng et al., 2012). Alternatively, small-scale reinforced concrete elements are constructed (Al-Defae et al., 2013; Al-Defae & Knappett, 2014a, 2014b; Loli et al., 2014). To limit the concrete scale effects, (Knappett et al., 2011) used a model concrete comprising properly distributed sand as an aggregate and gypsum as a binding element. They manufactured the reinforcement by hand using steel wire. Manufacturing the reinforcement is the bottleneck both in terms of time to build the specimens and in terms of feasible scales. At a 1:40 scale, a 12-mm stirrup becomes 0.3 mm and this is clearly not manageable by hand.

The second reason is to use very small-scale physical models for the validation of the system-level ("global") assumptions (e.g., global damping formulation, component interaction, boundary conditions) of the numerical models. These have been identified as a major source of error in numerical modeling in an opinion paper by (Bradley, 2013). Indeed, blind prediction contests have shown that numerical models perform much better in predicting the component-level cyclic behavior of RC members ("Collapse Prevention Center," 2011; Trüb, 2011) than the system-level dynamic behavior of RC structures (Schoettler et al., 2012; Terzic et al., 2015) (Figure 1). This highlights the need for system level shake table testing. In parallel, (Bachmann et al., 2018, 2019; Del Giudice & Vassiliou, 2020) have shown that it is not always possible to validate numerical models deterministically (i.e., by trying to predict the response to individual ground motions). In fact, it is not even clear whether shake table tests of RC structures are repeatable. To this end, (Bachmann et al., 2018, 2019; Del Giudice & Vassiliou, 2020) have

proposed that models should be validated statistically under sets of ground motions, with a virgin specimen for each test. Clearly, this is not feasible in full scale, and the authors of this paper (Del Giudice et al., 2020) have suggested that model validation can be performed at a very small scale (say 1:40) and using a centrifuge.

It is acknowledged that a 1:40 model will be unavoidably distorted, as concrete properties scale with size, even when scaled aggregates are used. However, the purpose of this approach is not to create undistorted models but to statistically validate the global level assumptions (Figure 1) for given and experimentally obtained (at the model scale) component level behavior. Therefore, it needs to be clarified that the purpose of small-scale tests is not to determine the component level behavior of full-scale RC members. This can and should be determined by tests as close as possible to full scale. Moreover, the methodology discussed in this paper is easier to apply to modern structures that are designed to be ductile and fail by forming plastic hinges – a failure mechanism that is less influenced by scale phenomena. Physically modeling older structures that could fail in shear or because of the non-ductile design of joints is a larger step to take and is not the focus of this paper.

Notably, a 1:40 scale and the new ETH Zurich geotechnical centrifuge that has a platform of 1 × 1 m (extendable to 1 × 2 m) allows for testing of a typical five-story 15 × 15-m building or a whole overpass bridge together with the soil and the abutments.

Manufacturing of the 1:40 RC elements by hand presents three limitations: the construction time, the accuracy in positioning the reinforcement, and the size limitation of the steel rebars and stirrups. More specifically, manufacturing by hand the 1:50 bridge pier that was tested in (Loli et al., 2014) takes 4 h of watchmaker's precision work – and this is easier than manufacturing physical models of building columns that are even smaller. Clearly, it is not time-effective to build the reinforcement of a whole small-scale (e.g., 1:40) building by hand, while multiple specimens are impossible. Moreover, results from previous work (Loli et al., 2014) show that hand accuracy might be good enough for SSI work, but it is not acceptable for studies focusing on the structure itself. Finally, it is not possible to manufacture the joints by hand, where column and beam rebars intersect with the stirrups. These limitations can be overcome by using a metal 3D printer to manufacture the reinforcement (Del Giudice et al., 2020). The use of a metal 3D printer allows manufacturing of the entire reinforcement cage (longitudinal and horizontal reinforcement) with the desired layout.

This paper serves as a proof of concept and presents some first experimental results. It presents, for the first time, cyclic tests on 1:40 specimens with 3D printed reinforcement. It aims at characterizing the flexural behavior of 1:40 scale RC members by means of full-reversed quasi-static cyclic tests on cantilever specimens of different reinforcement ratios. A simple setup is used that only applies lateral load. The experimental results are compared to numerical simulations performed in Opensees (Mazzoni et al., 2006) using modeling techniques commonly used with full-scale RC elements. The difficulties in 3D printing such small specimens and in performing cyclic tests at such scale are highlighted. This work should not be confused with the attempts to use additive manufacturing technologies to construct full-scale buildings, either by 3D printing the concrete (Asprone et al., 2018; Buswell et al., 2018; Khoshnevis, 2004) or the reinforcement (Hack et al., 2017; Mechtcherine et al., 2018). Both the means and the goals are completely different. The only similarity sources from the umbrella term "3D printing" that is used to describe very different technologies.

5.2 Materials and methods

5.2.1 Specimen description

The experimental program reported in the following sections consists of five cyclic cantilever tests of small-scale reinforced concrete members subjected to fully reversed cycles. The specimens are 55-mm height with a square cross section of 15 × 15 mm (Figure 2). Assuming a length scale of 1:40, in the prototype scale, the specimen has dimensions 600 × 600 × 2200 mm. Assuming an inflection point in the mid-height of the member, the test is intended to study a 600 × 600 × 4400-mm member. The base of the specimens consists of a square footing of 65 mm by 65 mm, 20-mm thick (Figure 2).

Two longitudinal reinforcement ratios are considered, that is, ρ_l = 2.2% and ρ_l = 1.1%. The former will be referred to as high (H). The latter one will be referred to as low (L), not because the reinforcement is absolutely low, but because it is lower than the 2.2% specimens. The H specimens have 16 bars of 0.6-mm diameter (24 mm in prototype scale) whereas the L specimens have 8 bars of 0.6-mm diameter. In both cases, the reinforcement is doubly symmetric with a concrete cover c of 1.64 mm.

Label	Longitudinal Reinforcement	Shear Reinforcement
HH	Heavily (H)	High (H)
HL	Heavily (H)	Low (L)
LH	Lightly (L)	High (H)
LL	Lightly (L)	Low (L)
LN	Lightly (L)	No Stirrups (N)

Table 1. Specimens list and details

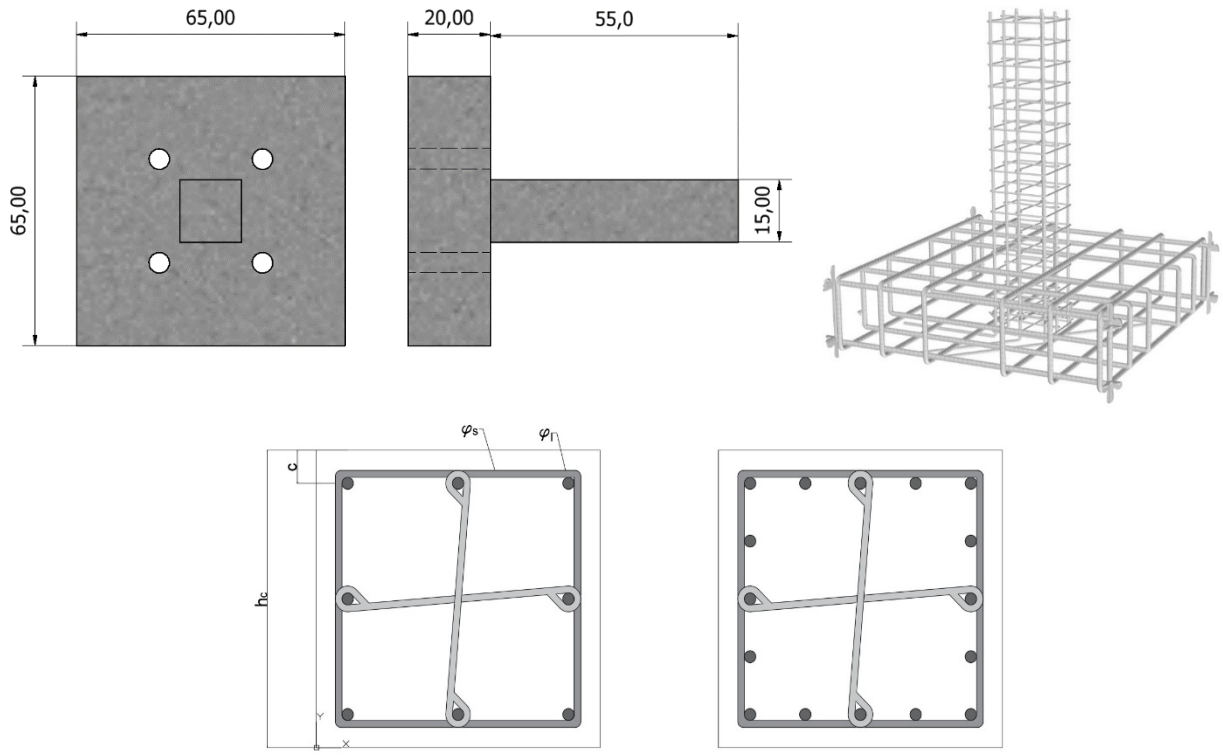

Figure 2. Top: Specimen dimensions and reinforcement. Bottom: Reinforcement layout for the specimens having lighter (left) and heavier (right) longitudinal reinforcement.

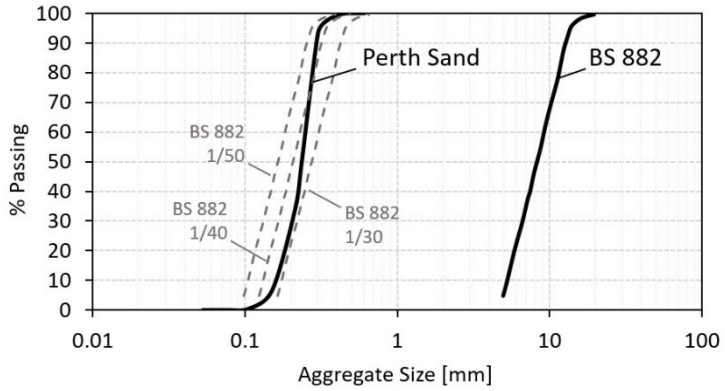

Figure 3. Passing distribution of the sand used in the micro-concrete.

Regarding the transverse reinforcement, three layouts with different spacing were tested: 2.5 mm of spacing (ρ_w =0.76%, labeled H), 5 mm of spacing (ρ_w = 0.38%, labeled L), and no transversal reinforcement (labeled with an N for no- reinforcement). Shear ties are included in the specimens with transverse reinforcement. The diameter of the transversal reinforcement bars and the shear ties is 0.35 mm (14 mm in prototype scale). Not all combinations of the above properties were tested. Table 1 summarizes the labeling and characteristics of each specimen.

5.2.2 Micro-concrete

Due to the small scale of the specimens, it is necessary to scale the inert component of the concrete so that the ratio inert size/rebars/cross section is about the same as in the prototype scale. Perth silica sand with a d50 = 0.23 mm was used. Its grain distribution compares well to the typical aggregate size when scaled 40 times (Figure 3).

The cement-based micro-concrete mixture consists of cement Normo52.5R, Perth sand, and water. The ratio binding component/sand/water was 1/1/0.5. The mix design was chosen to minimize the water percentage while preserving a good workability and flowability of mixture.

The mechanical properties of the micro-concrete were investigated through three uniaxial compression tests on cylindrical specimens of 20-mm diameter and 50-mm height, and three 4-point bending tests performed on prism specimens with cross section 15 × 15 mm and length of 80 mm. The size of the compression and 4-point bending test specimens was close to the size of the cantilever specimens, so that the values obtained from the material-level tests are directly applicable to modeling of the component-level tests. However, the specimens were larger than what would be dictated by a 1:40 scaling of the standardized specimens used for material testing of concrete (i.e., 300 × 150 mm cylinders and prisms of 40 × 40 × 160 mm). The specimen tested in compression is roughly a 1:5 model of the standardized prototype cylinder and the one tested in 4-point bending is a 1:10 model of the standardized prototype prism, and this is one of the reasons for the high tensile to compressive strength obtained by the tests.

Figure 4 plots the stress–strain curves of the compression tests. The resulting average (coefficient of variation – CoV) compressive strength f_c is equal to 34.9 MPa (3.4%), the strain at the maximum load ε_1 is 3.7‰ (3.4%), and the modulus of rupture f_{ct} is 4 MPa (5%).

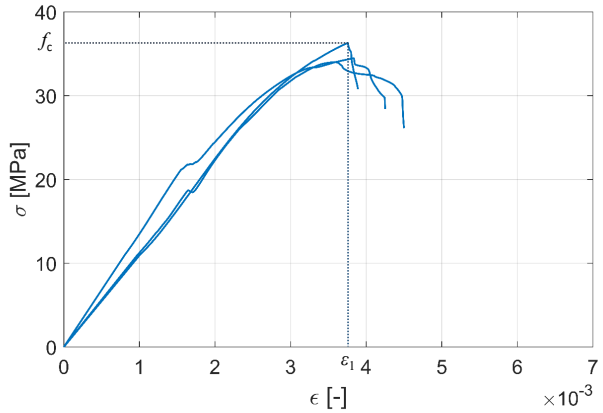

Figure 4. Micro-concrete's stress-strain curves.

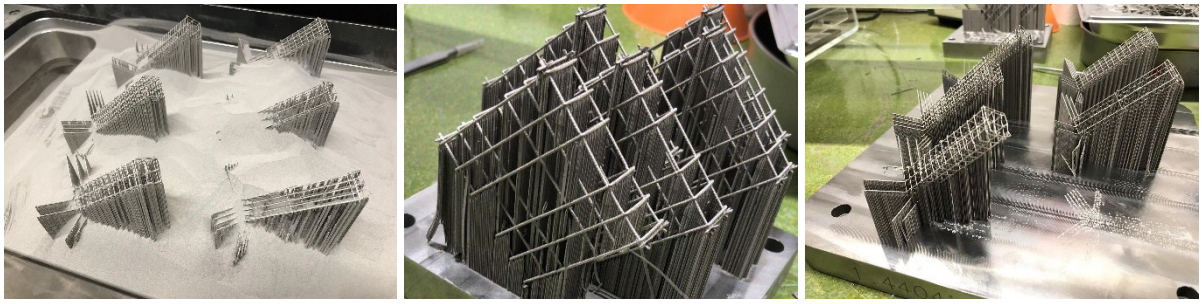

Figure 5. Printed reinforcement with a necessary support structure. Left: 3D printer Jobbox. Center: Reinforcement cage after the printing process. Right: Footing reinforcement after the printing process.

The Young's modulus E_c is calculated as the secant stiffness at 0.4 f_c and it is equal to 13.4 GPa (1.11%). As only three tests were performed, the confidence interval on the CoV is relatively large and the values reported are only indicative.

5.2.3 3D printed reinforcement

The use of a 3D printer allows manufacturing of the entire reinforcement cage, namely the longitudinal and shear reinforcement, with the designed layout (Figure 5). Depending on the 3D printer, one can print rebars as small as 0.20 mm (200 μm), which in the prototype scale (1:40) represent Φ8 rebars. Even though significant advances were made in the recent years, additive manufacturing of metals is not a plug-and-play procedure yet and requires a careful preparation of the build job considering the geometry and size of the parts to achieve the best quality in a reasonable build time. In addition, overhanging features require support structures (Figure 5) to avoid part distortion and to prevent the part from local overheating. Support structures are printed in the same build job and need to be manually removed afterwards. The careful reader will observe that (a) the stirrups are completely closed (i.e., there is no 135° hook, as in the prototype elements), (b) the hooks of the shear ties are also closed, (c) there is a continuity between longitudinal reinforcement and stirrups, that is, they go through each other. This is a limitation sourcing from the capabilities of the metal 3D printer that was used, which, as all-metal 3D printers, cannot easily print overhanging features. The stirrups and shear ties being closed are not expected to distort the model, as modern buildings require hooks that are not supposed to open, and indeed they do not (Tanaka, 1990). The influence of the continuity between longitudinal and transverse reinforcement is quantifiable and can be taken into account when manufacturing physical models of specific target properties to be used in a centrifuge for system-level testing or for SSI problems, where the research question is not the behavior of the element, but of the whole system for a given component-level behavior.

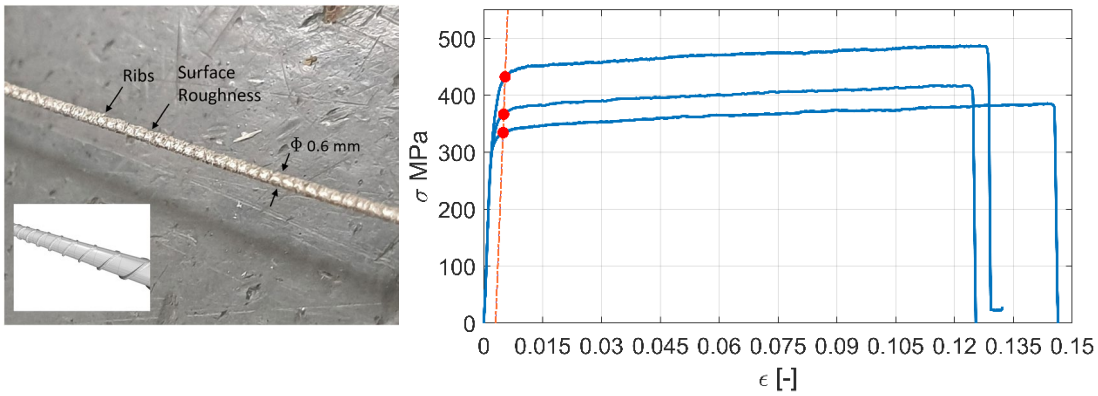

Figure 6. 3D printed steel's stress-strain curves.

This study used a Concept Laser M2 Laser Powder Bed Fusion (LPBF) printer that is able to manufacture various types of metal. A gas-atomized stainless steel 316L powder with a grain size 15–45 μm was used. All rebars were printed with ribs on the surface to increase bonding with concrete (Figure 6, left). The rib parameters for the 0.6-mm rebars (according to (EN, 2005)) were h = 0.05 mm, b = 45°, and c = 0.6 mm, while for the transverse, they were h = 0.029 mm, b = 45°, and c = 0.35 mm. In addition, the 3D printed steel has a roughness Ra value of 15–20 μm, hence it has an inherent roughness that increases steel-concrete bonding.

The mechanical properties of the 3D printed steel were characterized with a series of uniaxial tension tests performed on 0.6-mm diameter bars identical to the ones used as reinforcement in the micro RC samples. Due to the small cross section, a sensor arm extensometer was used instead of strain gauges. The gauge length was 30mm to measure the strains during the tests. The resulting average yield strength f_y was 377 MPa (CoV = 13.2%). This value was calculated using the offset of 3‰ as suggested by (ASTM, 2016). The average maximum strength $f_{s,max}$ was 417 MPa (12.1%) and the average Young's modulus E_s was equal to 176.7 GPa (1.6%). These values are in line with those reported by (Casati et al., 2016) for 3D printed Stainless steel 316L. The experimental uniaxial behavior of the 3D printed steel is reported in Figure 6 (right): The stiffness of the printed material at such a small scale, that is, 0.6 mm of diameter, is consistent across multiple specimens. Nonetheless, the yield and ultimate stresses have a non-negligible variability. Given that larger 3D printed coupons that were tested showed less variability, the dispersion of Figure 6 (right) can be attributed to geometric imperfections at such a small scale. Therefore, in the future, either larger scales should be attempted, or finer steel powders (i.e., the raw material that the 3D printer uses) or more precise 3D printers should be used.

5.2.4 Experimental setup and instrumentation

The cyclic tests were performed in a universal testing machine (UTM), equipped with a support to attach the specimens and loading attachment. A fully reversed cyclic loading was applied at the top of the samples. The elements were placed horizontally and fixed on a steel support designed to fit in the UTM and to align the samples to the center of the machine (Figure 7). The base of the specimens was fixed to the lateral support with four M6 bolts. A 2 × 65 × 65-mm steel plate was placed between the bolts and the face of the base to avoid local crushing of the concrete due to the compressive force applied by the screws.

The load is applied at the centerline of the element by two loading pins, which are connected to a double-hinged fork (Figure 7). The latter transfers the vertical load applied by the UTM. The measuring devices consist of two LVTD and a 3D-DIC system. The first LVDT measures the vertical displacement at the application point of the load, while the second LVDT measures the vertical displacement of the base of the element (to measure any possible sliding of the base). Digital image correlation (DIC) was used to measure the displacements and the strain field at the lateral surface of the RC member. The strain distribution was used to identify any cracks and micro-cracks formed during the tests and to locate the plastic hinges that formed at the base of the element.

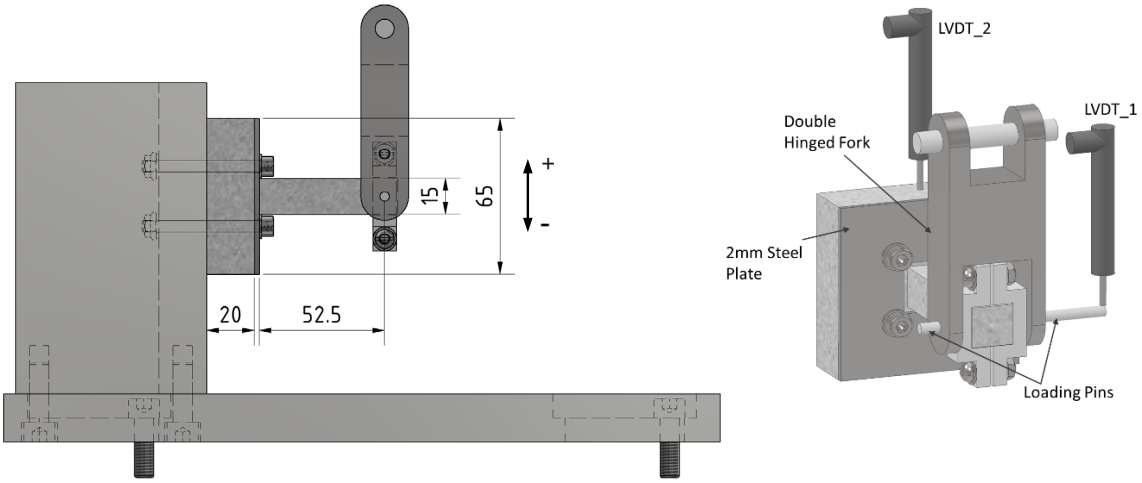

Figure 7. Experimental setup and details of the loading apparatus.

5.2.5 Loading protocol

The load is applied by displacement control, applying a displacement Δ at the top of the elements. The kinematic parameter that is used to define the loading protocol is the drift ratio φ,

which is defined as the ratio between the top displacement and the element length l_v = 52.5 mm (in this case it also represents the shear span).

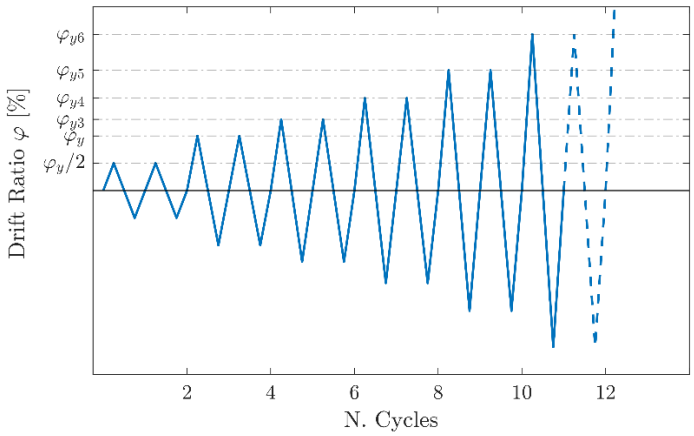

Figure 8. Loading protocol in terms of drift ratio φ

The test program is defined based on (FEMA 461, 2007) in which the amplitude increase is defined as $\varphi_{n+1} = 1.4 * \varphi_n$. However, to capture the behavior of the element in the elastic range, the first amplitude was set equal to $0.5 \times \varphi_y$ and the second one was set to the yield drift, φ_y (see Figure 8). The yield drift was calculated for each specimen using a fiber model in Opensees (Mazzoni et al., 2006) and is defined as the drift that causes the first yield of reinforcement.

The velocity of application of the load was selected considering two principles. First, the displacement rate needs to be as low as possible to minimize any inertia and strain rate effects. Second, the loading rate needs to be reasonably fast to avoid creep and to make the test feasible time-wise. On these premises, the strain rate needed to be within a range of $\dot{\varepsilon} = 10^{-5}$-$10^{-4}$ s^{-1}. This strain refers to the outermost fiber of the cross section of the RC member that lies closer to the foundation. The lower end of the strain-rate range corresponds to a displacement rate of the actuator equal to 0.075 mm/min, which was used for the first three amplitudes of the loading protocol. For the subsequent four amplitudes, the displacement rate was set to 0.413 mm/min, which corresponds to a strain rate of 5.6×10^{-5} s^{-1}. According to (Mander et al., 1988) such a strain rate corresponds to an increase of concrete strength and stiffness of less than 3% and 1.5%, respectively, which is considered negligible. Finally, the last cycles were applied with a displacement rate of 0.75 mm/min, corresponding to the upper limit of the aforementioned strain rate range.

5.3 Results

5.3.1 Load-deformation response: observations and discussion of the results

No shear failure occurred and all five specimens failed in bending. Concrete spalling (i.e., crushing of the unconfined concrete) occurred only in the HH and HL specimens. The spalling was not visible by naked eye and a magnifying lens was needed. However, no concrete spalling occurred in specimens LH, LL, and LH. This is in contrast with the behavior of full-scale columns, but it can be explained by the lack of axial loading: the specimen loading conditions resemble more a beam than a column. In all cases, failure involved fracture of the longitudinal reinforcement. In all but the LL case, this occurred at the base cross section where a clearly visible crack was formed. In the LL case, failure was caused by a crack at a distance of 3.9 mm from the base. Micro-cracks were not visible by the eye because of the small scale of the specimens. However, DIC analysis (Figures 9 and 10, right: horizontal strain distribution at peak load, measured with 3D-DIC system) showed that micro-cracks along the length of the specimens did form, with the exception of the LL specimen. Based on the above, the behavior of the

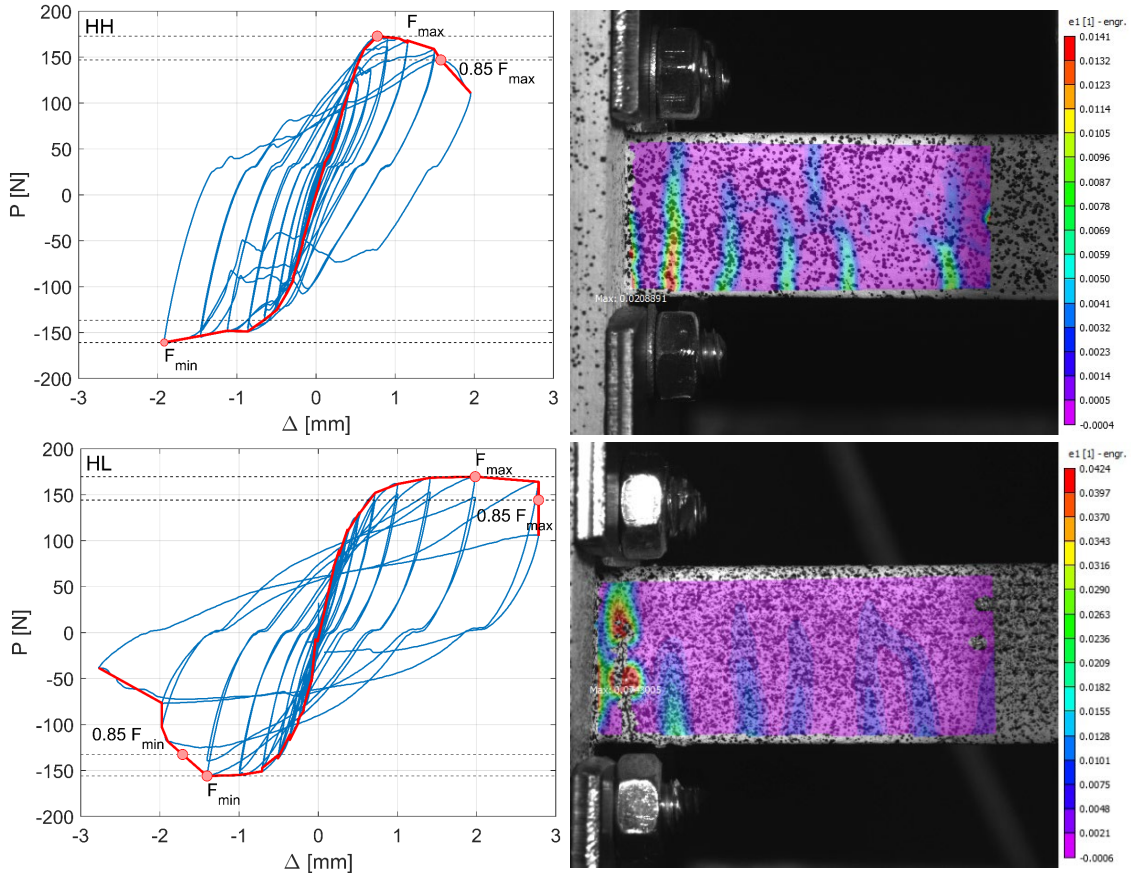

Figure 9. Specimens HH and HL. Left: Force-deformation loops. Right: Horizontal strain at peak load, measured with DIC.

RC members is controlled by the behavior of the steel reinforcement. Figures 9 and 10 (left) also offer the lateral force-displacement loops (P-Δ) for all tested specimens and the backbone curves for each specimen. The backbone is defined as the curve connecting the point of maximum displacement of the first cycle of each loading amplitude. The failure load ($F_{0.85}$) is con-

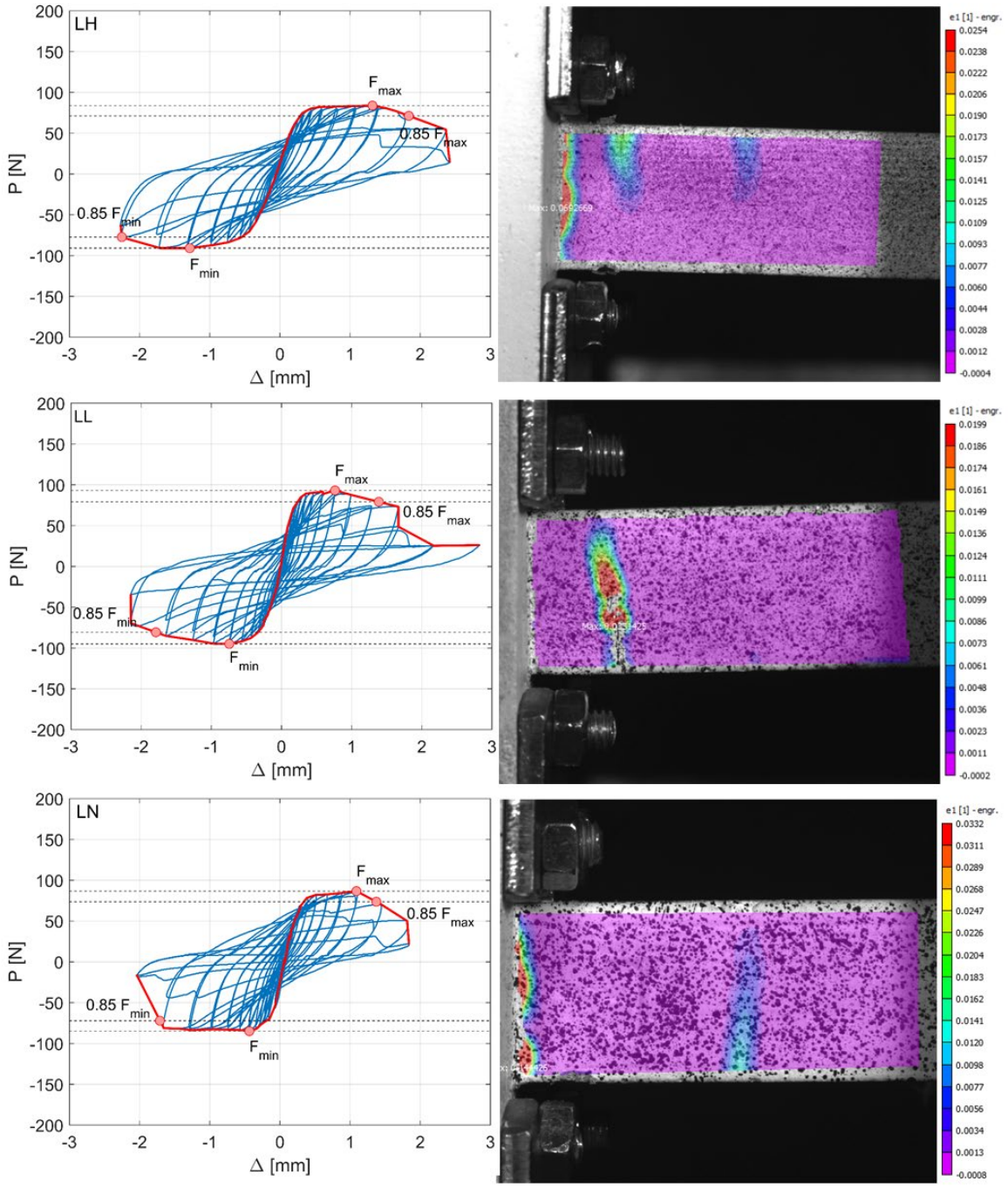

Figure 10. Specimens LH, LL, and LN. Left: Force–deformation loops. Right: Horizontal strain at peak load, measured with DIC.

ventionally defined as a strength degradation to 85% of the peak load (F_{max}) (i.e., of the strength). The results are summarized in Table 2. The relevant drift ratios are defined as φ_{max} and $\varphi_{0.85}$. Based on Figures 9 and 10, the following observations can be made:

(a) In all tests, there is a measured sliding on the order of 0.2 mm (=0.35%) in load reversal. This is a drawback of the custom-made clevis of the setup. In future tests, the displacement of the end cross section of the specimen itself should be directly measured. This setup drawback makes the relative error of the displacement at small drift ratios large. Therefore, this discussion will not focus on yield displacement but only on displacement and drift ratio at maximum load (φ_{max}) and ultimate displacement ($\varphi_{0.85}$).

(b) In the HH specimen, there is a clear offset of this sliding by roughly 30N indicating that for this test, there was a misalignment of the setup. This is reflected in not reaching maximum load towards negative displacements. So, the results for HH will not be furtherly discussed.

(c) A comparison of the HL specimen to the LH, LL, and LN specimens clearly shows that an increase in the longitudinal reinforcement causes an increase in strength. This behavior is expected and is compatible with the behavior of prototype RC members. A quantitative discussion on the issue is offered in the next section.

(d) A comparison of the HL and LL specimen reveals that an increase in longitudinal reinforcement causes an increase in both φ_{max} and in $\varphi_{0.85}$. This is not compatible with the behavior in the prototype scale, as according to (Panagiotakos & Fardis, 2001), the displacement at ultimate load $\varphi_{0.85}$ should not depend on the longitudinal reinforcement. However, given the variability in RC members response, especially when it comes to deformation (Biskinis, 2007), a comparison between only two specimens is not adequate for general conclusions and more specimens should be tested.

(e) A comparison of the LH, LL, and LN shows that the strength is not significantly influenced by the transverse reinforcement. This is compatible with the visual observation that these specimens failed because of the fracture of the longitudinal rebars and no concrete spalling was observed. Therefore, for the specimens tested, any possible increase of concrete strength because of confinement offered in LH and LL should not influence the strength of the RC member.

Specimen		F_{max} [N]	φ_{max} [%]	$F_{0.85}$	$\varphi_{0.85}$ [%]
HH	+	172.80	1.474	146.88	3.002
	-	-	-	-	-
HL	+	169.60	3.775	144.16	5.299
	-	156.60	2.660	132.60	3.263
LH	+	83.7	2.512	83.70	3.499
	-	90.90	2.286	77.26	4.291
LL	+	93.66	1.445	79.10	2.641
	-	94.93	1.415	80.69	3.408
LN	+	86.70	2.076	73.69	2.610
	-	84.90	0.830	72.16	3.258

Table 2. Summary of the results from the cyclic tests.

(f) From the above observations, it seems that specimens LH, LL, and LN should have behaved the same and the differences in their behavior can only be attributed to what can be called "natural variation," that is variations caused by setup imperfections, or the geometric and mechanical properties of the materials. (Biskinis, 2007), based on 1844 tests published in literature, reports that such variations in prototype scale RC columns lie in between 0% and 38% for the yield moment and 0% and 59% for the yield drift. The CoV of F_{max}, φ_{max}, and $\varphi_{0.85}$ of the tests reported in this paper and assuming the positive and negative values as independent measurements are 5%, 37%, and 20%. Therefore, it can be concluded that for the small-scale specimens LH, LL, and LN, the "natural variation" observed is not something uncommon in full-scale tests too. This is in line with the observations of (Knappett et al., 2018).

(g) Even though the specimens were symmetrically reinforced, their force–deformation loops are not perfectly symmetric. This is a behavior that is not incompatible with full-scale tests. For example, (Saatcioglu & Ozcebe, 1989) report an asymmetric behavior for the specimen they tested under zero axial load. In the small-scale model, the asymmetric behavior can be explained by the variability of the steel properties, but also from the Bauschinger effect and the isotropic hardening of the steel under cyclic loading.

5.4 Numerical results

The purpose of this section is to show that numerical models developed for full-scale RC elements can describe the behavior of the tested small-scale models, if their parameters are calibrated against the small-scale material tests. Then according to the rationale developed in the introduction, these models could be used to validate the global level assumptions (Figure 1) against small-scale shake table tests that can be performed in a centrifuge.

To this end, numerical models of the cyclic tests were implemented in Opensees, and the results were compared against the experimental curves. The cantilever beam was modeled in 2D with three nonlinear forceBeamColumn elements and using a fiber model to characterize the hysteretic behavior of the rebars, unconfined concrete, and confined concrete (Figure 11). Each element included three integration sections.

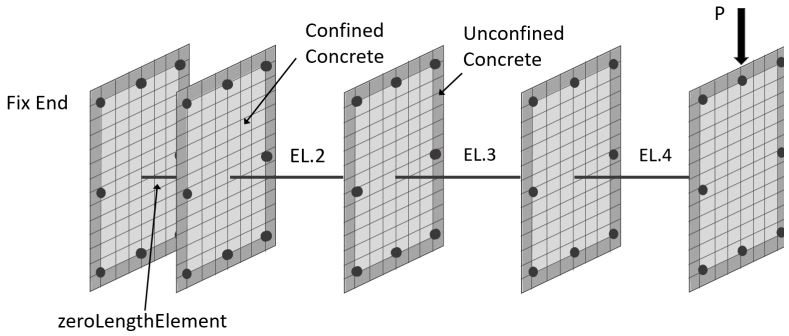

Figure 11. Schematic of the OpenSees model using fiber model and nonlinear force-BeamColumn elements.

The reinforcement was modeled using the Opensees Steel02 model (which is the Giuffré–Menegotto-Pinto model with isotropic hardening (Filippou et al., 1983)) enhanced with a MinMax model with strain at failure ε_{lim}. All but one of the parameters used were either calibrated on the uniaxial tension tests described in section 3.3 or the default Opensees values were chosen (Table 3). The sole parameter that was calibrated ad hoc on the cyclic tests of the RC member was a3, which is a parameter that controls the isotropic hardening of steel.

The concrete was modeled using Concrete01 (which is the Kent–Scott–Park concrete model (Scott et al., 1982)). The parameters for the unconfined concrete (cover) were obtained from the material level tests on the small-scale specimens, while the f_{cc}, ε_{cc}, and f_{ccu} of the confined concrete (core) were calculated using Mander's model that provides the confined concrete stress-strain curve for given unconfined concrete properties and transverse reinforcement (Mander et al., 1988). As Mander's model does not provide the ultimate stress ε_{ccu}, this was computed using the formula suggested by (Fib, 2012). All parameters are summarized in Table 4 and defined in Figure 12.

Parameter	Value	Parameter	Value
f_y	377.8 [*MPa*]	a1	0
E_s	180 [*GPa*]	a2	1
b_s	0.003	a3	0.02
R0	15	a4	1
cR1	0.925 (default)	ε_{lim}	0.135
cR2	0.15 (default)		

Table 3. Steel02 parameters

	Unconfined Concrete		**Confined Concrete**			
Specimen	f_c [*MPa*]	ε_1	f_{cc} [*MPa*]	ε_{cc}	f_{ccu} [*MPa*]	ε_{cc}
HH	34.5	0.0038	43.11	0.008	38.40	0.059
HL	34.5	0.0038	38.26	0.005	23.64	0.048
LH	34.5	0.0038	43.11	0.008	38.40	0.059
LL	34.5	0.0038	38.26	0.005	23.64	0.048
LN	34.5	0.0038	-	-	-	-

Table 4. Concrete01 parameters of cover and core concrete.

An additional zero-length section element was used at the fixed end of the cantilever beam in order to model strain penetration. The strain penetration causes slippage of the anchored bars, which leads to a fix-end rotation of the beam-column element. The fix-end rotation can be captured modeling the steel fiber in the zero-length section with the Bond_SP01 model developed by (Zhao & Sritharan, 2007) which accounts for the bar slippage. The model used by the Bond_SP01 element is defined by six parameters; yield stress of the rebars F_y, ultimate stress of the rebars F_u, a parameter R that governs the pinching of the cyclic force-slip loops, the hardening ratio b of the force-slip loops, and s_y and s_u which represent the rebar slip at yielding and the rebar slip at failure, respectively. (Zhao & Sritharan, 2007) defined s_y as

$$s_y(mm) = 2.54\left(\frac{d_b(mm)}{8437}\frac{f_y(MPa)}{\sqrt{f_c}}(2\alpha+1)\right)^{1/\alpha} + 0.34 \quad (1)$$

which was derived from a set of pullout tests at full-scale, and consequently it is not suitable for small-scale models. Preforming small-scale pullout tests to determine s_y lies beyond the scope of this paper. Therefore, s_y was calibrated so that the experimental curves of the cyclic tests discussed in the previous section match the Opensees numerical results. The value for s_u is conventionally defined as $40s_y$. The Bond_SP01 model parameters are reported in Table 5.

Parameter	Value
f_y	377.8
b	0.5
R	1
s_y	0.03
s_u	1.2

Table 5. Bond_SP01 parameters.

Figure 13 compares the experimental and numerical results of all the samples. With the exception of the last cycles, the numerical model is able to capture the cyclic loops with a reasonable accuracy. Notably, as these are cyclic tests, the displacement protocol is used as an input to the numerical model that essentially predicts the corresponding forces. A drawback of the model is that the longitudinal reinforcement in the numerical model did not fracture and this explains the poor performance of the model in the last cycles. Interestingly, the maximum

strain of the reinforcement in the numerical model was smaller than 0.096, while the fracture strain was numerically set to 0.135. As the reinforcement strain within the plastic hinge strongly depends on the strain penetration, evidently the calibration of the strain penetration parameters of the numerical model was not optimal. Such a calibration would require pullout tests that are not trivial at a 1:40 scale and lie beyond the scope of this paper.

The good match between the experimental results of cement-based micro RC models and the Opensees models, calibrated with standard material models, which are generally used in full-scale applications, suggest that small-scale physical models manufactured with 3D printed reinforcement can be used to perform system-level testing of whole structures with the purpose of obtaining datasets that can be used for the statistical validation of system-level assumptions. However, more research is needed in order to accurately physically model strain penetration.

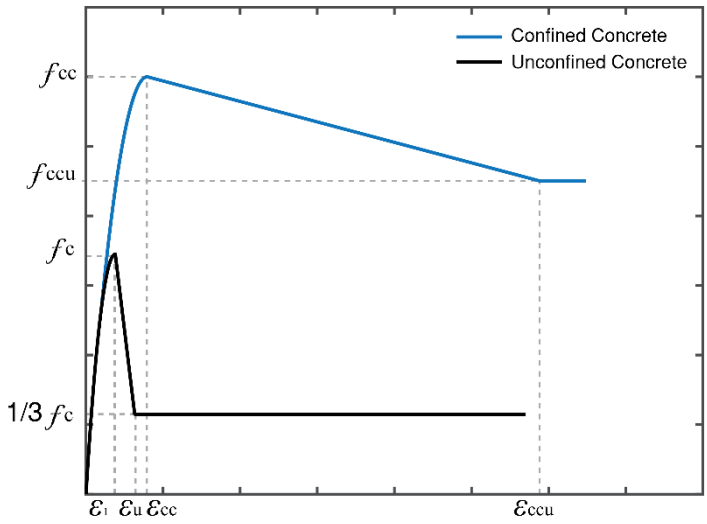

Figure 12. Definition of the parameters of the stress-strain diagram of the concrete column.

5.5 Conclusions

A large part of uncertainty and error in numerical modeling lies in the global level assumptions of numerical models. This has not attracted the attention it deserves, because it is not easy to produce much system-level (i.e., structure-level) data.

This paper proposes testing small-scale structures (e.g., whole buildings) on a shake table placed in a centrifuge. Sand can be used as an aggregate for small-scale concrete and submillimeter diameter reinforcing steel can be printed and placed by a metal 3D printer. Model

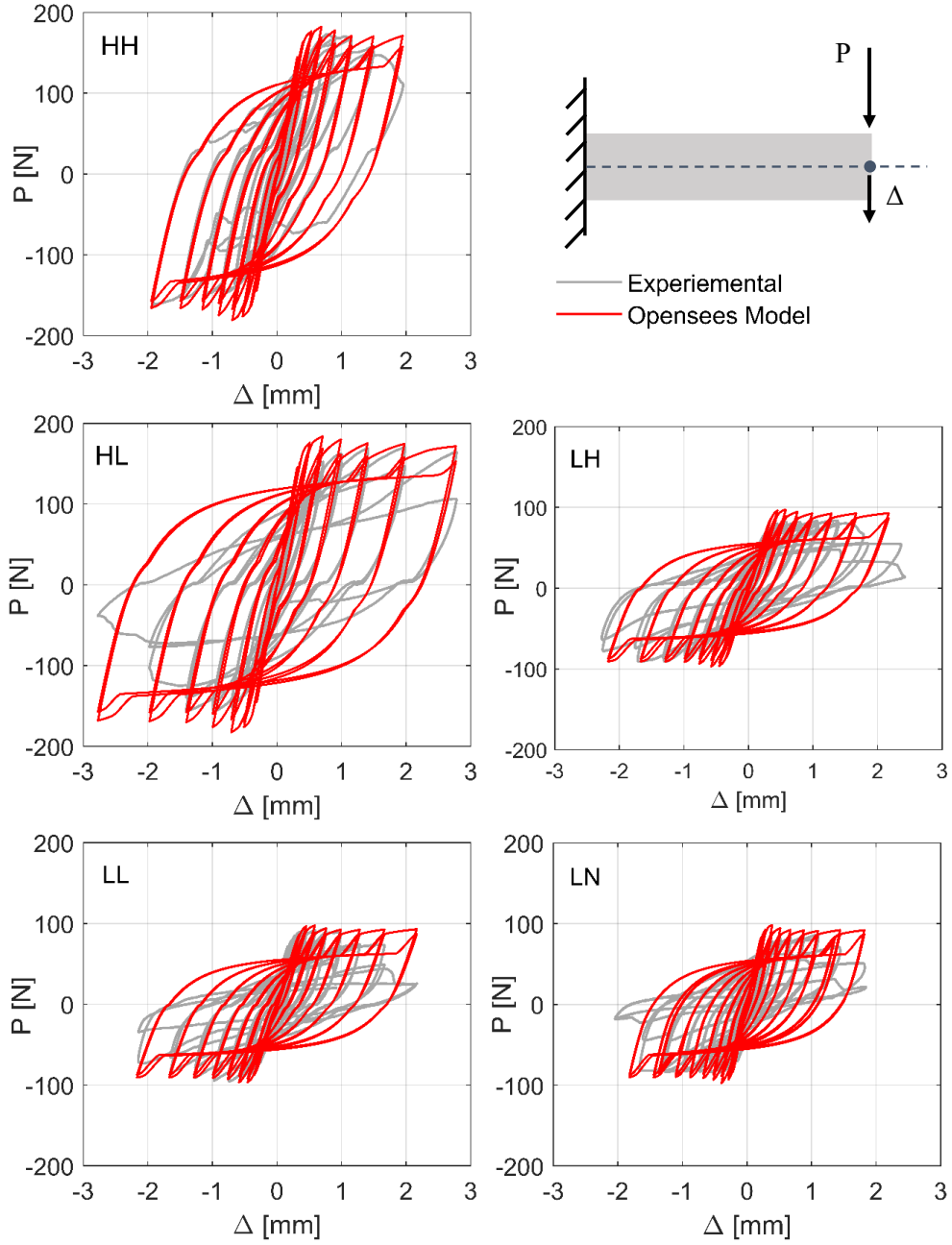

Figure 13. Comparison between experimental results and Opensees model.

("small scale") concrete showed similar compressive and flexural strength with prototype concrete. The 0.6-mm diameter 3D printed rebars had a Young Modulus of 177 GPa and a yield stress on the order of 380MPa, making it similar (albeit slightly weaker) to steel used for reinforcement. However, the dispersion of its strength is larger at such small diameters, something that is not observed in larger coupons.

RC members having cross section as small as 15 × 15 mm and reinforcement of 0.6 mm (longitudinal) and 0.35 mm (transverse) were manufactured and tested cyclically. They

were designed to fail in bending by failure of their reinforcement. The RC members were tested cyclically and their behavior was similar to the behavior of full-scale specimens, in terms of their hysteresis loops. For these specific cases, their variability was similar to the variability observed in full-scale tests.

An Opensees model, using elements and materials developed for full-scale structures, was built. The model used fiber elements and took account of strain penetration. It was able to capture the experimental behavior with a reasonable accuracy.

In the future, more tests are needed. At the material level, the steel behavior needs to be better quantified via cyclic tests. The steel–concrete bond behavior needs to be tested and made similar to the prototype behavior by fine tuning the roughness and ribs of the printed rebars. At a component level, tests with more longitudinal reinforcement and denser stirrups should be tested to study the behavior of confined cross sections where the concrete properties govern their flexural response.

It seems feasible to produce small-scale models of a full structure to perform dynamic tests in a geotechnical centrifuge. The shake table tests could provide datasets to statistically validate the global level assumptions that are usually made to scale up from component- to system-level behavior. Moreover, physical modeling or RC at such small scale could provide experimental data for problems on which few physical tests have been performed, like pounding of buildings or bridge–abutment interaction.

Acknowledgments

This paper has benefited from discussions with Mr. Medhat Elmorsy. Open access funding provided by Eidgenössische Technische Hochschule Zürich.

References

Abdoun, T., Dobry, R., O'Rourke, T. D., & Goh, S. H. (2003). Pile response to lateral spreads: centrifuge modeling. *Journal of Geotechnical and Geoenvironmental Engineering*, *129*(10), 869–878.

Al-Defae, A. H., & Knappett, J. A. (2014a). Centrifuge modeling of the seismic performance of pile-reinforced slopes. *Journal of Geotechnical and Geoenvironmental Engineering*, *140*(6), 4014014.

Al-Defae, A. H., & Knappett, J. A. (2014b). Stiffness matching of model reinforced concrete for centrifuge modelling of soil-structure interaction. In *8th International Conference on Physical Modelling in Geotechnics, ICPMG 2014* (pp. 1067–1072). CRC Press.

Al-Defae, A. H., Caucis, K., & Knappett, J. A. (2013). Aftershocks and the whole-life seismic performance of granular slopes. *Géotechnique*, *63*(14), 1230–1244.

Asprone, D., Auricchio, F., Menna, C., & Mercuri, V. (2018). 3D printing of reinforced

concrete elements: Technology and design approach. *Construction and Building Materials*, *165*, 218–231.

ASTM. (2016). *E8/E8M-16a: Standard Test Methods for Tension Testing of Metallic Materials*. ASTM international.

Bachmann, J., Strand, M., Vassiliou, M. F., Broccardo, M., & Stojadinovic, B. (2018). Is rocking motion predictable? *Earthquake Engineering & Structural Dynamics*, *47*(2), 535–552.

Bachmann, J., Strand, M., Vassiliou, M. F., Broccardo, M., & Stojadinovic, B. (2019). Modelling of rocking structures: Are our models good enough? In *2nd International Conference on Natural Hazards & Infrastructure (ICONHIC 2019)*.

Bazant, Z. P., & Kazemi, M. T. (1991). Size effect on diagonal shear failure of beams without stirrups. *ACI Structural Journal*, *88*(3), 268–276.

Bažant, Z. P., & Li, Z. (1995). Modulus of rupture: size effect due to fracture initiation in boundary layer. *Journal of Structural Engineering*, *121*(4), 739–746.

Belgin, Ç. M., & Şener, S. (2008). Size effect on failure of overreinforced concrete beams. *Engineering Fracture Mechanics*, *75*(8), 2308–2319.

Biskinis, D. (2007). *Strength and deformation capacity of reinforced concrete members with or without strengthening*. University of Patras.

Bradley, B. A. (2013). A critical examination of seismic response uncertainty analysis in earthquake engineering. *Earthquake Engineering and Structural Dynamics*, (42), 1717–1729. https://doi.org/DOI: 10.1002/eqe.2331

Buswell, R. A., De Silva, W. R. L., Jones, S. Z., & Dirrenberger, J. (2018). 3D printing using concrete extrusion: A roadmap for research. *Cement and Concrete Research*, *112*, 37–49.

Casati, R., Lemke, J., & Vedani, M. (2016). Microstructure and fracture behavior of 316L austenitic stainless steel produced by selective laser melting. *Journal of Materials Science & Technology*, *32*(8), 738–744.

Collapse Prevention Center. (2011). Retrieved September 29, 2019, from http://www.collapse-prevention.net/download/Competition/RC_Frame/RC_Frame_ Competition.htm

Deng, L., Kutter, B. L., & Kunnath, S. K. (2012). Centrifuge modeling of bridge systems designed for rocking foundations. *Journal of Geotechnical and Geoenvironmental Engineering*, *138*(3), 335–344.

EN, B. S. (2005). 10080–Steel for the reinforcement of concrete–Weldable reinforcing steel–General. *Brussels: Central Secretariat*.

FEMA 461. (2007). *Interim Testing Protocols for Determining the Seismic Performance Characteristics of Structural and Nonstructural Components*. Federal Emergency Management Agency.

Fib. (2012). *Model Code 2010 - Final Draft* (Vol. 2). Berlin: Ernst & Sohn, Wiley.

Filippou, F. C., Popov, E. P., & Bertero, V. V. (1983). Effects of bond deterioration on hysteretic behavior of reinforced concrete joints.

Del Giudice, L., & Vassiliou, M. F. (2020). Mechanical properties of 3D printed material with binder jet technology and potential applications of additive manufacturing in seismic testing of structures. *Additive Manufacturing*, *36*, 101714. https://doi.org/10.1016/j.addma.2020.101714

Del Giudice, L., Wrobel, R., Leinenbach, C., & Vassiliou, M. F. (2020). Static Testing of Additively Manufactured Microreinforced Concrete Specimens for Statistical Structural Model Validation at a Small Scale. In *8th International Conference on Advances in Experimental Structural Engineering (8AESE)*.

Hack, N., Wangler, T., Mata-Falcón, J., Dörfler, K., Kumar, N., Walzer, A. N., et al. (2017). Mesh mould: an on site, robotically fabricated, functional formwork. In *Second concrete innovation conference (2nd CIC), paper*.

Harris, H. G., & Sabnis, G. (1999). *Structural modeling and experimental techniques*. CRC press.

Hayward, T., Lees, A. S., Powrie, W., Richards, D. J., & Smethurst, J. (2000). Centrifuge modelling of a cutting slope stabilised by discrete piles.

Khoshnevis, B. (2004). Automated construction by contour crafting—related robotics and information technologies. *Automation in Construction*, *13*(1), 5–19.

Knappett, J. A., & Madabhushi, S. P. G. (2009). Influence of axial load on lateral pile response in liquefiable soils. Part I: physical modelling. *Geotechnique*, *59*(7), 571–581.

Knappett, J. A., Reid, C., Kinmond, S., & O'Reilly, K. (2011). Small-scale modeling of reinforced concrete structural elements for use in a geotechnical centrifuge. *Journal of Structural Engineering*, *137*(11), 1263–1271.

Knappett, J. A., Brown, M. J., Shields, L., Al-Defae, A. H., & Loli, M. (2018). Variability of small scale model reinforced concrete and implications for geotechnical centrifuge testing. In *Physical Modelling in Geotechnics* (pp. 241–246). CRC Press.

Litle, W. A., & Paparoni, M. (1966). Size effect in small-scale models of reinforced concrete beams. In *Journal Proceedings* (Vol. 63, pp. 1191–1204).

Loli, M., Knappett, J. A., Brown, M. J., Anastasopoulos, I., & Gazetas, G. (2014). Centrifuge modeling of rocking-isolated inelastic RC bridge piers. *Earthquake Engineering & Structural Dynamics*, *43*(15), 2341–2359.

Mander, J. B., Priestley, M. J. N., & Park, R. (1988). Theoretical stress-strain model for confined concrete. *Journal of Structural Engineering*, *114*(8), 1804–1826.

Mazzoni, S., McKenna, F., Scott, M. H., & Fenves, G. L. (2006). OpenSees command language manual. *Pacific Earthquake Engineering Research (PEER) Center*, *264*, 137–158.

Mechtcherine, V., Grafe, J., Nerella, V. N., Spaniol, E., Hertel, M., & Füssel, U. (2018). 3D-printed steel reinforcement for digital concrete construction–Manufacture, mechanical properties and bond behaviour. *Construction and Building Materials*, *179*, 125–137.

Panagiotakos, T. B., & Fardis, M. N. (2001). Deformations of reinforced concrete members at yielding and ultimate. *Structural Journal*, *98*(2), 135–148.

Saatcioglu, M., & Ozcebe, G. (1989). Response of reinforced concrete columns to simulated seismic loading. *Structural Journal*, *86*(1), 3–12.

Schoettler, M., Restrepo, J., Guerrini, G., & Duck, D. E. (2012). A full-scale, single-column bridge bent tested by shake-table excitation.

Scott, B. D., Park, R., & Priestley, M. J. N. (1982). Stress-strain behavior of concrete confined by overlapping hoops at low and high strain rates. In *Journal Proceedings* (Vol. 79, pp. 13–27).

Tanaka, H. (1990). Effect of lateral confining reinforcement on the ductile behaviour of reinforced concrete columns.

Terzic, V., Schoettler, M. J., Restrepo, J. I., & Mahin, S. A. (2015). Concrete column blind prediction contest 2010: outcomes and observations. *PEER Report*, *1*, 1–145.

Trüb, M. (2011). Numerical modeling of high performance fiber reinforced cementitious composites. *IBK Bericht*, *333*.

Zhao, J., & Sritharan, S. (2007). Modeling of strain penetration effects in fiber-based analysis of reinforced concrete structures. *ACI Materials Journal*, *104*(2), 133.

6. Conclusions and Future Research

Abstract

This chapter summarizes the key findings and contributions of this dissertation. It also presents the conclusions drawn at the end of each chapter. The main limitations of the study of this dissertation are presented and suggestions for the future research are offered.

6.1 Synopsis and key conclusions

This dissertation consists of six chapters summarizing the work conducted on the development of small-scale masonry and RC models manufactured with 3D printing. The developed physical models can be used for the statistical validation of the global-level assumptions of numerical models. Given the importance of numerical simulations for structural engineering, the lack of a large database of experimental results from system-level dynamic testing is of utmost importance to validate their performance. However, the excessive cost associated with these tests is a barrier for the creation of such a database. This dissertation focused on the development of cost-effective physical models that would enable researchers to perform several shake table tests of masonry and RC structures. The conclusions of each chapter are presented below.

Mechanical properties of 3D printed material with binder jet technology and potential applications of additive manufacturing in seismic testing of structures

Chapter 2 studied the mechanical properties of bulk material that a binder jet 3D printer builds. This material can be used to manufacture small-scale masonry structures. The study consisted of three distinct experimental campaigns aimed at assessing three material features: a) the influence of curing on its compressive and flexural strength; b) any possible scale effects; and c) its orthotropy. The orthotropic behavior of the material in quantified statistically with one-way analysis of variance (ANOVA). The main conclusions are:

- The compressive strength of the 3D printed material, without thermal post-processing, is in the order of 5-6 MPa (depending on the loading orientation).
- The flexural strength of non thermally post-processed 3D printed material is 1.5 MPa.
- ANOVA was performed on the compressive strength of the 3D printed material according to the loading direction. The analysis of variance produced a p-value of 1.54E-06, which indicates that there is very strong evidence that the compressive strength depends on the loading direction.
- The analysis of variance performed for the flexural strength of the material yielded a p-value of 0.078. This indicates a medium to weak evidence against the hypothesis that the direction does not affect the flexural strength. Hence, the material is slightly anisotropic in terms of flexural strength. Given that a p-value of 0.078 is not a clear-cut result, a Tukey-Kramer multiple comparison tests (at 5% level of significance) was

performed on the flexural strength values of the different loading directions. The statistical test confirmed that there is no evidence that the flexural strength is dependent on the loading orientation.

- The dependence of the compressive strength on the specimen size was investigated with a set of uniaxial compression tests of 50mm and 75mm cubic specimens. The results of the tests were analyzed with an ANOVA, assuming size as treatment of the experimental design. One ANOVA per each loading orientation was performed. The p-values were 0.98, 0.66, and 0.72 for loading along X, Y, and Z, respectively. The p-values indicate that there is no significant size effect on the compressive strength of the 3D printed material, for the sizes considered in the study.
- Compressive and flexural strength of the material strongly depends on curing time. The strength build-up is faster in the first two days of curing and it slows down in the subsequent days. The secant rate of strength growth during the first two days was 1.8MPa/days and 0.58MPa/day in compression and bending, respectively. After this rapid increase, the secant rate of strength increase (from day 2 to day 15 of curing) was 0.10 MPa/day and 0.035 MPa/day in compression and bending, respectively.

Global sensitivity analysis of 3D printed material with binder jet technology by using surrogate modeling and polynomial chaos expansion

Chapter 3 furtherly studies the mechanical properties of 3D printed material. It focuses on the relationship between printer parameters and mechanical properties because it is reasonable to assume that there is a correlation between the settings of the printer and the mechanical performances of the material. After a preliminary investigation of the printer settings, four printer parameters are identified that influence the mechanical properties of the material: printing speed, droplet mass, activator percentage, and voxel's resolution. To assess the effect of these four parameters on the compressive strength, Young's modulus, and flexural strength, an experimental design in the form of a latin-hypercube-sampling (LHS) was performed. The test results were used to calibrate a surrogate model developed using a sparse polynomial-chaos-expansion (PCE). Finally, the first order and total Sobol' indices were computed as by-product of the PCE. The main conclusions are:

- Thermal post-processing of the 3D printed material is investigated with a set of tests performed on samples treated at different temperatures and durations. The samples were cured at temperatures of 80°C and 115°C, for 30, 60, and 120 minutes. For these

curing temperatures and durations, the compressive strength of samples treated showed small variability with respect to the curing duration (for given temperature).

- The relationship between the pulse voltage of the piezo ceramic nozzle of the printer and the droplet mass is linear.
- A preliminary assessment of the correlation between input parameters (printer's settings) and output (mechanical properties) using Pearson's correlation coefficients was performed. The correlation coefficients showed that there is a possible linear correlation between the voxel resolution and the mechanical properties of the material. Pearson's correlation coefficient between voxel resolution and the outputs range from -0.80 to -0.91. With respect to the other printing parameters, the correlation was much looser, as the correlation coefficients were all below 0.5.
- By using sparse polynomial chaos expansion, with a limited number of tests it was possible to derive analytical equations to predict the mechanical properties of the material, given the printer parameters.
- Sobol' indices are used to quantify the influence of each input parameter on the mechanical properties of the printed material. As it would have been too expensive to compute the Sobol' indices with traditional Monte Carlo based estimation, the indices were directly obtained as by-product of the PCE.
- First order and total Sobol' indices showed that the voxel resolution is by far the most influential parameter for the mechanical properties of the printed material. Because one droplet of binder is sprayed in each voxel, decreasing the voxel's volume will increase the binder weight per printed bulk material volume ratio (w/v). This ratio is a physical meaningful parameter that controls the mechanical properties of the material. A second input parameter that affects the binder weight to volume ratio is the droplet mass. However, the influence of the droplet mass was not captured by the Sobol' indices because of the small range investigated in the experimental campaign.
- Sobol' indices showed that the printing speed did not significantly affect the mechanical properties of the printed material. A low but not negligible dependence on the activator percentage was found.

Small-scale physical models of unreinforced masonry walls 3D printed with sand-based binder jet technology

Chapter 4 presents the experimental results of a series of quasi-static tests conducted on 1/10-scale masonry walls manufactured with sand-based binder-jet 3D printer. It studies a novel approach to manufacture small-scale masonry walls with one material. The mortar joints of prototype masonry were emulated by controlling the micro-geometry in the joints of the model walls by printing micro-notches. The experimental campaign included uniaxial compression tests of the bulk 3D printed material, the uniaxial compression test of model wallets, and quasi-static cyclic tests of model masonry walls with fixed-end boundary conditions. Different notch geometries were tested and two level of vertical pre-compression were applied to the samples. The main conclusions are:

- The small-scale masonry manufactured with binder jet 3D printed material and micro notches had a compressive strength and Young's modulus of 10.4 MPa and 4038 MPa, respectively. These values are comparable to prototype masonry.
- Model masonry walls failed in sliding.
- The cyclic response of the tested masonry walls showed an initial linear branch with a peak shear force, followed by strength degradation. The strength reached a plateau and the cyclic loops were almost purely frictional. This loop is comparable to prototype walls with similar failure modes.
- Different level of pre-compression had a distinct effect on the maximum shear strength of the specimens.
- The notch geometry had a significant effect on the strength and displacement capacity of the specimens. Increasing the size of the horizontal notches resulted in a decrease in the shear strength.
- The non-dimensional results were compared to prototype walls from the literature. The non-dimensional shear strength compares well to the prototype. The model wall proved less stiff than the prototype walls and with a larger displacement capacity.

Physical modelling of reinforced concrete at a 1:40 scale using additively manufactured reinforcement cages

Chapter 5 describes the development of 1/40-scale physical models of RC beams. Five flexural elements were manufactured with their reinforcement cage completely 3D printed with selective-laser-melting technology. First the mechanical properties of the 3D printer rebars and micro-concrete were tested. Then quasi-static cyclic tests on five small-scale reinforced concrete

elements were performed. The experimental results were finally compared to an Opensees model. The main conclusions are:

- No shear failure occurred during the cyclic tests. All five specimens failed in bending.
- Concrete spalling occurred only in the specimens of high longitudinal reinforcement. The spalling was not visible by naked eye, a magnifying lens was necessary.
- In all specimens, failure involved the fracture of the longitudinal reinforcement at the base of the reinforced concrete elements.
- Comparison between the samples showed that an increase in the longitudinal reinforcement caused an increase in strength.
- Comparison between the samples showed that their strength was not significantly influenced by the transverse reinforcement. This is compatible with the observed failure, i.e. fracture of the longitudinal rebars. Therefore, any increase of concrete strength produced by the confinement should not have influenced the strength of the RC members.
- Numerical results were obtained with an OpenSees model calibrated using standard material models used in full scale reinforce concrete. The material models were calibrated based on the material tests of 3D printed steel and micro-concrete. The numerical results were in good agreement with the experimental results. This suggests that small-scale physical models manufactured with 3D printed reinforcement can be used to perform system-level testing with the purpose of obtaining datasets for the statistical validation of the system-level assumptions.

6.2 Limitations and Future Research

The main limitations of the work summarized in this dissertation, and suggestions for future research are:

- The scale effect investigated in Chapter 2 was assessed with only two different sizes. In future work, a wider range of sizes should be studied.
- The polynomial-chaos-expansion model developed in Chapter 3 was trained on 18 experimental data points. In future studies, the performance of the PCE can be improved by enriching the experimental design with additional data points in order to reduce the leave-one-out errors.
- The effects of the droplet mass on the mechanical properties of the printed material should be further investigated. In future studies, a wider range of variation for the droplet mass should be considered.

- The experimental setup used in Chapter 4 could be improved with some minor adjustments. The stopper used to fix the model walls started to slide after some cycles. The sliding did not affect the results since the measurement were taken directly from the specimen, however it did affect the applied displacement.
- The pre-compression used in the tests presented in Chapter 4 was either 7.21% or 3.60%. Higher level of pre-compression should be used to assess the response of the model masonry.
- Shake table testing of 3D printed masonry model will require in depth study of the similitude laws, to reduce any distortion of the physical model. Such distortions would prevent direct comparison to prototypes. Nonetheless, even a distorted model would be useful, as the main purpose of the suggested testing methodology is the validation of global level assumptions.
- The experimental setup developed for the study of the cyclic behavior of RC beams, presented a series of drawbacks. In all tests, there was a measured sliding on the order of 0.2 mm in load reversal. This sliding is a drawback of the custom-made clevis and the tolerances at the joints. In future studies, the displacement of the end cross section of the specimens should be directly measured. Due to the measured sliding, the error at small drift ratios is large compared to the applied displacement. Moreover, the setup was not able to apply axial load. More complicated setups need to be built to study the behavior of physical models of RC columns (i.e. elements under both axial and lateral loads)
- The study of the mechanical properties of the 3D printed rebars was limited to their uniaxial tensile behavior. In future work, a thorough investigation of mechanical properties should be carried out with special focus on the cyclic behavior of the 3D printed rebars. Furthermore, the bonding between rebars and micro concrete should be assessed through small-scale pullout tests. These tests would allow for a better calibration of the material models used in the OpenSees simulation.
- Future research on small scale RC structures should include testing of beam column joints, as well as full RC frames with floor slabs. To this end, the production of the 3d printed reinforcement needs to be optimized to minimize manual assembly. Ideally, the reinforcement of the entire frame should be 3D printed, if the printing volume is sufficient. Otherwise, the reinforcement can be divided in segments that need to be assem-

bled using reinforcement splices. In this case, it is necessary to directly print the complex reinforcement sections of the frame, such as column-beam joints, and to use splices in areas where the bending moment is minimum – as is done in full-scale reinforced concrete structures.